2024

A SPATIOTEMPORAL ANALYSIS OF OCEAN ACIDIFICATION IN THE PACIFIC-ARCTIC REGION

Thomas V. Caero
University of Rhode Island, vinson.caero@gmail.com

Recommended Citation
Caero, Thomas V., "A SPATIOTEMPORAL ANALYSIS OF OCEAN ACIDIFICATION IN THE PACIFIC-ARCTIC REGION" (2024). *Open Access Master's Theses.* Paper 2476.
https://digitalcommons.uri.edu/theses/2476

A SPATIOTEMPORAL ANALYSIS OF OCEAN ACIDIFICATION IN THE PACIFIC-ARCTIC REGION

BY

THOMAS V. CAERO

A THESIS SUBMITTED IN PARTIAL FULFILLMENT OF THE
REQUIREMENTS FOR THE DEGREE OF
MASTER OF SCIENCE
IN
OCEANOGRAPHY

UNIVERSITY OF RHODE ISLAND
2024

MASTER OF SCIENCE THESIS

OF

THOMAS V. CAERO

APPROVED:

Thesis Committee:

Major Professor	Hongjie Wang
	Brice Loose
	Coleen Suckling
	Brenton DeBeof DEAN OF THE GRADUATE SCHOOL

UNIVERSITY OF RHODE ISLAND

2024

ABSTRACT

The Pacific-Arctic Region (PAR) is highly vulnerable to ocean acidification (OA) due to its low buffer capacity, carbonate concentration, and the regionally-amplified effects of climate change. Although it experiences the highest rates of OA globally, the existing literature lacks observation-based surface decadal OA rates for the PAR, primarily due to large data gaps. To address these limitations, we aggregated open-source carbonate datasets and established spatially-dependent relationships to predict surface total alkalinity (TA) using salinity and temperature (R^2=0.93, MAE = 23 μmol kg^{-1}). We then applied these relationships to gridded sea surface salinity and temperature products to obtain monthly surface TA fields. The TA fields were coupled with the MPI-SOM-FFN surface pCO_2 dataset (doi: 10.7289/v5z899n6) to obtain monthly 1°x 1° surface pH, Ω_{Ar}, and dissolved inorganic carbon fields from 1993-2021 for the entire PAR, yielding the first gapless gridded Arctic carbonate system dataset to date. This dataset indicated that the Southern PAR acidified at rates comparable to the global average, predominantly due to the absorption of anthropogenic CO_2. In contrast, the Bering Sea shelf exhibited basification, likely a result of increased primary productivity. The Northern PAR exhibited acidification rates 2-4x greater than the global rate due to reduced TA linked to sea ice melt. Our findings suggest that continued warming will likely exacerbate surface acidification in regions experiencing a shift from year-round multi-year ice cover to a seasonal ice pack. While local processes such as primary productivity can temporarily counteract OA, whether they can compensate for rising anthropogenic CO_2 levels is unclear. This highlights the complexity of predicting future ocean acidification trends and underscores the importance of advanced models that integrate both climatic and biological factors, enabling accurate forecasts of impacts on marine ecosystems in these highly sensitive regions.

ACKNOWLEDGMENTS

Thank you to my major professor, Hongjie Wang, for their dedication to my graduate education at the University of Rhode Island Graduate School of Oceanography. We would like to acknowledge the vessel crews and scientists in collecting, processing, and publishing all open-source data utilized in this study. We also thank Annika Jersild for providing unpublished variables from the MPI-SOM-FFN dataset which further aided our analysis and Danling Ma for their expertise in driver decomposition.

TABLE OF CONTENTS

MANUSCRIPT

APPENDIX

LIST OF FIGURES

LIST OF TABLES

1. INTRODUCTORY PAGE

The following manuscript is prepared for submission to the American Geophysical Union (AGU) Global Biogeochemical Cycles journal. Co-authors are Thomas Caero and Hongjie Wang. This work will be submitted for publication in May 2024.

2. INTRODUCTION

The industrial revolution spawned an era in which global atmospheric carbon dioxide (CO_2) levels have increased at a rate unparalleled in the last 65 million years (Hönisch et al., 2012; Zeebe et al., 2016). This surge in CO_2 has been a major driver of global climate change (Portner et al., 2019; Lee et al., 2023) and has significantly altered ocean carbonate chemistry by increasing proton concentration [H^+] and decreasing carbonate concentration [${CO_3}^{2-}$], reducing pH and calcium carbonate saturation states (Ω) (*i.e.*, ocean acidification) (Caldeira and Wickett, 2003; Orr et al., 2005; Doney et al., 2009; Portner et al., 2019; Lee et al., 2023). When CO_2 dissolves in seawater, it reacts with H_2O to form carbonic acid (H_2CO_3), which can dissociate into bicarbonate (HCO_3^-) and carbonate (CO_3^{2-}), releasing protons which lower pH. This shift in pH affects the relative proportion of the carbonate species – as water acidifies, free protons react with CO_3^{2-} to form HCO_3^-, decreasing [CO_3^{2-}]. The ocean carbonate system consists of H^+, OH^-, weak acid-base systems, and the four carbonate system parameters and is resolvable to a known degree of uncertainty if temperature, salinity, pressure, and two of the four carbonate parameters are known (Dickson, 2010). The four carbonate system parameters are:

1. Dissolved inorganic carbon (DIC): the total concentration of carbonate species (carbonic acid, bicarbonate, carbonate)
2. Total alkalinity (TA): the ability for seawater to resist changes in acidity due to the concentration of excess proton acceptors relative to proton donors
3. pH: a logarithmic measure of basicness/acidity defined as $-\log_{10}([H^+])$
4. pCO_2: the partial pressure of CO_2

A consequence of decreased [$CO_3{}^{2-}$] is the reduction in aragonite saturation state (Ω_{Ar}), which measures the thermodynamic tendency of aragonite (a form of calcium carbonate prevalent in seawater and marine organisms) to dissolve. Net dissolution of aragonite is thermodynamically favored when $\Omega_{Ar} < 1$. This adversely affects marine calcifiers by influencing their physiological functions (Feely et al., 2004; Orr et al., 2005; Doney et al., 2009), making it difficult to form and maintain their aragonite exoskeletons, and potentially disrupting overall ecosystem dynamics (Cooley et al., 2009; AMAP, 2013; AMAP, 2018; Portner et al., 2019; Lee et al., 2023).

The global ocean has absorbed nearly a third of anthropogenic CO_2 since the mid-18th century, resulting in an average 30% increase in global surface ocean acidity (*i.e.*, [H^+]) (Sabine et al., 2004; AMAP, 2013; Portner et al., 2019). The current understanding is that the global mean surface acidification rates range from 16 to 18 μatm pCO_2, -0.027 to -0.016 pH units, and -0.081 to -0.065 Ω_{Ar} units per decade since the 1980s (Doney et al., 2009; Lauvset et al., 2015; Portner et al., 2019; Iida et al., 2021; Ma et al., 2023). While this broad range is due in part to methodological differences and limited observational data, it primarily reflects the high spatial variability caused by diverse environmental factors impacting the carbonate system. In addition to anthropogenic CO_2 uptake, changes in temperature, salinity, or any of the carbonate system parameters can modify the acidification rate or drive basification (the decrease in [H^+] and increase in Ω_{Ar}). Where carbon uptake exclusively drives acidification, these effects may be less straightforward. For example, warming tends to decrease pH but increase Ω_{Ar} by driving the bicarbonate-to-carbonate dissociation reaction (increasing [CO_3^{2-}] and [H^+]) and lowering CO_2 solubility, which reduces CO_2 via outgassing (increasing [CO_3^{2-}] and decreasing [H^+]) (Jiang et al., 2019; Xue et al., 2020).

Certain regions, such as coastal and high-latitude waters, exhibit acidification rates that significantly diverge from the global mean due to natural and anthropogenic processes not present in typical open-ocean environments. In addition to spatial variations in temperature, salinity, and carbonate system parameters, the influence of sea ice, watershed and riverine discharge, nutrient influx, and dense biological communities also drive variability in the marine carbonate system (Duarte et al., 2013; Carstensen and Duarte, 2019). Climate change has the potential to affect these processes and drive ocean acidification, particularly in the Pacific-Arctic Region (PAR).

The PAR, as defined in this study, encompasses the west Arctic Ocean, its marginal seas (East Siberian, Chukchi, Beaufort), the western Canadian Archipelago, the Bering Sea, the Gulf of Alaska, and the subarctic Pacific Ocean (Figure 1). The PAR is highly vulnerable to ocean acidification due to its inherently low buffer capacity and $[\mathrm{CO}_3^{2-}]$. This primes the PAR to absorb CO_2 as atmospheric concentrations rise, threatening to lower its already near-undersaturated Ω_{Ar} levels. The PAR's natural vulnerability, coupled with regional climate change impacts (Portner et al., 2019; Lee et al., 2023), have manifested in the highest observed rates of ocean acidification globally, with current trends suggesting it will be the first major body of water to reach complete surface undersaturation (Fabry et al., 2009; AMAP, 2013; AMAP, 2018). At the same time, the region is gaining economic and geopolitical significance due to enhanced vessel accessibility resulting from reduced sea ice (Dodman et al., 2022). Consequently, it is emerging as an economic hub in part due to its highly productive fisheries (Dodman et al., 2022). However, acidification may threaten to curb the region's fishery potential given its detrimental effects on marine calcifiers and their vital role in the food chain, underscoring the importance of quantifying regional acidification trends.

While numerous studies have documented surface pCO_2 dynamics (Bates, 2006; Chen and Gao, 2007; Cai et al., 2010; DeGrandpre et al., 2020; Ouyang et al., 2020a; Woosley and Millero, 2020; Ouyang et al., 2021; Tu et al., 2021) and Ω_{Ar} undersaturation events (Chierici and Fransson, 2009; Yamamoto-Kawai et al., 2009; Mathis et al., 2012; Robbins et al., 2013; Semiletov et al., 2016; Wynn et al., 2016) in the PAR, research quantifying long-term (*i.e.*, decadal) surface rates of change in pCO_2, pH, and Ω_{Ar} remain scarce. Table 1 lists the studies that have quantified surface acidification rates and reveals a broad spectrum of results: 7.4 to 61.8 μatm pCO_2, -0.086 to -0.013 pH units, and -0.50 to -0.04 Ω_{Ar} units per decade. This wide range in trend values underscores both the significant spatial variability in PAR surface acidification rates as well as overall uncertainty in the literature. Despite this variability, the consensus among these studies is that surface acidification rates in the PAR, particularly in areas with sea ice, far exceed the global average.

Table 1 highlights two other important factors. For one, observational studies that quantify decadal acidification rates are notably limited. This scarcity primarily stems from the limited availability of direct carbonate system measurements in the PAR prior to the 1990s, and is further aggravated by significant spatial and temporal gaps within the data that does exist. Second, the observational studies that <u>are</u> available tend to concentrate on specific areas within the PAR, not the entire region. This focus is largely dictated by data availability, with regions such the Bering, Beaufort, and Chukchi Seas sampled more often than less accessible areas such as the East Siberian Sea or Canadian Archipelago. Furthermore, the variation in trend methodology and mechanism analysis across studies complicates direct trend comparisons between them. This study aims to address gaps in our current understanding by completing the following objectives:

(1) Leverage open sources to assemble the most comprehensive PAR carbonate system dataset to date.

(2) Use this data to identify spatially-dependent relationships between TA and SSS/SST.

(3) Use these correlations to transform widely-available SSS/SST data into a gridded TA dataset.

(4) Couple the TA dataset with a gridded surface pCO_2 product to fully resolve the carbonate system.

(5) Perform statistical analyses to quantify decadal surface acidification rates and identify primary drivers of change.

Table 1: Published works that report PAR surface trends in pCO_2, pH, and/or Ω_{Ar}. pCO_2, pH, and Ω_{Ar} trends are in μatm decade^{-1}, pH units decade^{-1}, and Ω_{Ar} units decade^{-1}, respectively. Studies are categorized as observation-based or model output. Observation-based means trends were derived from direct observations or on algorithmically-predicted data (*e.g.*, neural network). The subregion column refers to the closest-matching area from Figure 1. Figures listed in the notes column refer to figures from that publication.

Observation-based

Reference	**Subregion**	**Time Span**	**pCO_2 Rate**	**pH Rate**	**Ω_{Ar} Rate**	**Note**
Ma et al. (2023)	Bering, Aleutian, Gulf of Alaska	1982-2021	15.9	-0.017	-0.048	NP-SPSS (Fig. 3)
Lauvset et al. (2015)	Bering, Aleutian, Gulf of Alaska	1991-2011	7.4	-0.013	-	NP-SPSS (Fig. 1)
Ouyang et al. (2020b)	Arctic Ocean	1994-2017	46.0	-	-	Canada Basin (Fig. 2a)
Ouyang et al. (2020b)	Beaufort Sea	1994-2017	38.1	-	-	Canada Basin (Fig. 2a)
Qi et al. (2022)	Arctic Ocean	1994-2020	-	-0.086 to -0.031	-0.20 to -0.11	IC, NWCB, NECB (Fig 1a)
Qi et al. (2022)	Beaufort Sea	1994-2020	-	-0.057	-0.16	SCB (Fig 1a)
Zhang et al. (2020b)	Arctic, Beaufort Sea	1997-2007	-	-	-0.50	
Zhang et al. (2020b)	Arctic, Beaufort Sea	2007-2016	-	-	No Trend	

Model Output

Reference	**Subregion**	**Time Span**	**pCO_2 Rate**	**pH Rate**	**Ω_{Ar} Rate**	**Note**
Mathis et al. (2015)	Bering Sea Shelf	2011-2100	-	-	-0.07	
Mathis et al. (2015)	Chukchi Sea	2011-2100	-	-	-0.06	
Mathis et al. (2015)	Beaufort Sea	2011-2100	-	-	-0.06	
Pilcher et al. (2019)	Bering Sea Shelf	2003-2012	-	-	-0.40 to -0.25	
Pilcher et al. (2022)	Bering Sea Shelf	2010-2100	17.5 to 61.8	-0.045 to -0.015	-0.10 to 0.04	
Mortenson et al. (2020)	Beaufort Sea	1981-2015	21.3	-0.03	-0.04	Beauf. Shelf (Fig. 1)
Mortenson et al. (2020)	Arctic Ocean	1981-2015	12.6	-0.02	-0.05	Beauf. Basin (Fig. 1)
Mortenson et al. (2020)	Upper & Lower Archipelago	1981-2015	19.6	-0.03	-0.09	CPS (Fig. 1)
Gruber et al. (2012)	Arctic Ocean	1935-2064	-	-	-0.07	Approx. from Fig. 3

3. STUDY AREA

The PAR is where the North Pacific waters feed into the Arctic by passing over the shallow (<150 m depth) Bering Sea shelf and through the narrow (80 km wide) Bering Strait. This influx consists of saline, nutrient-rich Anadyr water from the eastern Russian coast and fresher, lower-nutrient Alaskan Coastal water from the western Alaskan coast (Grebmeier, 2012). These currents converge on the northern Bering Sea shelf and Chukchi Sea, driving primary productivity in one of the world's most productive marine ecosystems (Grebmeier et al., 2006; Grebmeier, 2012). The high primary productivity observed here is closely tied to its seasonal sea ice dynamics. Sea ice extent is typically at its highest in March and lowest in September. Figure 1 depicts the median March and September ice extent for the years 1981-2010. Historically, the waters within these geographical boundaries, such as the Bering Sea shelf and Chukchi sea, undergo seasonal changes in ice coverage. Areas south of the March extent are generally ice-free throughout the year, while regions north of the September line maintain year-round ice cover. Sea ice breakup and melting on the Bering Sea shelf and Chukchi Sea drives spring phytoplankton blooms by allowing more light to penetrate the water column and keeping nutrients at the surface through increased stratification (Grebmeier, 2012). Declining sea ice coverage has lengthened the growing season and led to the emergence of fall phytoplankton blooms. These blooms are facilitated by extended light availability due to ice, which reduces light penetration, forming later in the season, and the replenishment of surface nutrients through storm-induced upwelling (Waga and Hirawake, 2020). The cold, highly soluble water of the region combined with high primary productivity makes the Bering Sea shelf and Chukchi Sea exceptionally strong CO_2 sinks.

North of the Bering Strait, surface circulation in the Arctic sector of the PAR is dominated by the Beaufort Gyre. Situated between the continental shelves of the Chukchi Sea, Beaufort Seas, and Canadian Archipelago, the Beaufort Gyre is a clockwise-rotating surface circulation system that lies over the deepwater (mean depth 3.8 km) Canada Basin. The Beaufort Gyre is the largest freshwater reservoir in the Arctic. It contains approximately 25% of the Arctic Ocean's total freshwater due to freshwater discharge from Russian and North American rivers and, in recent decades, significant sea ice loss (Timmermans and Toole, 2023). Climate change-driven warming has caused significant sea ice decline in the Arctic (Chapman and Walsh, 1993; Walsh and Chapman, 2001; Kwok, 2018). This loss is particularly rapid in the PAR, with the East Siberian, Chukchi, and Beaufort Seas and the Beaufort Gyre exhibiting a sea ice cover decline of 10-30% per decade since 1979 (Timmermans and Toole, 2023). This is illustrated by the September 2012 ice extent (Figure 1), the lowest extent on record (Timmermans and Toole, 2023), which is significantly further north than the median September ice extent of the prior three decades.

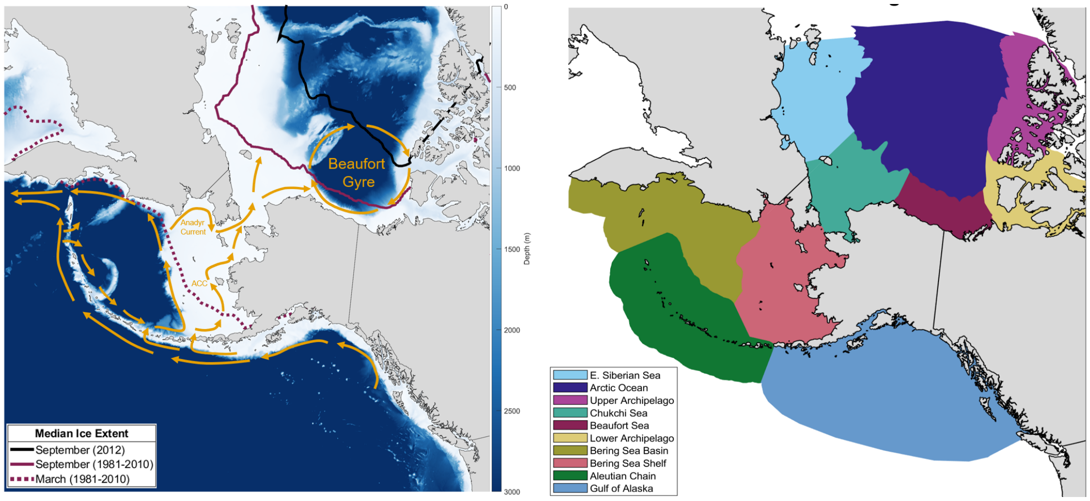

Figure 1: The Pacific Arctic Region (PAR). Left) Bathymetry is sourced from the General Bathymetric Chart of the Oceans (GEBCO 2023), ice extents from the National Snow and Ice Data Center. Right) The PAR divided into subregions using Marine Ecoregions of the World (Spalding et al., 2007), slightly modified to ensure complete coverage of the study area.

4. METHODS

4.1 Discrete Bottle Samples

The first step in quantifying acidification trends involves assembling a comprehensive set of field samples (*i.e.,* bottle samples), which will be utilized to identify inter-variable relationships for TA reconstruction, validate our carbonate system predictions, and propagate prediction errors to the final trend results. Discrete bottle samples were primarily sourced from the Global Ocean Data Analysis Project, GLODAP v.2022 (Lauvset et al., 2022), due to its extensive data coverage, rigorous quality control, and inclusion of relevant parameters. Specifically, GLODAP observations within the PAR containing at least one carbonate system parameter were extracted. The dataset was then expanded by leveraging online databases such as the National Centers for Environmental Information Ocean Carbon and Acidification Data System (NCEI-OCADS), the National Science Foundation's Arctic Data Center, the Japan Agency for Marine-Earth Science and Technology (JAMSTEC) data catalog, the PANGAEA data publisher, as well as individual publications. A comprehensive summary of the cruises used is provided in Appendix A. From these sources, only observations with a WOCE quality flag of 2 consisting of SSS, SST, depth, and at least one carbonate system parameter were selected.

Data was standardized to uniform units where necessary. For datasets lacking an expedition code, one was generated using the National Oceanographic Data Center's (NODC) standardized format contingent on the availability of the vessel's NODC identifier and cruise details. If the port departure date was unknown, the date of the earliest measurement was used. If the NODC identifier or research vessel's name was unavailable, a unique identifier was assigned. All pH data were confirmed as total scale. Observations reporting pH and pCO_2 at specific temperatures were converted to an in-situ value using CO2SYS (see section 4.4). For GLODAP observations, measurement uncertainty for each parameter was collected from individual cruise metadata. Otherwise, uncertainties of 4 μmol kg^{-1} for DIC and TA and 0.01 for pH were adopted per Lauvset et al. (2022). When data included two or three carbonate system parameters, the remaining parameters were calculated using CO2SYS, opting for the input pair that minimized calculation error (Dickson, 2010). Uncertainty in calculated carbonate system parameters was obtained using the CO2SYS 'errors' subroutine (Orr et al., 2018).

4.2 Gridded Datasets

A number of gridded datasets were used in this study as they are publicly accessible and provide wider spatial and temporal coverage than discrete bottle samples. The gridded datasets employed in this study are listed in Table 2. Each dataset had a monthly temporal resolution and was confined to a time period of January 1993 to December 2021. Although some datasets used in this study contain earlier data, the carbonate system in the PAR was rarely sampled prior to the 1990s. Therefore, we restricted the period of study such that we have sufficient field measurements for validation.

The MPI-SOM-FFN pCO_2 dataset is the output of a two-step neural network, detailed and validated in previous works (Landschützer et al., 2013; Landschützer et al., 2014; Landschützer et al., 2016), and expanded in 2023 to encompass the Arctic Ocean. This approach categorizes the global ocean into biogeochemically similar regions using a self-organizing map (SOM), then leverages a feed-forward neural network (FFN) to establish regional non-linear relationships between environmental variables (SSS, SST, atmospheric dry air CO_2 mixing ratio, mixed-layer depth, chlorophyll *a*) and surface pCO_2 observations from the Surface Ocean CO_2 Atlas (SOCAT v2022). These relationships were then applied to envi-

Table 2: The gridded datasets used in this study. The top four listed were directly used to solve the carbonate system as described in Section 4.4. The bottom five datasets were used for validation and results comparison. Note *a*) WOA silicate and phosphate data are a monthly climatology.

Dataset	**Spatial Resolution**	**Temporal Resolution**	**Variables Used**	**Uncertainty Included**	**Methodology**	**Reference**
			Datasets used for Analysis			
MPI-SOM-FFN (v2022)	1°x 1°	Monthly	pCO_2, Air-Sea Flux	No	Neural Network	Jersild et al. (2017)
Hadley EN4 (EN.4.2.2)	1°x 1°	Monthly	SSS	Yes	Objective Analysis	Good et al. (2013)
OI SST (v2)	1°x 1°	Monthly	SST	No	Objective Analysis	Reynolds et al. (2002)
WOA 2018	1°x 1°	Monthly[a]	Si, P	No	Objective Analysis	Garcia et al. (2019)
			Datasets used for Validation and Comparison			
OceanSODA-ETHZ (v2023)	1°x 1°	Monthly	pCO_2, pH, Ω_{Ar}	Yes	Neural Network	Gregor and Gruber (2021)
CMEMS-LSCE (r100)	1°x 1°	Monthly	pCO_2, pH, Ω_{Ar}	Yes	Neural Network	Chau et al. (2023)
CMEMS-LSCE (r25)	0.25°x 0.25°	Monthly	pCO_2, pH, Ω_{Ar}	Yes	Neural Network	Chau et al. (2023)
SOCAT (v2023)	1°x 1°	Monthly	fCO_2	Yes	Observational	Bakker et al. (2016)
ORAS5	0.25°x 0.25°	Monthly	Sea Ice Thickness	No	Reanalysis	Zuo et al. (2019)

ronmental parameter datasets, which offer broader spatial and temporal coverage than direct surface pCO_2 measurements, to produce a monthly gapless gridded surface pCO_2 dataset. The OceanSODA-ETHZ and CMEMS-LSCE datasets are similar neural network outputs but contain predicted fields for the entire carbonate system rather than just pCO_2. MPI-SOM-FFN was chosen for our primary analysis, rather than the full carbonate system datasets, because it is the only carbonate system dataset from Table 2 that offers gapless coverage of the Arctic Ocean.

4.3 TA Reconstruction

The discrete bottle samples from Section 4.1 were used to explore spatial relationships between TA, temperature, and salinity. Establishing these relationships allowed us to transform the gridded temperature and salinity datasets from Table 2 into a gridded TA dataset, thereby filling in the spatial and temporal data gaps of the bottle sample dataset. 7,148 TA measurements in the upper 10m across the PAR were used to develop TA prediction models. Various model-equation pairs were evaluated to predict TA. Four equations modeled TA as a function of different parameters: SSS (Equation 1), SSS and SST (Equation 2), SSS and SST with an interaction term (Alin et al., 2012) (Equation 3), and SSS and SST with second-order terms (Lee et al., 2006) (Equation 4).

$$TA = a + b(SSS) \tag{1}$$

$$TA = a + b(SSS) + c(SST) \tag{2}$$

$$TA = a + b(SSS) + c(SST) + d(SSS)(SST) \tag{3}$$

$$TA = a + b(SSS) + c(SST) + d(SSS)^2 + e(SST)^2 \tag{4}$$

Three linear regression models were applied to these equations: ordinary least squares (OLS), robust regression (with bisquare weighting, tuning constant = 4.685), and geographically weighted regression (GWR). The OLS and robust regression models were applied to distinct subregions (Figure 1) to account for the spatial variability in response-predictor relationships, a step not required for GWR.

GWR is an OLS variant where coefficients can vary spatially. It was implemented using the MATLAB Spatial Econometrics Toolbox (LeSage, 1999), which outputs gridded coefficient fields (*a*-*e* from Equations 1-4) that enable the coefficients to vary spatially. All GWR calculations were initially conducted in a polar stereographic projection to ensure uniform grid cell areas and avoid spatial distortion at high latitudes. Final results were then converted back to a 1°x 1° grid. This step was particularly important as the study area spans a broad latitudinal range (45°- 90°N).

A *k*-fold (k=10) cross-validation analysis was conducted for each model-equation pair. This consisted of dividing the dataset into ten equal subsets (nine for training and one for testing) and changing the test subset in each iteration such that all data points are used for validation. Model performance was assessed using mean absolute error (MAE, Equation 5) and mean bias error (MBE, Equation 6). The locally interpolated alkalinity regression (LIARv2) package (Carter et al., 2018) was also explored as a prediction solution.

$$MAE = \frac{\Sigma\ |y_{\text{Pred}} - y_{Obs}|}{N_{Obs}} \tag{5}$$

$$MBE = \frac{\Sigma\ (y_{\text{Pred}} - y_{Obs})}{N_{Obs}} \tag{6}$$

4.4 Carbonate System Calculations

TA was reconstructed by applying the best-performing TA prediction model-equation pair to gridded SSS and SST datasets. CO2SYS v2.1 (Lewis and Wallace, 1998) for MATLAB (van Heuven et al., 2011) was then used on the gridded TA, pCO_2, SSS, SST, silicate, and phosphate datasets to obtain monthly averaged 1°x 1° DIC, pH, $[H^+]$, and Ω_{Ar} fields. The K_1 and K_2 dissociation constants from Millero et al. (2006), K_{SO4} dissociation constants from Dickson et al. (1990), and the boron/chlorinity ratio from Uppström (1974) were used.

The gridded monthly DIC, $[H^+]$, and Ω_{Ar} fields were then validated against discrete bottle samples to assess their accuracy. To do so, bottle samples from the upper 10m were averaged to a 1°x1° grid at a monthly resolution. These gridded monthly averages were then compared to the reconstructed DIC, pH, and Ω_{Ar} fields to assess the accuracy of our predictions. A potential issue is the sporadic spatiotemporal distribution of discrete samples, which may not comprehensively reflect the average conditions of a grid cell for an entire month. To counteract this potential bias and enhance the representativeness of the data, we only considered a grid cell's monthly average valid if it included discrete samples from both the first and second halves of the month. While this criterion aimed to bolster the validation process, it is important to recognize that it still likely overestimates predictive error, resulting in a more conservative uncertainty estimate.

4.5 Salinity Normalization

sTA and sDIC were also calculated by normalizing TA and DIC values to a constant salinity, as described in Equations 7 and 8 (Friis et al., 2003). This normalization allows us to remove the impact of freshwater additions or removals on TA and DIC. For instance, rainwater dilutes surface seawater, lowering SSS and DIC, but does not affect sDIC. Processes independent of salinity, such as primary production, impact both DIC and sDIC. By comparing trends in normalized and non-normalized variables, we gain further insights into the underlying mechanisms affecting these variables. For example, identical trends in DIC and sDIC indicate that freshwater dynamics had a negligible effect on overall DIC trends.

$$sTA = \frac{TA - TA_{SSS=0}}{SSS} \cdot 34.5 + TA_{SSS=0} \tag{7}$$

$$sDIC = \frac{DIC - DIC_{SSS=0}}{SSS} \cdot 34.5 + DIC_{SSS=0} \tag{8}$$

TA$_{SSS=0}$ and DIC$_{SSS=0}$ are the zero-salinity TA and DIC values observed at any given grid cell. TA$_{SSS=0}$ was obtained from the GWR intercept field (*i.e.*, coefficient a) from Equation 1. DIC$_{SSS=0}$ was also calculated by running a GWR where DIC is a function of SSS. The spatial variation in TA$_{SSS=0}$ and DIC$_{SSS=0}$ is influenced by local biogeochemical processes that modify the linear relationship between TA and SSS, and DIC and SSS. For instance, the Mackenzie River's (endmember properties SSS=0, DIC=1390 μmol kg^{-1}, TA=1540 μmol kg^{-1}) (Mol et al., 2018) discharge into the Beaufort Sea elevates TA$_{SSS=0}$ and DIC$_{SSS=0}$ values compared to regions influenced solely by rainwater, which has negligible SSS, DIC, and TA endmember values. TA$_{SSS=0}$ and DIC$_{SSS=0}$ are also affected by sea-ice meltwater, upwelling, surface water mass exchange, calcification, and primary production due to their impact on the local linear relationship between TA and SSS, and DIC and SSS (Friis et al., 2003). Incorporating TA$_{SSS=0}$ and DIC$_{SSS=0}$ into the normalization procedure yields more accurate sTA and sDIC values by accounting for these biogeochemical processes.

4.6 Statistical Trend Methods

Once the carbonate system is reconstructed, we can apply statistical trend methods to determine acidification rates. However, detecting and quantifying trends in the marine carbonate system requires careful consideration due to its non-linear response to external influences such as increasing atmospheric CO_2 and concurrent climate change-driven impacts on DIC, TA, SSS, and SST. This task is further nuanced by inherent seasonality in oceanographic variables, meaning a robust statistical approach is more suitable than simple linear regression. Therefore, we utilized the seasonal Kendall trend test and Theil-Sen estimator for trend analysis in this study.

The seasonal Kendall trend test (Hirsch et al., 1982), a non-parametric (*i.e.*, distribution-free) method, excels in identifying both the presence and direction of monotonic trends in seasonal data. This test determines whether there is an upward or downward trend between every possible pair of data points. When no overall trend exists, the number of upward and downward trends between these pairs should be approximately equal. In contrast, an underlying trend would yield more pairwise trends in one direction than could be explained by random chance. Seasonality is handled by only comparing data points within the same month, then integrating individual monthly statistics into a single overall trend.

While the seasonal Kendall trend test identifies trend direction in seasonal data, it does not measure trend magnitude. This limitation is addressed by the seasonal Theil-Sen estimator (Sen, 1968). Similar to the seasonal Kendall Trend test, this non-parametric method quantifies trend magnitude by first finding the slopes between all pairs of data points in a grid that share the same month (*e.g.*, all June values). This produces a distribution of slope values, the median of which is the trend value for that month. Repeating this process for every month of the year yields twelve slope values which are then combined to form the overall trend.

The seasonal Kendall trend test and Theil-Sen estimator are widely used in environmental trend analysis. This combined approach has been extensively applied to study long-term trends in environmental parameters such as salinity (Wiseman et al., 1990), chemical concentrations (Smith et al., 1982; Lehmann et al., 2005), aquatic heatwaves (Kaushal et al., 2010; Tassone et al., 2021; Tassone et al., 2023), sea-level rise (Taibi and Haddad, 2019; Nguyen et al., 2022), and phytoplankton blooms (Friedland et al., 2018).

4.7 Ocean Acidification Driver Decomposition

After determining decadal acidification trends, the next step is decomposing the total trends into their individual drivers, revealing which processes drive or mitigate observed acidification rates. A discrete change in a calculated carbonate system parameter (y) is caused by changes in its drivers (X) relative to the sensitivity of y to these changes (*e.g.*, $\delta y/\delta X$). This is represented by the first-order terms of a Taylor expansion (Takahashi et al., 1993; Landschützer et al., 2018) given by Equation 9. The drivers (X) were DIC, TA, SSS, and SST. DIC was used in lieu of pCO_2 due to its conservative nature. Furthermore, nutrients were omitted as drivers because climatological values lack long-term trends, though their values were used in sensitivity calculations.

$$\Delta y = \sum_{\text{X = DIC, TA, SSS, SST}} \left(\frac{\delta y}{\delta X} \cdot \Delta X \right) \tag{9}$$

To compare the impact of changing drivers and sensitivities across subregions with different baseline Ω_{Ar} and $[H^+]$ values, we replaced the sensitivity term in Equation 9 with relative sensitivities (ω_X and β_X) given by Equations 10 and 11.

$$\omega_X = \frac{1}{\Omega_{Ar}} \cdot \frac{\delta \Omega_{Ar}}{\delta X} \tag{10}$$

$$\beta_X = \frac{1}{[H^+]} \cdot \frac{\delta [H^+]}{\delta X} \tag{11}$$

Consider a scenario where DIC increases by 10 μmol kg^{-1} in both the Arctic and subarctic Pacific. Assuming $\delta\Omega_{Ar}/\delta DIC = -0.01$ Ω_{Ar} units per μmol kg^{-1}, this change in DIC would decrease Ω_{Ar} by 0.1 units in both locations. However, this value does not reflect that this constitutes a 10% Ω_{Ar} reduction in the Arctic ($\Omega_{Ar} \approx 1$ units) but only a 5% decline in the subarctic Pacific ($\Omega_{Ar} \approx 2$ units). Using relative sensitivities would reflect that the impact of this change in the Arctic (-0.1 Ω_{Ar} units / 1 Ω_{Ar} units = -0.1) is double that of the subarctic Pacific (-0.1 Ω_{Ar} units / 2 Ω_{Ar} units = -0.05). Therefore, replacing the sensitivities in Equation 9 with the relative sensitivities of Equations 10 and 11 results in the updated Taylor expansions given by Equations 12 and 13. Note that, in order to maintain proper units and account for the added 1/Ω_{Ar} and 1/[H$^+$] terms, we must multiply each term by Ω_{Ar} and [H$^+$], respectively (*e.g.*, 1/$\Omega_{Ar} \cdot \Omega_{Ar}$ cancel out, maintaining the equality in Equation 9).

$$\Delta\Omega_{Ar} = \sum_{\text{X = DIC, TA, SSS, SST}} (\omega_X \cdot \Omega_{Ar} \cdot \Delta X) \tag{12}$$

$$\Delta[H^+] = \sum_{\text{X = DIC, TA, SSS, SST}} \big(\beta_X \cdot [H^+] \cdot \Delta X\big) \tag{13}$$

The same concept holds true for trends: a trend in y must be due to trends in its drivers and/or sensitivities. Taking the derivative of Equations 12 and 13 with respect to time using the product rule gives the total trends in Ω_{Ar} (Equation 14) and [H$^+$] (Equation 15), where X = DIC, TA, SSS, SST.

$$\frac{d\Omega_{Ar}}{dt} = \sum_{\mathrm{X}} \left(\underbrace{\frac{d\omega_X}{dt} \cdot \overline{\Omega}_{Ar} \cdot \Delta X}_{\text{change in sensitivity}} + \underbrace{\overline{\omega}_X \cdot \frac{d\Omega_{Ar}}{dt} \cdot \Delta X}_{\text{mass effect}} + \underbrace{\overline{\omega}_X \cdot \overline{\Omega}_{Ar} \cdot \frac{d\Delta X}{dt}}_{\text{change in driver}} \right) \tag{14}$$

$$\frac{d[H^+]}{dt} = \sum_{\mathrm{X}} \left(\underbrace{\frac{d\beta_X}{dt} \cdot \overline{[H^+]} \cdot \Delta X}_{\text{change in sensitivity}} + \underbrace{\overline{\beta_X} \cdot \frac{d[H^+]}{dt} \cdot \Delta X}_{\text{mass effect}} + \underbrace{\overline{\beta_X} \cdot \overline{[H^+]} \cdot \frac{d\Delta X}{dt}}_{\text{change in driver}} \right) \tag{15}$$

Sensitivities were calculated for each grid cell by inputting long-term averages of DIC, TA, SSS, SST, silicate, and phosphate fields into the CO2SYS ‘derivnum’ subroutine. ΔX is the discrete change in driver from 1993 to 2021. All time derivatives were calculated using the seasonal Theil-Sen estimator except for dΔX/dt, which was calculated by dividing ΔX by 29 years. Variables denoted by a bar on top indicate the long-term mean for the grid cell. This decomposition yields three distinct terms for each driver: change in sensitivity, mass effect, and change in the driver itself, the sum of which equals the contribution of that driver to the total trend in Ω_{Ar} or [H$^+$].

The “change in sensitivity” term illustrates how trends in Ω_{Ar} and [H$^+$] are influenced by shifts in their sensitivities to various drivers (ω_X and β_X). The “change in driver” term captures the impact of driver trends (*e.g.*, rising SST) on the overall Ω_{Ar} and [H$^+$] trends. The “mass effect” term accounts for the influence of changes in Ω_{Ar} and [H$^+$], relative to their sensitivities and changing drivers, on their own trends. This term is primarily a mathematical consequence of using relative sensitivities – that is, it arose because we introduced Ω_{Ar} and [H$^+$] into the right-hand side of Equations 12 and 13. The implications of the mass effect term, while largely unexplored in the current literature, may reflect the interconnectedness of the marine carbonate system. According to the principles of chemical equilibrium (Le Chatelier, 1884), the marine carbonate system as a whole is affected when the concentrations of chemical species change. Thus, an underlying trend in [H$^+$] or Ω_{Ar} ($i.e.$, $[CO_3^{2-}]$) could influence the carbonate system, which in turn could affect the overall trend in [H$^+$] or Ω_{Ar}. Although the specific implications of the mass effect term are not well-documented, its inclusion is justified by the benefit of relative sensitivities in our analysis. Moreover, our approach to driver decomposition, which follows the methodology established by Ma et al. (2023), ensures methodological alignment with previously published work. This uniformity facilitates straightforward comparisons of results across studies.

4.8 Error Propagation and Trend Determination

The validity of final trend results depends on the accuracy of carbonate system variables. To ensure reliability in reported results, error was meticulously propagated through to the final trends and drivers.

The MPI-SOM-FFN pCO$_2$ dataset did not include gridded uncertainty values. Although the method demonstrates near-zero bias and <20 μatm RMSE (Landschützer et al., 2016), its effectiveness in the Arctic Ocean has not been evaluated in the literature. To account for this, we compared the pCO$_2$ data to SOCAT v2023 and discrete bottle samples, averaged the residuals on a 1°x1° grid, and interpolated spatial gaps to create a continuous pCO$_2$ uncertainty field. Residuals from the TA prediction model (Section 4.3) were calculated in the same manner. We assumed spatial pCO$_2$ and TA uncertainty was consistent over time due to insufficient spatiotemporal data coverage to support time-dependent uncertainty fields. The CO2SYS 'errors.m' subroutine (Orr et al., 2018) was used to determine uncertainty in calculated variables (DIC, pH, [H$^+$], Ω_{Ar}) by incorporating gridded pCO$_2$ and TA uncertainty into carbonate system calculations (Section 4.4). In addition to pCO_2 and TA uncertainty, the calculation error of a carbonate system variable (y) is also a function of the state of the carbonate system per Equation 16.

$$\mathrm{y}_{Err} = \mathrm{errors.m}(\mathrm{pCO_2},\ \mathrm{pCO}_{2Err},\ \mathrm{TA},\ \mathrm{TA}_{Err},\ \mathrm{SSS},\ \mathrm{SST}) \tag{16}$$

This adds both a spatial and seasonal aspect to the uncertainty of calculated variables. For example, calculation uncertainty increases with salinity for DIC, $[H^+]$, and Ω_{Ar}. Conversely, lower temperatures results in lower calculation error for DIC and Ω_{Ar}, but higher error for $[H^+]$ (see Appendix B). This means that, although seasonality was not explicitly taken into account for gridded pCO_2 and TA uncertainty, inherent seasonality in monthly pCO_2, TA, SSS, and SST values induce a partial seasonal dependence into the uncertainty of monthly DIC, pH, $[H^+]$, and Ω_{Ar} values. This results in a unique uncertainty value for every calculated carbonate system variable for every month at every location, which was then accounted for in trends and driver calculations using a bootstrap approach.

Bootstrapping the seasonal Kendall trend test involved re-assigning each monthly mean in every grid cell a random value within its uncertainty range before conducting the test. Repeating this procedure 1,000 times yielded a normally-distributed set of 1,000 p-values and trend directions at every grid cell. A grid cell's trend direction was deemed statistically significant if at least 95% of the bootstrapped p-values were below 0.05 with a consistent trend direction.

Trend magnitude and uncertainty was calculated using a similar approach: every monthly mean at every grid cell was re-assigned a random value within its uncertainty range, then the slope of each grid cell's time series was computed using the seasonal Theil-Sen estimator. Repeating 1,000 times yielded a normally-distributed set of 1,000 slopes for each grid cell, the mean of which was used as the trend magnitude and the 95% confidence interval the trend uncertainty.

A bootstrap approach was also utilized in driver decomposition by solving Equations 14 and 15 1,000 times at every grid cell. An added benefit of the bootstrap approach is that by accounting for uncertainty in carbonate system variables, it also reflects uncertainty in sensitivities (ω_X and β_X). This is because sensitivities are a function of the entire carbonate system, so applying error to carbonate parameters before calculating sensitivities reflects this uncertainty. Decomposed drivers were then calculated using carbonate parameters and sensitivities with applied error, thereby extending uncertainty into the final driver results. Similar to the total trends, each decomposed driver is calculated 1,000 times at each grid cell, the mean of which is the final reported value and the 95% confidence interval its uncertainty.

5. RESULTS

5.1 Discrete Bottle Samples

A total of 295 oceanographic cruises, consisting of 216 from GLODAP and 79 from other sources, were used in this study. The data, ranging from October 1973 to November 2021, yielded a total of 86,750 discrete samples in time and space (latitude, longitude, depth) with at least one carbonate system parameter. This dataset included 27,227 surface samples (from the upper 10m) and 59,523 samples collected at various depths from 5,668 vertical casts. Post-processing through CO2SYS produced 76,421 DIC, 62,885 TA, 58,845 [H^+], and 55,653 pCO_2 measurements, culminating in 253,804 total carbonate parameter measurements. Notably, 3% (6,997) of these measurements did not report measurement errors.

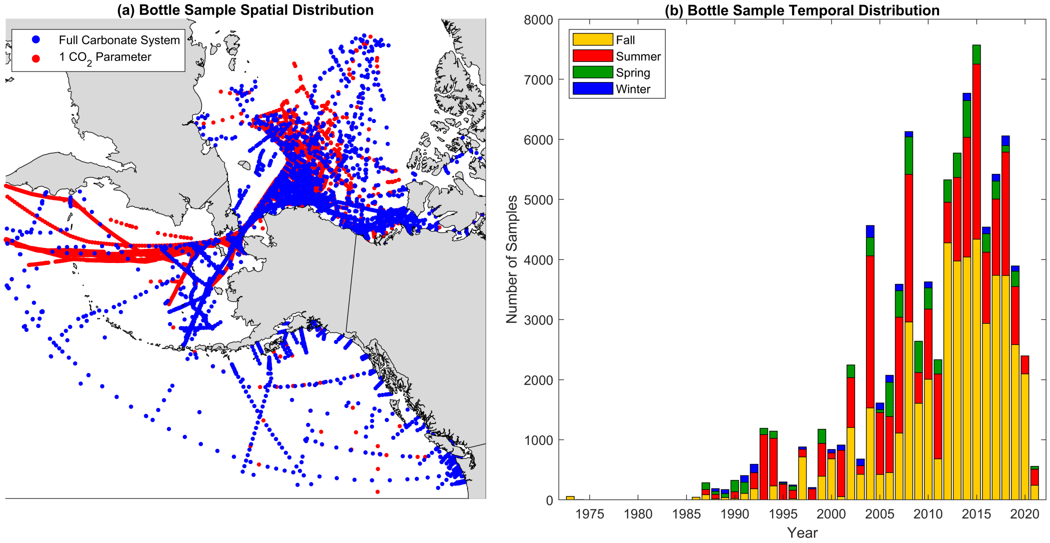

Figure 2: (a) The two-dimensional spatial distribution of the discrete bottle samples. Blue points denote locations the entire carbonate system is measured and/or calculated. Red points are locations with only one carbonate parameter. (b) The temporal distribution of the discrete bottle samples. Each bin is a year, subdivided into boreal seasons. The vast majority of observations occur in summer and fall when sea ice is less likely to inhibit vessel access.

5.2 TA Prediction

TA prediction model and equation performance are summarized in Table 3. LIAR ranked as the least accurate (MAE 40 μmol kg^{-1}) and most biased (MBE 16.7 μmol kg^{-1}) method, with robust regression performing only marginally better in accuracy (MAE 33 to 35 μmol kg^{-1}) and bias (MBE -15 to -9 μmol kg^{-1}). OLS was the least biased method (MBE -0.05 to -0.07 μmol kg^{-1}) across all equations, but was less accurate (MAE 34 to 35 μmol kg^{-1}) than GWR. GWR outperformed OLS, robust regression, and LIAR in both MAE and R^2 across all equations. Pairing Equation 2 with GWR yielded the best results, with an MAE of 23 μmol kg^{-1}, an R^2 of 0.93, and effectively zero bias (MBE -0.01 μmol kg^{-1}) as depicted in Figure 3. Consequently, Equation 2-GWR was selected as the TA prediction method for this study. While SSS is the primary determinant of TA, incorporating the SST term accounts for additional processes. For instance, some subregions undergo seasonal shifts in water masses with distinct TA-SSS relationships. Since water masses are identified through both their temperature and salinity, including the SST term enhances TA prediction accuracy in these scenarios. Moreover, temperature-related processes, such as primary productivity, sea ice melt, and riverine inputs, influences the TA-SSS relationship, which the SST term can partially address. In regions unaffected by these processes, the SST term's contribution would effectively be null, thereby not compromising our ability to predict TA. Further details, including subregion-specific performance metrics for each model-equation pair, are provided in Appendix C.

Table 3: 10-fold cross validation results of all TA prediction model-equation pairs for the entire PAR. MAE and MBE (bias) are in μmol kg^{-1}. Each model-equation pair was trained and validated on the same 7,146 surface samples.

	OLS			**Robust**			**GWR**		
	MAE	**Bias**	R^2	**MAE**	**Bias**	R^2	**MAE**	**Bias**	R^2
Eq 1	35	-0.06	0.85	34	-9.49	0.84	24	0.13	0.92
Eq 2	34	-0.06	0.85	33	-11.3	0.83	23	-0.01	0.93
Eq 3	34	-0.05	0.86	33	-11.2	0.83	23	-0.33	0.93
Eq 4	34	-0.07	0.85	35	-15.2	0.70	23	0.96	0.92
LIAR: MAE 40 μmol kg^{-1}, Bias 16.7 μmol kg^{-1}, R^2 = 0.82									

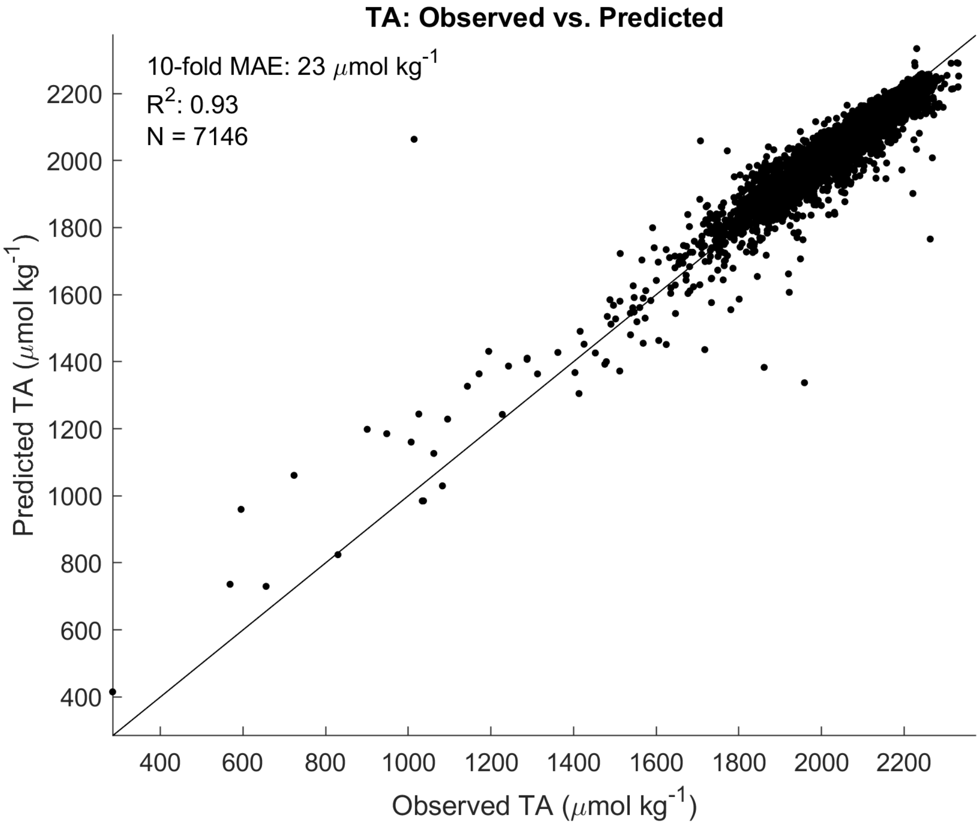

Figure 3: The measured TA of discrete bottle samples plotted against the TA predicted by Equation 2-GWR as described in Section 4.3.

5.3 Carbonate System Uncertainty

The spatial distribution of uncertainty (MAE) and bias (MBE) for our TA prediction method and the MPI-SOM-FFN pCO_2 dataset are presented in Figure 4. The MAE plots (Figures 4 (a) and (b)) represent the gridded TA and pCO_2 uncertainty fields used for error propagation. The MAE and MBE fields were calculated by comparing predicted values to discrete measurements (7,146 for TA and 2.2 million for pCO_2) as detailed in Section 4.8.

Figure 4 (a) and (c) provides detailed insight into the accuracy of our TA prediction methodology and offers a more nuanced perspective than the aggregate statistics of Table 3. While the overall TA MAE is 23 μmol kg^{-1}, the vast majority (76%) of the study area exhibits a TA MAE below 23 μmol kg^{-1}. However, highly localized coastal areas in the Beaufort Sea, Gulf of Alaska, and lower Canadian Archipelago show TA MAE values as high as 80 μmol kg^{-1}, skewing the overall average. While bias is consistently low and does not favor a particular direction across the region, the same coastal areas with high TA MAE also exhibit bias as large as ± 40 μmol kg^{-1}, significantly higher than the overall TA MBE of -0.1 μmol kg^{-1} may suggest.

Comparing the MPI-SOM-FFN pCO_2 dataset to discrete field samples yielded a pCO_2 MAE of 36 μatm and pCO_2 MBE of -16 μatm for the entire region. Similar to TA, the pCO_2 MAE and MBE fields (Figure 4 (b) and (d)) highlight the spatial variability of prediction accuracy and bias not captured in the overall averages. The MPI-SOM-FFN pCO_2 fields exhibited low error (0-40 μatm) and bias (< 10 μatm) in open-ocean subregions such as the Arctic Ocean and Gulf of Alaska. Predictive error and bias generally increased in coastal waters (MAE 40-80 μatm, MBE 20-40 μatm) with certain areas – such as the southeast Alaskan coast and pockets of the Bering Sea shelf – exhibiting errors and bias as high

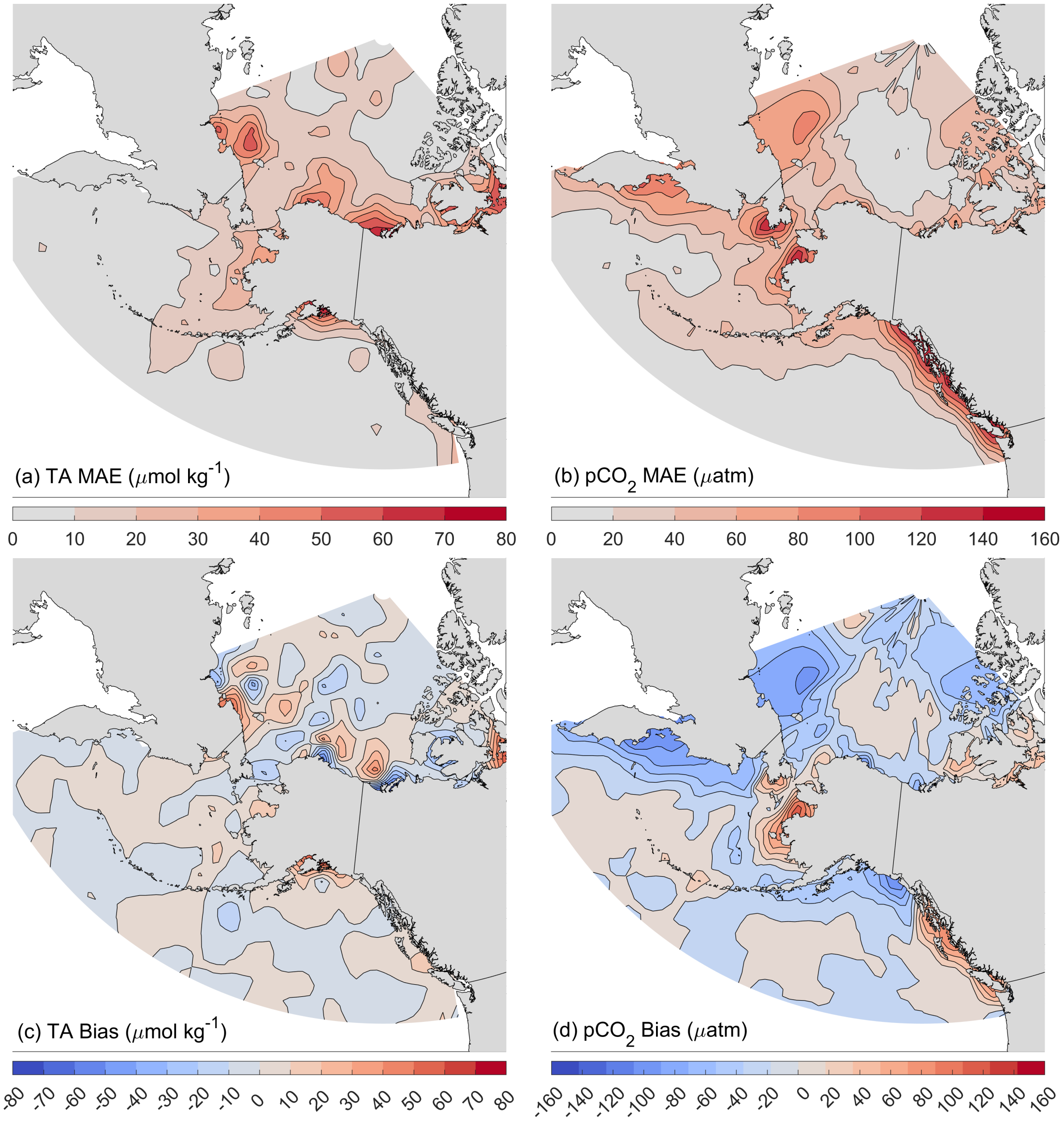

Figure 4: (a) and (b) display the spatial MAE of TA and pCO$_2$, also referred to as gridded TA/pCO$_2$ uncertainty or TA/pCO$_2$ uncertainty fields. (c) and (d) are the spatial distribution of MBE.

as 140 μatm and 80 μatm. Our MAE/MBE calculation methodology, which involves comparing discrete pCO_2 measurements (which vary between 58 - 1,000 μatm (Bakker et al., 2016)) to the predicted monthly average of a 1°x1° grid cell, inherently leads to an increase in error closer to shore where pCO_2 exhibits higher natural variability. This discrepancy arises because a monthly 1°x1° dataset lacks the spatial or temporal resolution necessary to capture such fine-scale processes. Additionally, the sampling distribution within a grid cell for a given month may not accurately represent the average monthly conditions, further contributing to the potential for increased error in these areas. Overall, MPI-SOM-FFN tends to underestimate pCO_2, evidenced by the overall MBE of -16 μatm, except for the southeast Alaskan Coast and eastern Bering Sea shelf, which show a positive bias.

The spatial distribution of calculation uncertainty in DIC, Ω_{Ar}, and $[H^+]$ are presented in Figures 5 (a)-(c). These were created by averaging all monthly calculation uncertainty values at each grid cell and smoothing spatially using a 2D moving mean with a 3°x3° window. While the monthly uncertainty fields were used for error propagation, the averaged and smoothed uncertainty fields presented in Figure 5 (a)-(c) solely serve to give a general representation of prediction confidence throughout the region. The area-weighted mean calculation uncertainty of these fields are 18.5 μmol kg^{-1} for DIC, 0.153 units for Ω_{Ar}, and 0.712 nmol kg^{-1} for $[H^+]$. DIC, Ω_{Ar}, and $[H^+]$ fields were then compared to discrete bottle samples as detailed in Section 4.4 and presented in Figures 5 (d)-(f). These comparisons show low prediction bias for all three variables: -2.6 μmol kg^{-1} for DIC, -0.07 units for Ω_{Ar}, and 0.21 nmol kg^{-1} for $[H^+]$.

Perhaps more relevant than the absolute MAE values of bottle comparisons are their agreement with overall calculation uncertainty. If the MAE values calculated by comparing predicted fields to discrete measurements are similar to the overall

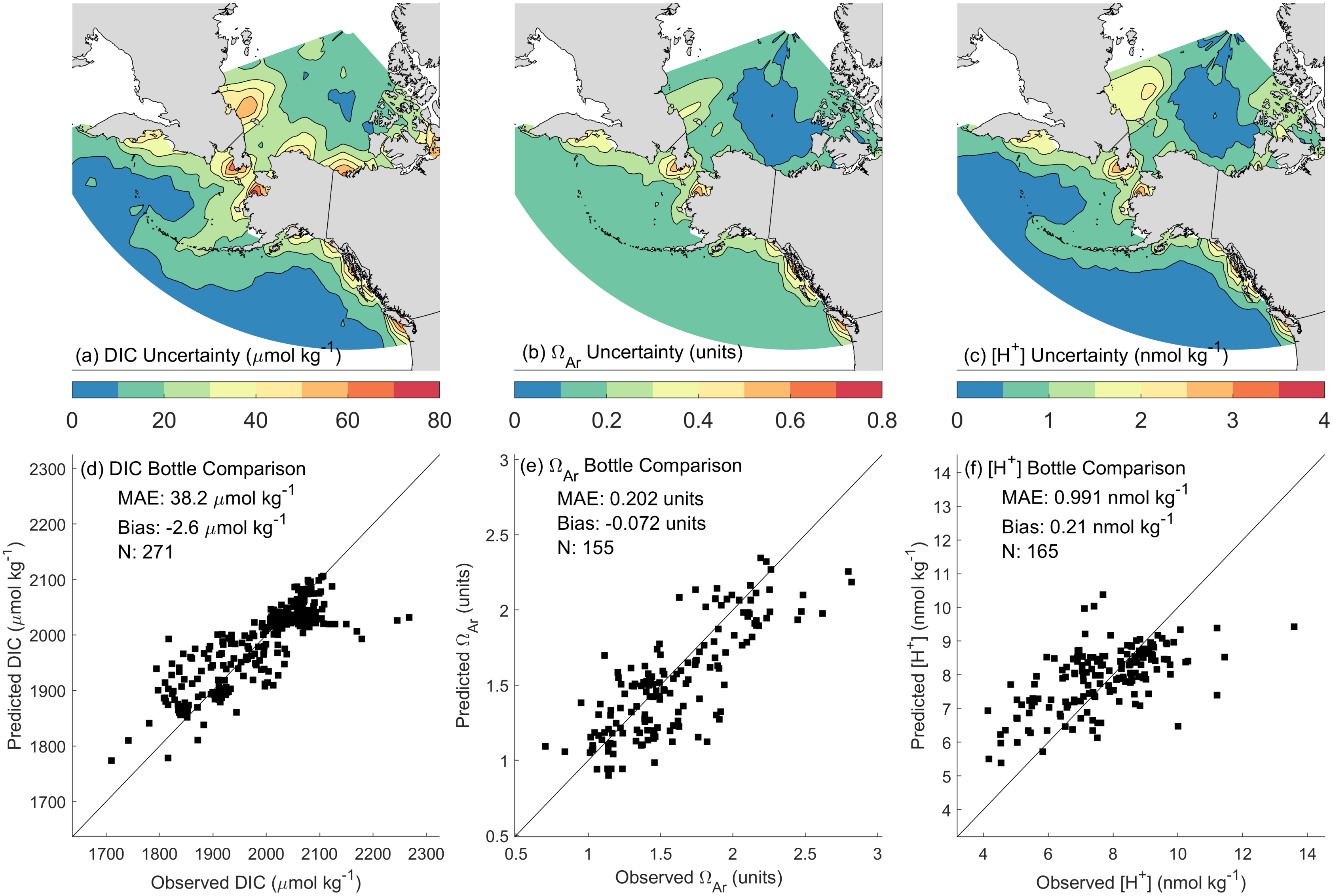

Figure 5: (a)-(c) Monthly calculation uncertainties, determined using Equation 16, averaged across the entire time series and spatially smoothed to give a general representation of calculation uncertainty for predicted DIC, Ω_{Ar}, and [H$^+$] fields. (d)-(f) Predicted DIC, Ω_{Ar}, and [H$^+$] fields compared to discrete bottle samples that were averaged into 1°x1° grid cells at a monthly resolution.

uncertainty calculated using ‘errors.m’ (Section 4.8), this would indicate that the DIC, Ω_{Ar}, and [H$^+$] uncertainty fields accurately represent the actual uncertainty in their predicted values. This validation is necessary because the uncertainty of final carbonate system trends rely on the uncertainty of monthly mean values due to our bootstrap approach. The Ω_{Ar} bottle comparison MAE of 0.202 units closely matches the mean calculation uncertainty of 0.153 units. Likewise, the [H$^+$] bottle comparison MAE of 0.999 nmol kg^{-1} corresponds well with the mean calculation uncertainty of 0.712 nmol kg^{-1}. However, the DIC bottle comparison MAE of 38.2 μmol kg^{-1} is double the mean calculation uncertainty of 18.5 μmol kg^{-1}, suggesting our error accounting may underestimate DIC uncertainty. The findings presented in Figure 5 indicate low bias in DIC, Ω_{Ar}, and [H$^+$] predictions and accurate error propagation methodology, albeit with slightly overconfident DIC uncertainties.

5.4 Regional Decadal Trends

Figure 6 illustrates the seasonal Kendall trend test results for the period of January 1993 to December 2021. These results indicate widespread surface acidification across the PAR characterized by rising pCO$_2$ and declining pH and Ω_{Ar}. The Bering Sea shelf and southern Alaskan coast are notable exceptions as they show either no trend or basificiation trends for pCO$_2$, pH, and Ω_{Ar} (Figure 7). The PAR can be clearly delineated into three distinct zones based on trend magnitude and direction: the Northern PAR (subregions: E. Siberian Sea, Arctic Ocean, Upper Archipelago, Chukchi Sea, Beaufort Sea, Lower Archipelago), the Bering Sea shelf, and the Southern PAR (subregions: Bering Sea basin, Aleutian Chain, Gulf of Alaska). Carbonate system variable trends for each zone are presented in Table 4. For each variable, every grid cell has a distinct trend and trend uncertainty calculated via the bootstrap method. The mean trend for each zone was derived by computing the area-weighted average of all grid cell trend values within the zone. The trend uncertainty for each zone was calculated by taking the area-weighted average of all grid cell trend uncertainty values within the zone. Thus, within a zone, certain grid cells may exhibit trend or trend uncertainty values that deviate from the zone averages presented in Table 4.

Table 4: Area-weighted trends and trend uncertainties for each zone from January 1993 to December 2021. SST has no trend uncertainty due to a lack of monthly SST uncertainty values as indicated in Table 2.

Parameter	**Northern PAR**	**Bering Sea Shelf**	**Southern PAR**	Units ($decade^{-1}$)
pCO_2	36.311 ± 3.459	-1.216 ± 4.263	14.181 ± 1.941	μatm
$[H^+]$	0.851 ± 0.082	-0.041 ± 0.092	0.281 ± 0.043	$nmol\ kg^{-1}$
pH	-0.047 ± 0.004	0.002 ± 0.005	-0.015 ± 0.002	$pH\ units$
Ω_{Ar}	-0.121 ± 0.013	0.031 ± 0.018	-0.040 ± 0.012	$\Omega_{Ar}\ units$
DIC	3.611 ± 2.13	-0.286 ± 2.302	4.397 ± 1.084	$\mu mol\ kg^{-1}$
sDIC	15.840 ± 2.136	-4.631 ± 2.299	4.689 ± 1.059	$\mu mol\ kg^{-1}$
TA	-12.828 ± 1.676	2.705 ± 1.294	-0.542 ± 0.544	$\mu mol\ kg^{-1}$
sTA	-0.303 ± 1.439	0.031 ± 1.191	-0.069 ± 0.477	$\mu mol\ kg^{-1}$
SSS	-0.211 ± 0.067	0.054 ± 0.031	0.010 ± 0.010	psu
SST	0.042	0.243	0.181	$^\circ C$

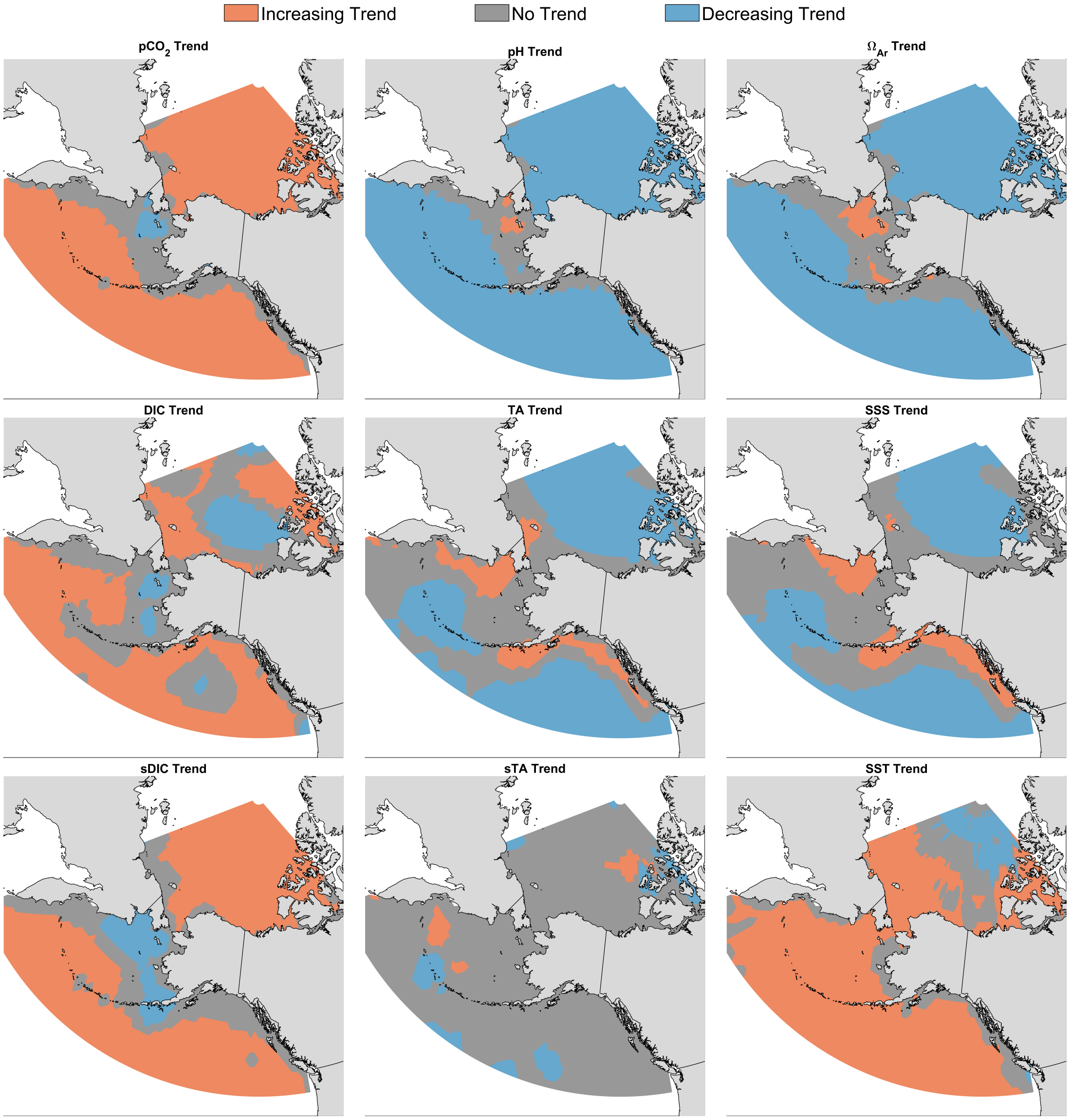

Figure 6: A seasonal Kendall trend test was conducted 1,000 times at each grid cell as outlined in Section 4.8. Areas in orange (increasing trend) and in blue (decreasing trend) had a positive and negative mean Mann-Kendall statistic, respectively, with more than 95% of bootstrapped p-values below 0.05. Locations in grey (no trend) are those where <95% of the bootstrapped values had a p-value <0.05. This does not mean the result is necessarily statistically insignificant, but rather we failed to reject the null hypothesis of no trend. A "no trend" result signifies either the genuine absence of a trend or the presence of a trend that is undetectable due to high uncertainty. [H^+] results are omitted as they mirror the pH results.

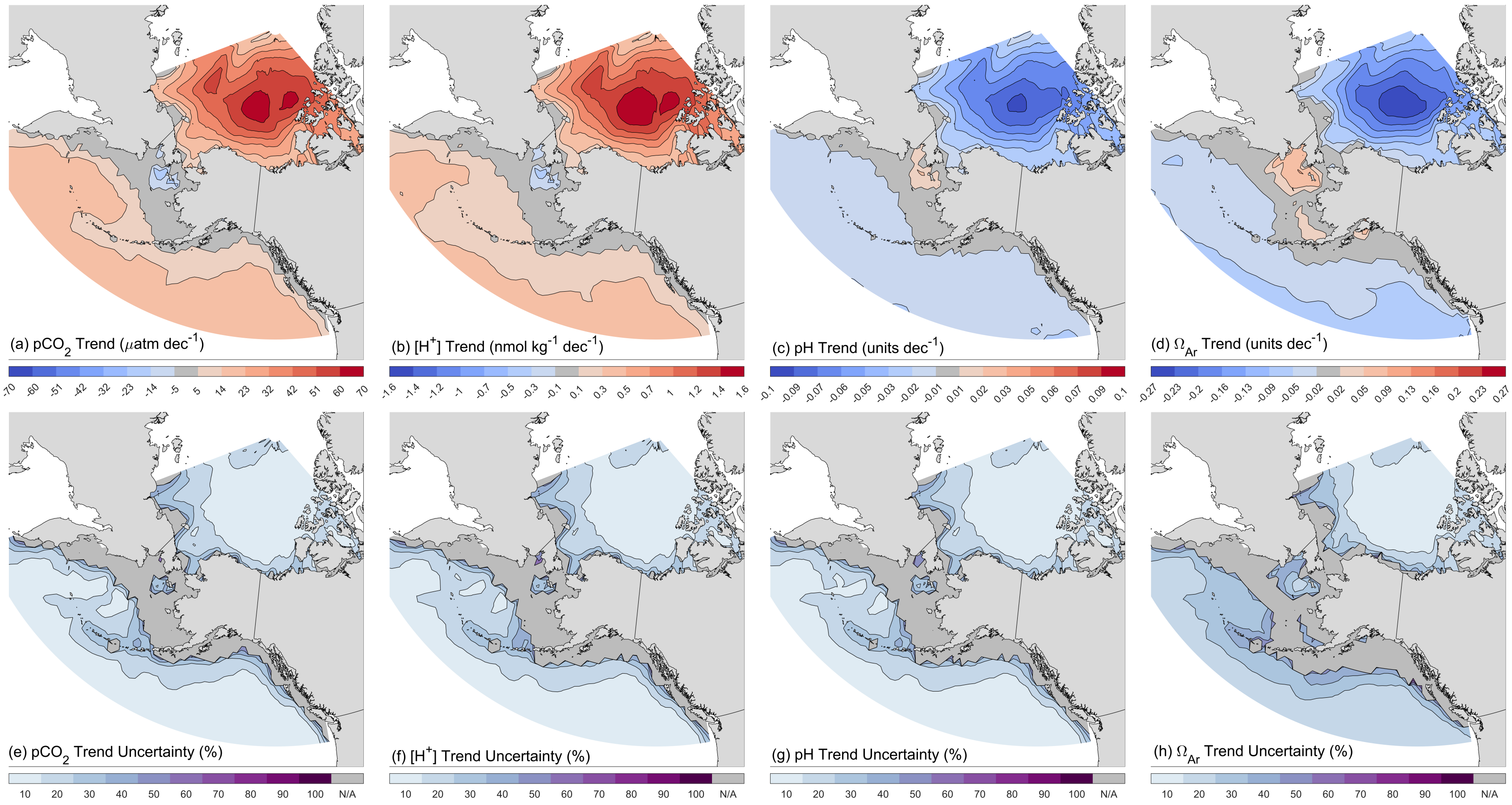

Figure 7: The decadal trend (1993-2021) and relative trend uncertainty for [H$^+$], pH, and Ω_{Ar} determined via the bootstrapped seasonal Theil-Sen estimator approach defined in Section 4.8. Grey denotes grid cells with no statistically significant trend (Figure 6).

5.4.1 Northern PAR Trends

The Northern PAR exhibits the most pronounced acidification rates in this study with an average pCO_2 increase of 36 μatm decade^{-1}, [H$^+$] increase of 0.851 nmol kg^{-1} decade^{-1}, a pH decrease of -0.047 units decade^{-1}, and an Ω_{Ar} rate of -0.121 units decade^{-1}. The Arctic Ocean subregion (and the Beaufort Gyre specifically) is the epicenter of this acidification, showing surface acidification rates 2-4 times higher than the global average, in line with prior observational and biogeochemical modeling studies (Table 1). The highest observed decadal trends for a grid cell within the Northern PAR are 65 μatm decade^{-1} for pCO_2, 1.6 nmol kg^{-1} decade^{-1} for [H$^+$], -0.089 pH units decade^{-1}, and -0.263 Ω_{Ar} units decade^{-1} (Figure 7). Moreover, substantial declines in SSS (-0.211 psu decade^{-1}), and therefore TA (-12.8 μmol kg^{-1} decade^{-1}), characterized the Northern PAR. There was no statistically significant trend for sTA (-0.3 ± 1.4 μmol kg^{-1} decade^{-1}). sDIC rose consistently (15.8 μmol kg^{-1}) but the overall DIC trend was significantly lower (3.6 μmol kg^{-1}). The wide range between zone-averaged sDIC and DIC trends arose because certain locations within the Northern PAR exhibited a decline in surface DIC, a pattern likely tied to the extensive SSS reduction and further discussed in Section 6.2. Warming (0.04°C decade^{-1}) occurred across the Northern PAR but was less pronounced than the Bering Sea shelf and Southern PAR.

5.4.2 Bering Sea Shelf Trends

On average, the Bering Sea shelf exhibited no discernible trend for pCO_2 (-1 ±4 μatm decade^{-1}), [H$^+$] (-0.041 ±0.092 nmol kg^{-1} decade^{-1}), or pH (0.002 ±0.005 units decade^{-1}), but did show a clear basificiation trend for Ω_{Ar} (0.031 ±0.018 units decade^{-1}). Figures 6 and 7 show that, while the vast majority of the shelf had no trend in pCO_2, [H$^+$], pH, or Ω_{Ar}, the northern shelf did exhibit statistically significant basification trends for these variables. The Bering Sea shelf exhibited no trend for DIC (-0.3 ±2.3 μmol kg^{-1} decade^{-1}) but did display a clear sDIC decrease (-4.6 ±2.3 μmol kg^{-1} decade^{-1}). SSS slightly increased (0.054 psu decade^{-1}), as did TA (2.7 μmol kg^{-1} decade^{-1}), but sTA had no statistical trend (0.03 ±1.19 μmol kg^{-1} decade^{-1}). The Bering Sea shelf also had the highest warming rate (0.24°C decade^{-1}) across all three zones.

5.4.3 Southern PAR Trends

The Southern PAR exhibited average acidification rates of 14 μatm decade^{-1} for pCO_2, 0.281 nmol kg^{-1} decade^{-1} for [H^+], -0.015 pH units decade^{-1}, and -0.040 Ω_{Ar} units decade^{-1}, which agrees with the established literature (Table 1). Rising trends in DIC (4.40 μmol kg^{-1} decade^{-1}) and sDIC (4.69 μmol kg^{-1} decade^{-1}) were indistinguishable within trend uncertainties of ±1.1 μmol kg^{-1} decade^{-1}, indicating freshwater addition or removal was minimal. This is highlighted by overall statistically insignificant trends in SSS (0.01 ±0.01 psu decade^{-1}), TA (-0.54 ±0.51 μmol kg^{-1} decade^{-1}), and sTA (-0.07 ±0.48 μmol kg^{-1} decade^{-1}).

5.5 Ocean Acidification Drivers

The results of the driver decomposition, averaged into the three zones, are presented in Figure 8 and listed in Table 5. In all cases, changes in sensitivity and the mass effect had near-equal magnitudes and opposite directions, meaning that changes in the drivers themselves were solely responsible for long-term trends in Ω_{Ar} and [H^+]. As such, Table 5 and our results and discussion will focus solely on the ΔDriver results. Detailed values for changes in sensitivity and mass effect are provided in Appendix D.

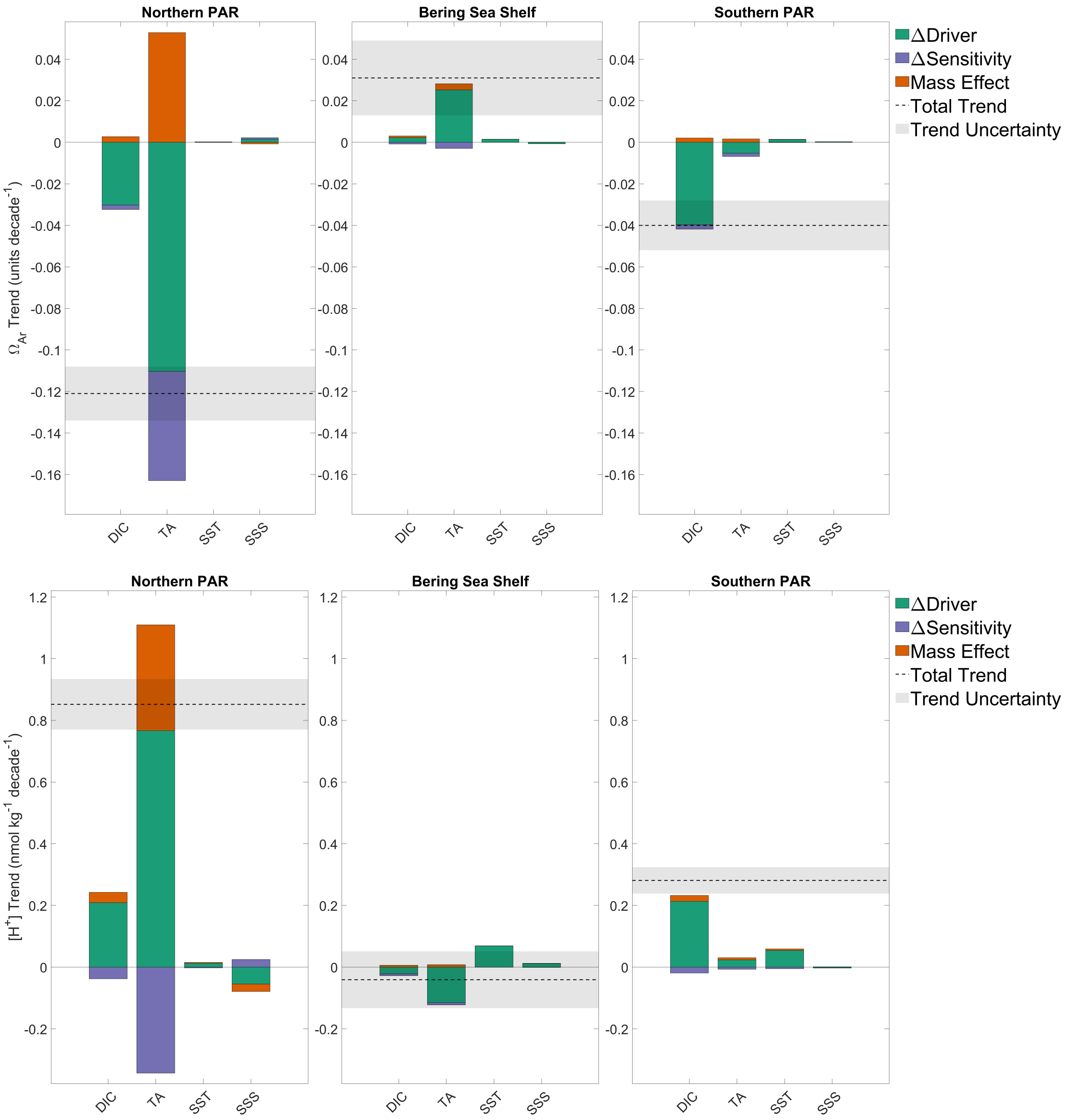

Figure 8: This top figure presents the area-weighted driver decomposition results for each zone, calculated using Equation 14. The four drivers (DIC, TA, SST, and SSS) are further decomposed based on change in driver, change in sensitivity of Ω_{Ar} to that driver, and the mass effect. The sum of all drivers approximately equals the total trend, shown as the dashed line. The bottom figure is the same as the top, but for [H$^+$] and Equation 15.

Table 5: Results of driver decomposition for Ω_{Ar} and [H$^+$]. Only the results for ΔDriver are shown, as ΔSensitivity and Mass Effect were equal and opposite in all cases, meaning ΔDriver values fully account for observed trends in Ω_{Ar} and [H$^+$]. Each value represents the area-weighted average value and uncertainty for the corresponding zone. The sum of all 4 values (*i.e.*, ΔDriver for DIC, TA, SSS, and SST) equals the total trend of Ω_{Ar} and [H$^+$] per Equations 14 and 15. The total trends in Table 4 may differ slightly from the summed decomposed drivers as a result of averaging across grid cells. Decomposed drivers are in Ω_{Ar} units decade^{-1} for Ω_{Ar} and nmol H$^+$ kg^{-1} decade^{-1} for [H$^+$].

	Northern PAR	**Bering Sea shelf**	**Southern PAR**
		ΔDriver (Ω_{Ar})	
DIC	-0.030±0.018	0.002±0.020	-0.040±0.010
TA	-0.110±0.015	0.025±0.012	-0.005±0.005
SSS	0.001±0.000	-0.001±0.000	0.000±0.000
SST	0.000±0.000	0.001±0.000	0.001±0.000
		ΔDriver ([H$^+$])	
DIC	0.209±0.130	-0.022±0.110	0.213±0.052
TA	0.767±0.102	-0.115±0.060	0.023±0.025
SSS	-0.055±0.001	0.011±0.000	-0.003±0.000
SST	0.012±0.000	0.069±0.001	0.054±0.000

5.5.1 Northern PAR Drivers

Table 5 and Figure 8 indicate that the primary cause of surface acidification in the Northern PAR is decreasing TA. $\Delta\text{Driver}_{\text{TA}}$-$\Omega_{Ar}$ had a value of -0.11 units decade^{-1}, accounting for approximately 91% of the total Ω_{Ar} trend of -0.12 units decade^{-1}. Increasing DIC further drove acidification, with a $\Delta\text{Driver}_{\text{DIC}}$-$\Omega_{Ar}$ value of -0.03 units decade^{-1}. The direct effect of declining SSS acted to mitigate acidification trends ($\Delta\text{Driver}_{\text{SSS}}$-$\Omega_{Ar}$ = 0.001 units decade^{-1}), though its effect was orders of magnitude less than TA and DIC. Rising SST had no effect on Ω_{Ar} trends, evidenced by the $\Delta\text{Driver}_{\text{SST}}$-$\Omega_{Ar}$ value of 0.000 units decade^{-1}.

Driver decomposition of [H$^+$] yields similar results. Negative trends in TA were the major factor driving acidification ($\Delta\text{Driver}_{\text{TA}}$-[H$^+$] = 0.767 nmol kg^{-1} decade^{-1}) and accounted for approximately 90% of the total [H$^+$] trend of 0.851

nmol kg^{-1} decade^{-1}. Rising DIC was again the second largest factor (ΔDriver$_{\mathrm{DIC}}$-[H$^+$] = 0.209 nmol kg^{-1} decade^{-1}). Unlike Ω_{Ar}, SSS and SST had a more notable effect on [H$^+$] trends. The direct effect of freshening slightly mitigated acidification (ΔDriver$_{\mathrm{SSS}}$-[H$^+$] = -0.055 nmol kg^{-1} decade^{-1}) while rising temperatures drove it, albeit at insignificant levels (ΔDriver$_{\mathrm{SST}}$-[H$^+$] = -0.003 nmol kg^{-1} decade^{-1})

5.5.2 Bering Sea Shelf Drivers

Similar to the Northern PAR, changes in TA were the primary driver for observed trends in Ω_{Ar} on the Bering Sea shelf. Unlike the Northern PAR, the Bering Sea shelf experienced an overall increase in TA, driving basification (ΔDriver$_{\mathrm{TA}}$-Ω_{Ar} = 0.025 units decade^{-1}). DIC was again the second strongest driver (ΔDriver$_{\mathrm{DIC}}$-Ω_{Ar} = 0.002 units decade^{-1}), the major difference being DIC decreased on the Bering Sea shelf. While the effect of changes in DIC on Ω_{Ar} are low compared to TA, the fact that DIC is not driving acidification is noteworthy in itself. The direct effects of trends in SSS (ΔDriver$_{\mathrm{SSS}}$-Ω_{Ar} = -0.001 units decade^{-1}) and SST (ΔDriver$_{\mathrm{SST}}$-Ω_{Ar} = 0.001 units decade^{-1}) on Ω_{Ar} trends were relatively minor and cancelled each other out.

For [H$^+$], positive trends in TA were the primary factor and also drove basification (ΔDriver$_{\mathrm{TA}}$-[H$^+$] = -0.115 nmol kg^{-1} decade^{-1}). However, unlike Ω_{Ar}, warming had the second-largest impact on [H$^+$] trends and acted to increase [H$^+$] (ΔDriver$_{\mathrm{SST}}$-[H$^+$] = 0.069 nmol kg^{-1} decade^{-1}). Decreasing DIC bolstered the basification driven by increased TA (ΔDriver$_{\mathrm{DIC}}$-[H$^+$] = -0.022 nmol kg^{-1} decade^{-1}), whereas the direct effects of salinity worked in tandem with SST to drive acidification (ΔDriver$_{\mathrm{SSS}}$-[H$^+$] = 0.011 nmol kg^{-1} decade^{-1}). The overall result of no [H$^+$] trend for the Bering Sea shelf arises from the combined effects of TA and DIC trends driving a decrease in [H$^+$], while changes in SST and SSS act to increase [H$^+$].

5.5.3 Southern PAR Drivers

The drivers of ocean acidification in the Southern PAR closely match that of the global, ice-free ocean. The specific values for all 12 driver components for Ω_{Ar} and [H$^+$] almost exactly match what Ma et al. (2023) found for the same region. The primary driver of acidification for Ω_{Ar} was increased DIC (ΔDriver$_{\mathrm{DIC}}$-Ω_{Ar} = -0.040 units decade^{-1}). TA had a relatively minor effect (ΔDriver$_{\mathrm{TA}}$-Ω_{Ar} = -0.005 units decade^{-1}), while trends in SSS (ΔDriver$_{\mathrm{SSS}}$-Ω_{Ar} = 0.000 units decade^{-1}) and SST (ΔDriver$_{\mathrm{SST}}$-Ω_{Ar} = 0.001 units decade^{-1}) had no effect on the overall trend.

DIC was also the primary factor driving acidification for [H$^+$] trends (ΔDriver$_{\mathrm{DIC}}$-[H$^+$] = 0.213 nmol kg^{-1} decade^{-1}). Similar to the Bering Sea shelf, rising temperatures had a larger effect on [H$^+$] trends compared to Ω_{Ar} (ΔDriver$_{\mathrm{SST}}$-[H$^+$] = 0.054 nmol kg^{-1} decade^{-1}) and also drove acidification. TA contributed an order of magnitude less than rising DIC (ΔDriver$_{\mathrm{TA}}$-[H$^+$] = 0.023 nmol kg^{-1} decade^{-1}) and the direct effects of SSS were inconsequential (ΔDriver$_{\mathrm{SSS}}$-[H$^+$] = -0.003 nmol kg^{-1} decade^{-1}).

6. DISCUSSION

6.1 Processes Driving TA Uncertainty

The spatial distribution of TA prediction error, as shown in Figure 4a, can shed light on regions with more complex biogeochemical processes. While a strong correlation exists between TA and SSS, certain processes can disrupt this relationship as detailed in Section 4.5. For instance, the formation and dissolution of calcium carbonate ($CaCO_3$) impacts TA without affecting SSS. Areas undergoing $CaCO_3$ dissolution would exhibit a rise in TA not mirrored in SSS measurements, leading to a higher prediction error. This increase in error, while highlighting a limitation in the TA prediction method's ability to accommodate salinity-independent processes, also signals underlying changes at these locations, providing valuable clues for further analysis.

Regions exhibiting the highest TA prediction errors correspond to areas where rivers drain into the sea, such as the Beaufort Sea near the Mackenzie River discharge, the East Siberian Sea at the Kolyma River outlet, and the northern Gulf of Alaska which is influenced by the Susitna and Copper Rivers. This pattern suggests that riverine inputs significantly affect the accuracy of our TA predictions by introducing variability not accounted for by SSS and SST alone. It also supports the notion that some Arctic rivers are undergoing significant changes in chemical composition (*e.g.* TA, nutrient concentration, dissolved organic carbon) as a result of climate change and anthropogenic activities and noted in prior work (Drake et al., 2018; Tank et al., 2023).

Shifts in plankton species composition, particularly changes involving coccolithophores - a group of highly-productive marine calcifiers - represents another salinity-independent factor affecting TA prediction accuracy. Coccolithophores significantly influence carbonate system dynamics. For instance, while primary productivity decreases DIC and marginally increases TA, $CaCO_3$ formation, characteristic of coccolithophores, leads to a reduction in TA (due to the removal of Ca^{2+} ions) and Ω_{Ar} (by eliminating CO_3^{2-} ions), as illustrated in the following reaction. This reaction also raises CO_2 levels, thereby lowering pH:

$$2HCO_3^- + Ca^{2+} \rightleftharpoons CO_2 + CaCO_3 + H_2O \tag{17}$$

Consequently, changes such as the poleward movement of Atlantic-sourced coccolithophores into the Arctic (Ardyna and Arrigo, 2020) can substantially alter local carbonate system dynamics, highlighting the complex interplay between biological activity and ocean chemistry. These processes underscore how regions of with high TA prediction residuals may simultaneously indicate regions that warrant further investigation.

6.2 Northern PAR

Our results indicate that surface acidification rates in the Northern PAR far exceed the global average primarily due to declining TA. This is a departure from the global, ice-free ocean where DIC drives acidification by an order of magnitude more than TA, SSS, or SST (*i.e.*, $\Delta \text{Driver}_{\text{DIC}} >> \Delta \text{Driver}_{\text{TA, SSS, SST}}$) (Ma et al., 2023). This negative trend in TA is likely due to sea ice decline as evidenced by Figure 9 and reported in prior, localized studies (Zhang et al., 2020b; Qi et al., 2022). Figures 9 (a)-(c) compare decadal trends (1993-2021) in sea ice thickness, SSS, and TA for the Northern PAR calculated using the seasonal Theil-Sen estimator. The center of the Arctic Ocean subregion exhibits strong negative trends in sea ice thickness (-0.8 m decade^{-1}), SSS (-1.0 psu decade^{-1}), and TA (-56.5 μmol kg^{-1} decade^{-1}), coinciding with the highest observed acidification rates in the PAR (Figure 7). Positive Pearson correlation coefficient (r) values across the Northern PAR between time series of sea ice thickness and SSS

(Figure 9(d)), and sea ice thickness and TA (Figure 9(e)), confirm the positive relationship between ice thickness, SSS, and TA. Areas with the most pronounced declines in ice thickness, SSS, and TA exhibit r values between 0.6 and 0.7 (where r=0 signifies no correlation and r=1 indicates perfect correlation), demonstrating a strong correlation between ice thickness and SSS and ice thickness and TA. This evidence supports the notion that the reduction in TA, and therefore the high rates of surface acidification, were primarily driven primarily by sea ice decline.

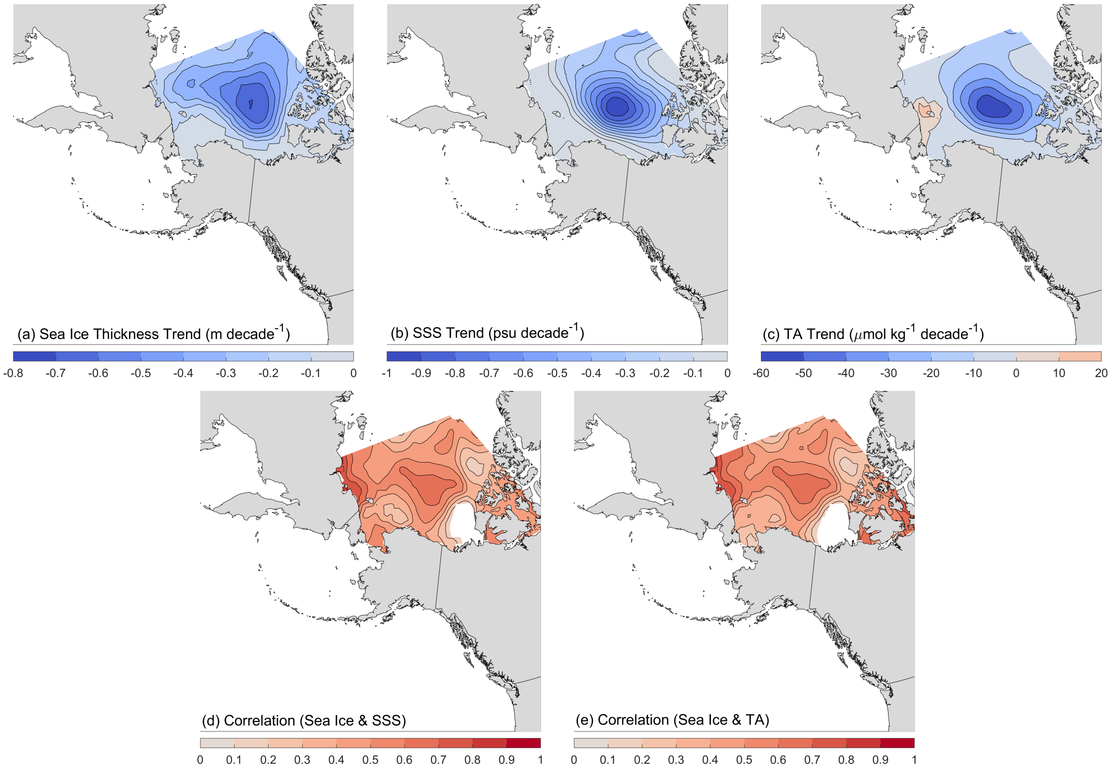

Figure 9: Decadal trends in (a) sea ice thickness, (b) SSS, and (c) TA for the Northern PAR from 1993-2021 determined using the seasonal Theil-Sen estimator. Locations with the highest rates of sea ice decline correspond to locations with strong negative SSS and TA trends. The Pearson correlation coefficient (r) between time series of ice thickness and SSS (d) and ice thickness and TA (e) statistically verify this observation. Only cells with $p < 0.05$ are plotted. The center of the Arctic subregion, which shows the highest rates of decline for sea ice, SSS, and TA, have r values between 0.6-0.7, indicating strong correlation.

Sea ice decline drives ocean acidification through dilution and enhanced CO_2 uptake. The mechanisms by which this occurs are heavily dependent on sea ice characteristics and can be broken into three distinct phases as shown in Figure 10. Figure 10 compares time series of sea ice thickness, SSS, surface pCO_2, and air-sea carbon flux (negative being into the water) from 1993-2021 in the Beaufort Gyre (75°N, 215°E). Phase I (1993-1998) is characterized by year-round multi-year ice cover. Sea ice thickness declined (-0.14 m yr^{-1}), driving dilution as indicated by the negative SSS trend (-0.4 psu yr^{-1}). Qi et al. (2022) found that dilution-driven reductions in TA and DIC from sea ice melt lower pCO_2, explaining the negative pCO_2 trend (-7.8 μatm yr^{-1}). Persistent ice cover prevented significant air-sea carbon flux, resulting in consistent near-zero flux values during Phase I. This dilution process primed surface waters underlying the ice for rapid acidification by decreasing both TA, lowering its resistance to acidification, and pCO_2, strengthening the pCO_2 gradient between underlying seawater and rising atmospheric CO_2 concentrations.

Phase II (1998-2013) marks the transition from a regime dominated by thick, multi-year ice with persistent coverage to one where thinner, seasonal first-year ice predominates, with September 1998 recording a historic low in sea ice extent that signaled the sea ice transition (Hutchings and Rigor, 2012; Zhang et al., 2020a). The remaining multi-year ice continued to melt, indicated by the ice thickness rate of -0.11 m yr^{-1}, driving further dilution as seen in the SSS trend of -0.3 psu yr^{-1}. Dilution-induced low pCO_2 values facilitated rapid pCO_2 uptake due to the strong air-sea pCO_2 gradient, reversing the negative pCO_2 trend of Phase I to a positive trend of 9.6 μatm $year^{-1}$ in Phase II. This is primarily because atmospheric CO_2 could now flux into surface waters due to the exposed air-sea interface, as indicated by the large negative September spikes in air-sea flux in Phase II that were not

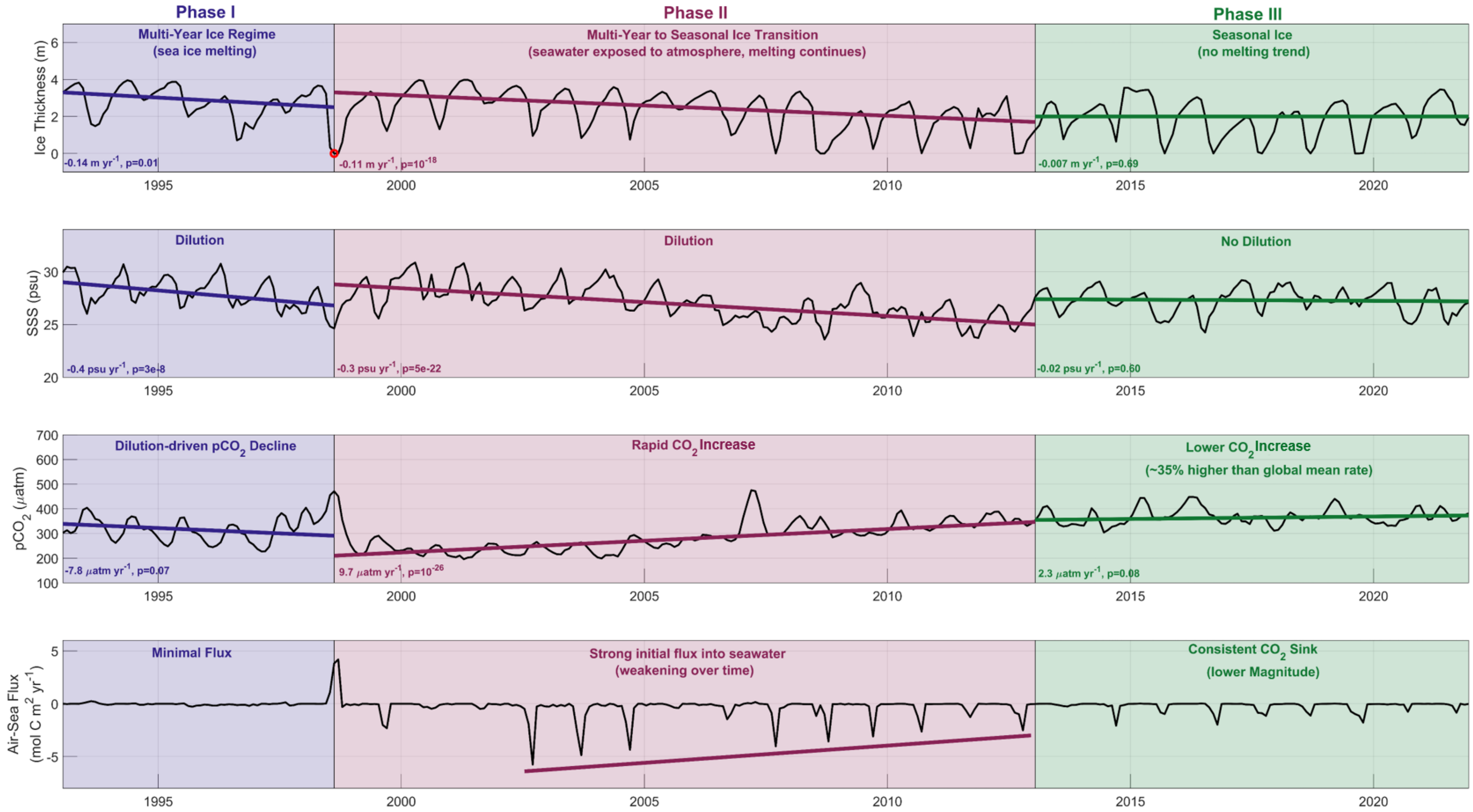

Figure 10: Time series of ice thickness, SSS, surface pCO$_2$, and air-sea carbon flux in the Beaufort Gyre (75°N, 215°E) from 1993-2021. This location corresponds to the highest observed acidification rates of the PAR. The time series is broken into three phases as described in Section 6.2. Phase I is characterized by thinning ice, which lowers SSS, TA, and pCO$_2$ via dilution. Persistent ice cover prevents air-sea flux, enabling a negative pCO$_2$ trend. Phase II marks when this location is predominated by seasonal sea ice and air-sea flux can rapidly increase pCO$_2$ levels. Dilution stops by Phase III and the air-sea pCO$_2$ gradient is smaller, reducing CO$_2$ uptake.

present during Phase I. This swift uptake, alongside the dilution-driven reduction in TA during Phases I and II, primarily drove the rapid acidification observed in the Beaufort Gyre. As the air-sea pCO_2 gradient diminished, so too did the seasonal carbon flux into the sea surface and the rate of pCO_2 uptake, signaling the shift to Phase III.

Phase III (2013-2021) is characterized by a stabilization of sea ice thickness and a lack of dilution, as evidenced by p-values for ice thickness and SSS trends of 0.69 and 0.60, respectively. Surface pCO_2 levels continued to climb at a rate of 2.3 μatm yr^{-1}, a pace four times slower than in Phase II and about 35% faster than the global average increase of 1.7 μatm yr^{-1}. Surface waters remained a consistent carbon sink each September, albeit at considerably reduced rates (-2.1 to 0.7 mol C m^2 yr^{-1}) compared to Phase II. Although we identified January 2013 as the boundary between Phase II and III, the actual transition likely represents a gradual, less distinct shift than the clear, stepwise shift from Phase I to II.

The decadal carbonate system trends summarized in Table 4 reflect an average across the entire time series and, therefore, might not fully capture the nuanced, shorter-scale processes specific to ice-dominated regions, as depicted in Figure 10. For instance, the overall 1993-2021 pCO_2 trend in the Beaufort Gyre was 65 μatm decade^{-1}, which is markedly different from the distinct trends of -78 μatm decade^{-1} in Phase I, 97 μatm decade^{-1} in Phase II, and 23 μatm decade^{-1} in Phase III. Nonetheless, averaging the rates from each phase according to their respective durations yields an overall rate of approximately 61 μatm per decade, closely aligning with the comprehensive trend of 65 μatm per decade.

These long-term averages, however, still justify that sea ice melt drove acidification rates. Recall that sTA and sDIC are the changes in TA and DIC, respectively, after the effects of freshwater are removed. The large differences between

TA and sTA (TA-sTA = -12.5 μmol kg^{-1} decade^{-1}), and DIC and sDIC (DIC-sDIC = -12.2 μmol kg^{-1} decade^{-1}), rates should therefore be mostly attributable to declining SSS. Having established the relationship between TA and SSS, and DIC and SSS, for surface Arctic waters (Figure 11), multiplying the TA-SSS slope (56.5 μmol kg^{-1} psu^{-1}), and DIC-SSS slope (47.5 μmol kg^{-1} psu^{-1}) by the SSS trend (-0.211 psu decade^{-1}) should equal the difference between TA and sTA, and DIC and sDIC. Multiplying the TA-SSS slope by the SSS trend equals -11.9 μmol kg^{-1}, which almost completely accounts for the 12.5 μmol kg^{-1} decade^{-1} difference between TA and sTA rates. Likewise, multiplying the DIC-SSS slope by the SSS trend equals -10.0 μmol kg^{-1} decade^{-1}, signaling that 83% of the difference between DIC and sDIC rates were due to freshening. The remaining difference could be due spatial variability in DIC-SSS slopes or a drift in DIC-SSS slopes as DIC increases due to anthropogenic CO_2 uptake, neither of which are accounted for in this first-order approximation. Having already established that negative SSS trends in this region are strongly correlated to declining sea ice thickness, this provides further support that the changes in TA and DIC responsible for the high acidification rates were linked to sea ice decline.

Our findings reveal that significant sea ice melt, coupled with increasing atmospheric CO_2 levels, led to rapid surface acidification in the Northern PAR, especially in zones undergoing shifts in sea ice dynamics. This observation has two primary implications. First, the intense acidification rates observed might be a temporary condition in regions transitioning from dense, year-round ice to seasonal coverage, as depicted in Figure 10. Zhang et al. (2020) observed this in the Beaufort Sea, noting a decline in surface Ω_{Ar} by 0.5 units decade^{-1} from 1997-2007 followed by no Ω_{Ar} trend from 2007-2016. The second implication is that higher latitudes, currently under year-round ice cover, might undergo rapid acidification

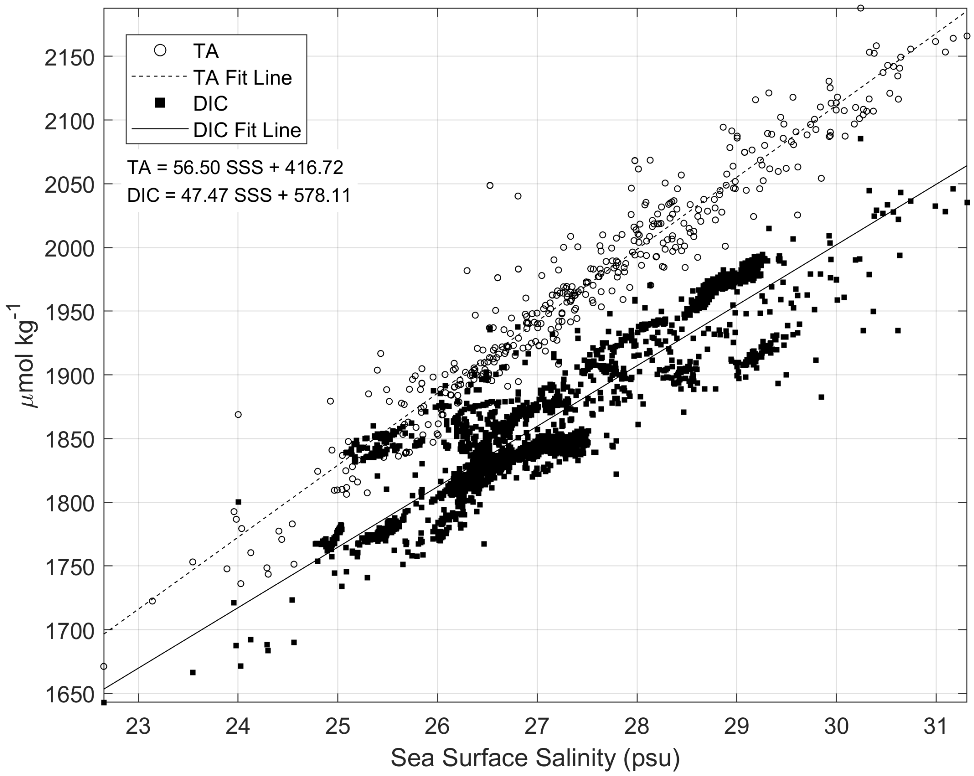

Figure 11: This plot features discrete measurements of TA (n=415) TA and DIC (n=3,356) from the upper 5 meters in the Arctic subregion. Note that while there is a clear linear relationship between TA and SSS, and DIC and SSS, the TA slope is 9 μmol kg^{-1} psu^{-1} higher than the DIC slope. This implies that decreasing SSS, such as due to sea ice melt, will decrease TA faster than DIC.

akin to Phase II of Figure 10 if their ice thins sufficiently to expose the surface waters to the atmosphere. However, the acidification rate would likely decline over time as the air-sea CO_2 gradient weakens as observed in Phase III.

6.3 Bering Sea Shelf

Our results indicate that basificiation (*i.e.*, increasing Ω_{Ar} and decreasing $[H^+]$) occurred on the Bering Sea shelf from 1993-2021. This challenges the prevailing literature that identifies the Bering Sea shelf as an acidification hotspot, with studies listed in Table 1 showing OA rates at or exceeding global levels.

Barring some coastal areas, our methodology exhibited low error and bias when predicting carbonate system variables across most of the Bering Sea shelf, suggesting our approach is well-equipped to detect significant trends as observed in the Northern and Southern PAR. Considering the disagreement between our Bering Sea shelf trends and the established literature, we also applied the bootstrap Theil-Sen estimator trend methodology to the OceanSODA-ETHZ and CMEMS-LSCE carbonate system datasets. This approach allowed us to compare trends across datasets with a uniform methodology, underscoring that disagreements are a result of the datasets rather than the methodology. Trends in pCO_2, pH, and Ω_{Ar} derived from OceanSODA-ETHZ and CMEMS-LSCE are presented in Figure 12.

Comparing trend results across datasets reveals a spectrum of predicted trends: our study indicates basification, OceanSODA points to acidification in line with global averages, and CMEMS datasets fall in between. OceanSODA-derived trends resulted in a significant pCO_2 increase of 17 μatm decade^{-1} and a pH rate of -0.019 units decade^{-1} . This aligns with the findings of Ma et al. (2023), who found similar rates in the Bering Sea and subarctic Pacific using OceanSODA. The CMEMS-LSCE datasets, meanwhile, showed more moderate changes: pCO_2 increases of 9-11 μatm decade^{-1} — half the rate of OceanSODA — and pH trends of -0.009 to -0.012 units decade^{-1}, closely aligning with our observed trend of 0.003 pH units decade^{-1} within trend uncertainties.

Significant discrepancies were most notable in Ω_{Ar} rates: our analysis found an increase of 0.031 units per decade, starkly contrasting OceanSODA's -0.042 units decade^{-1}. CMEMSr100 showed no statistically significant Ω_{Ar} trend, while CMEMSr25 indicated a slight negative trend (-0.013 ± 0.010 units decade^{-1}) with high relative uncertainty (76%). These differences highlight the varying acidification signals between datasets, with OceanSODA suggesting strong acidification

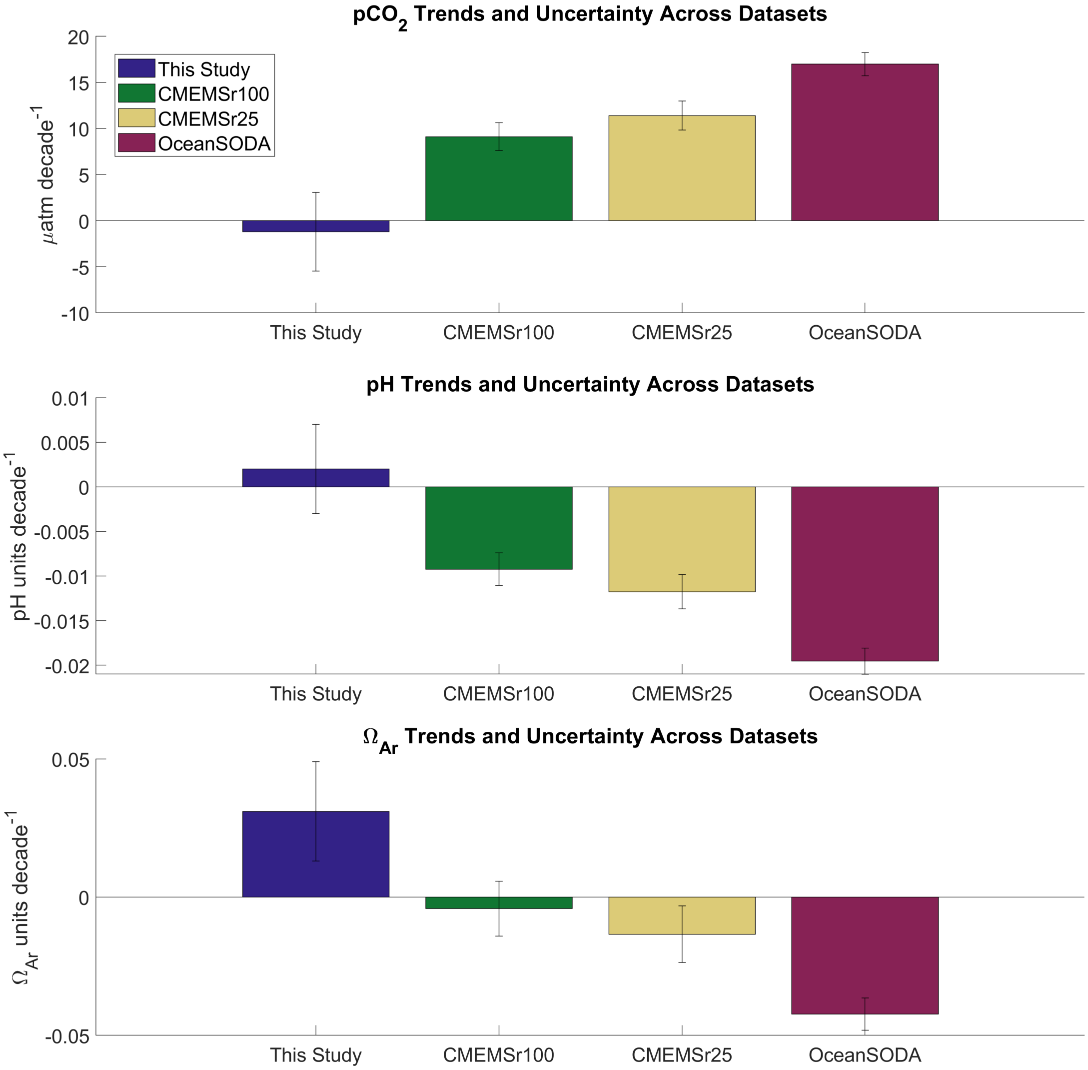

Figure 12: The bootstrapped seasonal Theil-Sen estimator was used to determine area-weighted average trends and trend uncertainties for pCO_2, pH, and Ω_{Ar} from 1993-2021 on the Bering Sea shelf. The trend methodology was applied to the CMEMSr100, CMEMSr25, and OceanSODA-ETHZ carbonate system datasets in order to compare the trends of this study using a consistent methodology.

and CMEMS indicating milder trends than OceanSODA but more pronounced than ours. The variance in trends between these datasets may be because MPI-SOM-FFN (the pCO_2 data used in this study), CMEMS, and OceanSODA are all neural networks trained to predict carbonate system parameters on a global scale, and as such may be limited in specific locales such as the Bering Sea shelf.

Supporting our findings, Zhang et al. (2023) utilized a Gaussian process regression (a non-neural network approach) to model surface pCO_2 specifically for the Bering Sea shelf. Their results revealed no significant surface pCO_2 trend on the shelf from 2003-2019. This concurs with our observations, suggesting our basification trend is consistent with alternative analytical approaches.

Similar to observations in the Northern PAR, changes in Ω_{Ar} and $[H^+]$ on the Bering Sea shelf were primarily influenced by decadal trends in TA, as depicted in Figure 8. However, in contrast to the Northern PAR, the Bering Sea shelf saw an increase in TA attributed to rising SSS. The Kendall trend test results (Figure 6) further clarify this dynamic. SSS, and therefore TA, increased on the western shelf and exhibited no trend on the eastern shelf. The salinity increase on the western half of the Bering Sea shelf raised buffer capacity because TA increases with SSS faster than DIC, as shown in Figure 11. Given that DIC typically rises with SSS, and anthropogenic CO_2 also elevates DIC, we might expect DIC to increase. However, our results show a decrease in both DIC and sDIC, suggesting that another process is removing DIC from the surface quicker than anthropogenic CO_2 uptake and increased DIC due to SSS can raise surface DIC levels.

We propose that increased surface primary productivity, which extracts inorganic carbon from surface waters and exports it to depth through the biological pump, is this factor. As outlined in Section 3, the Bering Sea shelf experiences spring and fall phytoplankton blooms due to nutrient-rich Anadyr water from the western shelf and Alaskan Coastal water from the eastern shelf mixing on the northern shelf. This dynamic supports the observation that rising primary productivity accounts for the basification trends observed on the northern shelf but not on the southern shelf. Notably, the emergence of fall phytoplankton blooms, tied to delayed sea ice formation and an extended growing season, suggests that primary productivity may have risen in tandem with decreasing sea ice extent. This hypothesis is supported by observed positive decadal trends in surface Chlorophyll *a* (Oziel et al., 2022) and annual primary production (Brown and Arrigo, 2012), as well as a biologically-driven increased summer carbon sink (Wang et al., 2022) on the Bering Sea shelf over a similar timeframe, pointing to increased primary productivity. This increase in primary productivity is likely responsible for the observed declines in DIC on the Bering Sea shelf, thereby contributing to the basification trends detected.

As described in Section 5.5, the direct effects of SSS and SST trends minimally impacted the overall Ω_{Ar} trend. However, the direct effects of SSS and SST had a notable effect on $[H^+]$ trends. While decreasing DIC and rising TA contributed to a reduction in $[H^+]$, increased SSS and SST on the Bering Sea shelf worked to elevate $[H^+]$, effectively neutralizing the overall trend. This significant influence of SSS and SST on $[H^+]$, as opposed to their limited effect on Ω_{Ar}, explains the statistically stronger and spatially extensive basification trends for Ω_{Ar} in comparison to less pronounced $[H^+]$ trends for the Bering Sea shelf.

Our findings suggest that the Bering Sea shelf did not experience surface ocean acidification from 1993 to 2021; instead, surface waters became less acidic in some portions of the shelf, and remained stable in others, due to a decline in DIC, likely due to enhanced primary production, and increased TA. The observed surface basification might account for the elevated acidification rates detected in bottom waters of the Bering Sea shelf (Mathis et al., 2014; Pilcher et al., 2022), as organic carbon from the surface undergoes remineralization at depth, increasing pCO_2 and promoting acidification. Although our findings diverge from the established literature for this region, surface basification does occur in some coastal waters, where physical and biogeochemical processes are more complex than in the open ocean. Factors such as rising river alkalinity concentrations (Kaushal et al., 2013), especially from Arctic rivers (Drake et al., 2018; Tank et al., 2023), and increasing riverine nutrient levels (Smith, 2003) may buffer coastal carbonate systems and enhance primary production, respectively. Decadal basification trends observed in areas such as Chesapeake Bay (Shen et al., 2020), the Gulf of Mexico (Hu et al., 2015; Gomez et al., 2021), and coastal Netherlands (Provoost et al., 2010) indicate that elevated atmospheric CO_2 does not uniformly lead to acidification across all regions. This underscores the importance of conducting further, ideally observational, studies on acidification in the Bering Sea to clarify these trends, especially given the region's significant economic value as a fishery and the potential impacts of ocean acidification on marine organisms.

6.4 Southern PAR

The Southern PAR exhibited acidification rates approximately half the global surface average, primarily due to increased DIC. The slight difference between DIC and sDIC (0.3 μmol kg^{-1} per decade) indicates that freshwater dynamics had minimal impact. Therefore, the increase in DIC is likely attributable to anthropogenic CO_2 uptake as noted in previous work (Ma et al., 2023) and expected in an ice-free, open-ocean environment. However, the southern Alaska coast uniquely showed no trends in pCO_2, pH, or Ω_{Ar}, as depicted in Figure 6. This anomaly could stem from the considerable uncertainty in pCO_2 measurements along the entire southern Alaska coast and significant TA uncertainty in the northern Gulf of Alaska, hindering the bootstrap method's ability to identify significant trends. Additionally, the upwards trend observed for SSS, and consequently TA, along the southern Alaskan coastline might have buffered the carbonate system, similar to the Bering Sea shelf. Coastal Gulf of Alaska also experiences significant runoff from land-terminating glaciers with higher TA than DIC, offering another potential cause for positive TA trends (Pilcher et al., 2018). This buffering effect could further obscure any potential acidification signal, especially amid uncertainty in carbonate system predictions.

6.5 Caveats and Limitations

Our study's primary limitation stems from the very issue it seeks to overcome: significant spatial and temporal data gaps. Figure 2b highlights the scarcity of carbonate system observations during the boreal spring and winter, especially in sea-ice-affected zones, with most sampling occurring in the summer and fall. This scarcity complicates, and in some locations prevents, prediction validation for spring and winter months. The complex interplay between sea ice dynamics and the carbonate system, coupled with the importance of sea ice trends to our findings, underscores the critical gap presented by the absence of field samples in these seasons. Moreover, certain areas within the PAR, such as key regions along the Russian coast (western Bering Sea and East Siberian Sea) and the Canadian Archipelago, suffer from a chronic lack of data throughout the year.

While these data gaps challenge our capacity to refine and validate predictive models in some locale during certain seasons, they underscore the necessity of our efforts to reconstruct the carbonate system from the limited data that is available. Enhanced sampling efforts in the Arctic would gradually refine such predictions, sharpening our understanding of the region's evolving carbonate dynamics.

7. CONCLUSION

By harnessing open-source datasets across the PAR, we identified spatial relationships to predict surface TA from widely available datasets. In conjunction with the MPI-SOM-FFN surface pCO_2 dataset, it was possible to resolve the full surface carbonate system on a monthly basis from 1993-2021. Leveraging this dataset, we introduced a robust methodology for detecting and quantifying trends, marking the first effort to systematically quantify trends in surface carbonate system parameters across the PAR. This approach bridges spatial and temporal gaps in our understanding of trends outlined in Table 1. The Northern PAR lacks a publicly-available comprehensive carbonate system dataset, with existing resources such as CMEMS and OceanSODA offering limited coverage in ice-covered regions. Therefore, the surface carbonate system dataset compiled in this study, as well as the discrete bottle samples, are intended to facilitate subsequent research efforts.

Our findings reveal that the Northern PAR experienced rates of surface ocean acidification 2-4 times higher than the global average, primarily attributed to the dynamics between sea ice and the carbonate system in zones of multi-year ice recession. Conversely, the Bering Sea shelf – a critical conduit for Pacific waters into the Arctic Ocean – showed trends of basification, possibly due to enhanced primary productivity. This suggests that while the PAR in general is vulnerable to acidification, the highly productive ecosystem of the Bering Sea shelf acted to mitigate the effects of rising atmospheric CO_2, albeit with potential repercussions for acidification in deeper waters. In the Southern PAR, an ice-free, open-ocean regime, acidification proceeded at roughly half the global rate, largely driven by anthropogenic CO_2 absorption, underscoring varied responses within the PAR to external forcing.

Should atmospheric CO_2 continue to rise, surface waters of the PAR will likely continue to acidify. Continued anthropogenic warming poses a significant threat to the high-latitude areas of the Northern PAR, which are currently shielded from CO_2 invasion by annually persistent sea ice. A transition in these regions from a multi-year ice cover to a dominantly seasonal, first-year ice cover could trigger rapid acidification similar to that observed in the Beaufort Gyre within this study. Although rising primary productivity, potentially driven by sea ice changes, currently seems to mitigate surface acidification on the Bering Sea shelf, it is likely that this CO_2 export from the surface will be surpassed by the influx of atmospheric CO_2, unless there is a sustained increase in primary productivity. Therefore, the current basification observed on the Bering Sea shelf may be temporary, with future data potentially showing acidification. Likewise, the Southern PAR is expected to keep acidifying as atmospheric CO_2 levels rise.

Key areas for future investigation include detailed analyses of regions with high uncertainties in pCO_2 and TA to refine trend identification. Moreover, enhancing the methodologies for predicting pCO_2 and TA, especially by explicitly incorporating seasonality, could significantly improve the accuracy of trend predictions and reduce uncertainties. Refining TA and DIC drivers into specific processes such as net community production, calcification, and anthropogenic carbon uptake (Fassbender et al., 2016; Ma et al., 2023), would offer further insight into the drivers of long-term change in the carbonate system. The results pertaining to the Bering Sea shelf, which contrast with prevailing literature, highlight a need for future work focused on understanding the mechanisms driving changes in the carbonate system of this ecologically important region.

LIST OF REFERENCES

Alin, S. R., Feely, R. A., Dickson, A. G., Hernández-Ayón, J. M., Juranek, L. W., Ohman, M. D., and Goericke, R. (2012). Robust empirical relationships for estimating the carbonate system in the southern California Current System and application to CalCOFI hydrographic cruise data (2005–2011). *Journal of Geophysical Research: Oceans*, 117(C5).

AMAP (2013). AMAP assessment 2013: Arctic ocean acidification. Technical report, Arctic Monitoring and Assessment Programme (AMAP), Tromsø, Norway.

AMAP (2018). AMAP assessment 2018: Arctic ocean acidification. Technical report, Arctic Monitoring and Assessment Programme (AMAP), Tromsø, Norway.

Ardyna, M. and Arrigo, K. R. (2020). Phytoplankton dynamics in a changing Arctic Ocean. *Nature Climate Change*, 10(10):892–903.

Bakker, D. C. E., Pfeil, B., Landa, C. S., Metzl, N., O'Brien, K. M., Olsen, A., Smith, K., Cosca, C., Harasawa, S., Jones, S. D., Nakaoka, S., Nojiri, Y., Schuster, U., Steinhoff, T., Sweeney, C., Takahashi, T., Tilbrook, B., Wada, C., Wanninkhof, R., Alin, S. R., Balestrini, C. F., Barbero, L., Bates, N. R., Bianchi, A. A., Bonou, F., Boutin, J., Bozec, Y., Burger, E. F., Cai, W.-J., Castle, R. D., Chen, L., Chierici, M., Currie, K., Evans, W., Featherstone, C., Feely, R. A., Fransson, A., Goyet, C., Greenwood, N., Gregor, L., Hankin, S., Hardman-Mountford, N. J., Harlay, J., Hauck, J., Hoppema, M., Humphreys, M. P., Hunt, C. W., Huss, B., Ibánhez, J. S. P., Johannessen, T., Keeling, R., Kitidis, V., Körtzinger, A., Kozyr, A., Krasakopoulou, E., Kuwata, A., Landschützer, P., Lauvset, S. K., Lefèvre, N., Lo Monaco, C., Manke, A., Mathis, J. T., Merlivat, L., Millero, F. J., Monteiro, P. M. S., Munro, D. R., Murata, A., Newberger, T., Omar, A. M., Ono, T., Paterson, K., Pearce, D., Pierrot, D., Robbins, L. L., Saito, S., Salisbury, J., Schlitzer, R., Schneider, B., Schweitzer, R., Sieger, R., Skjelvan, I., Sullivan, K. F., Sutherland, S. C., Sutton, A. J., Tadokoro, K., Telszewski, M., Tuma, M., van Heuven, S. M. A. C., Vandemark, D., Ward, B., Watson, A. J., and Xu, S. (2016). A multi-decade record of high-quality fCO2 data in version 3 of the Surface Ocean CO2 Atlas (SOCAT). *Earth System Science Data*, 8(2):383–413.

Bates, N. R. (2006). Air-sea CO2 fluxes and the continental shelf pump of carbon in the Chukchi Sea adjacent to the Arctic Ocean. *Journal of Geophysical Research: Oceans*, 111(C10).

Brown, Z. W. and Arrigo, K. R. (2012). Contrasting trends in sea ice and primary production in the Bering Sea and Arctic Ocean. *ICES Journal of Marine Science*, 69(7):1180–1193.

Cai, W.-J., Chen, L., Chen, B., Gao, Z., Lee, S. H., Chen, J., Pierrot, D., Sullivan, K., Wang, Y., Hu, X., Huang, W.-J., Zhang, Y., Xu, S., Murata, A., Grebmeier, J. M., Jones, E. P., and Zhang, H. (2010). Decrease in the CO2 uptake capacity in an ice-free Arctic Ocean basin. *Science*, 329(5991):556–559.

Caldeira, K. and Wickett, M. E. (2003). Anthropogenic carbon and ocean pH. *Nature*, 425(6956):365–365.

Carstensen, J. and Duarte, C. M. (2019). Drivers of pH variability in coastal ecosystems. *Environmental Science & Technology*, 53(8):4020–4029.

Carter, B. R., Feely, R. A., Williams, N. L., Dickson, A. G., Fong, M. B., and Takeshita, Y. (2018). Updated methods for global locally interpolated estimation of alkalinity, pH, and nitrate. *Limnology and Oceanography: Methods*, 16(2):119–131.

Chapman, W. L. and Walsh, J. E. (1993). Recent variations of sea ice and air temperature in high latitudes. *Bulletin of the American Meteorological Society*, 74(1):33–48.

Chau, T.-T.-T., Gehlen, M., Metzl, N., and Chevallier, F. (2023). CMEMS-LSCE: A global 0.25-degree, monthly reconstruction of the surface ocean carbonate system. *Earth System Science Data Discussions*, 2023:1–52.

Chen, L. and Gao, Z. (2007). Spatial variability in the partial pressures of CO2 in the northern Bering and Chukchi seas. *Deep Sea Research Part II: Topical Studies in Oceanography*, 54(23-26):2619–2629.

Chierici, M. and Fransson, A. (2009). Calcium carbonate saturation in the surface water of the Arctic Ocean: undersaturation in freshwater influenced shelves. *Biogeosciences*, 6(11):2421–2431.

Cooley, S. R., Kite-Powell, H. L., and Doney, S. C. (2009). Ocean acidification's potential to alter global marine ecosystem services. *Oceanography*, 22(4):172–181.

DeGrandpre, M., Evans, W., Timmermans, M.-L., Krishfield, R., Williams, B., and Steele, M. (2020). Changes in the Arctic Ocean carbon cycle with diminishing ice cover. *Geophysical Research Letters*, 47(12):e2020GL088051.

Dickson, A. G. (1990). Standard potential of the reaction: AgCl(s) + 12H2(g) = Ag(s) + HCl(aq), and and the standard acidity constant of the ion HSO4 in synthetic sea water from 273.15 to 318.15 K. *The Journal of Chemical Thermodynamics*, 22(2):113–127.

Dickson, A. G. (2010). The carbon dioxide system in seawater: equilibrium chemistry and measurements. *Guide to best practices for ocean acidification research and data reporting*, 1:17–40.

Dodman, D., Hayward, B., Pelling, M., Castan Broto, V., Chow, W., Chu, E., Dawson, R., Khirfan, L., McPhearson, T., Prakash, A., Zheng, Y., and Ziervogel, G. (2022). Cities, settlements and key infrastructure. in: Climate change 2022: Impacts, adaptation, and vulnerability. contribution of working group ii to the sixth assessment report of the intergovernmental panel on climate change. pages 907–1040.

Doney, S. C., Fabry, V. J., Feely, R. A., and Kleypas, J. A. (2009). Ocean acidification: The other CO2 problem. *Annual Review of Marine Science*, 1(1):169–192. PMID: 21141034.

Drake, T. W., Tank, S. E., Zhulidov, A. V., Holmes, R. M., Gurtovaya, T., and Spencer, R. G. (2018). Increasing alkalinity export from large Russian Arctic rivers. *Environmental science & technology*, 52(15):8302–8308.

Duarte, C. M., Hendriks, I. E., Moore, T. S., Olsen, Y. S., Steckbauer, A., Ramajo, L., Carstensen, J., Trotter, J. A., and McCulloch, M. (2013). Is ocean acidification an open-ocean syndrome? understanding anthropogenic impacts on seawater pH. *Estuaries and Coasts*, 36:221–236.

Fabry, V. J., McClintock, J. B., Mathis, J. T., and Grebmeier, J. M. (2009). Ocean acidification at high latitudes: The bellwether. *Oceanography*, 22.

Fassbender, A. J., Sabine, C. L., and Cronin, M. F. (2016). Net community production and calcification from 7 years of NOAA Station Papa mooring measurements. *Global Biogeochemical Cycles*, 30(2):250–267.

Feely, R. A., Sabine, C. L., Lee, K., Berelson, W., Kleypas, J., Fabry, V. J., and Millero, F. J. (2004). Impact of anthropogenic CO2 on the CaCO3 system in the oceans. *Science*, 305(5682):362–366.

Friedland, K. D., Mouw, C. B., Asch, R. G., Ferreira, A. S. A., Henson, S., Hyde, K. J. W., Morse, R. E., Thomas, A. C., and Brady, D. C. (2018). Phenology and time series trends of the dominant seasonal phytoplankton bloom across global scales. *Global Ecology and Biogeography*, 27(5):551–569.

Friis, K., Körtzinger, A., and Wallace, D. W. R. (2003). The salinity normalization of marine inorganic carbon chemistry data. *Geophysical Research Letters*, 30(2).

García, H. E., Weathers, K., Paver, C. R., Smolyar, I., Boyer, T. P., Locarnini, R. A., Zweng, M. M., Mishonov, A. V., Baranova, O. K., Seidov, D., and Reagan, J. R. (2019). World ocean atlas 2018, volume 4: Dissolved inorganic nutrients (phosphate, nitrate and nitrate+nitrite, silicate). NOAA Atlas NESDIS 84.

Gomez, F. A., Wanninkhof, R., Barbero, L., and Lee, S.-K. (2021). Increasing river alkalinity slows ocean acidification in the northern Gulf of Mexico. *Geophysical Research Letters*, 48(24):e2021GL096521. e2021GL096521 2021GL096521.

Good, S. A., Martin, M. J., and Rayner, N. A. (2013). EN4: quality controlled ocean temperature and salinity profiles and monthly objective analyses with uncertainty estimates. *Journal of Geophysical Research: Oceans*, 118(12):6704–6716.

Grebmeier, J. M. (2012). Shifting patterns of life in the Pacific Arctic and Sub-Arctic seas. *Annual Review of Marine Science*, 4(1):63–78. PMID: 22457969.

Grebmeier, J. M., Cooper, L. W., Feder, H. M., and Sirenko, B. I. (2006). Ecosystem dynamics of the Pacific-influenced Northern Bering and Chukchi Seas in the Amerasian Arctic. *Progress in Oceanography*, 71(2):331–361. Structure and function of contemporary food webs on Arctic shelves: a pan-Arctic comparison.

Gregor, L. and Gruber, N. (2021). OceanSODA-ETHZ: a global gridded data set of the surface ocean carbonate system for seasonal to decadal studies of ocean acidification. *Earth System Science Data*, 13(2):777–808.

Gruber, N., Hauri, C., Lachkar, Z., Loher, D., Frölicher, T. L., and Plattner, G.-K. (2012). Rapid progression of ocean acidification in the California current system. *Science*, 337(6091):220–223.

Hirsch, R. M., Slack, J. R., and Smith, R. A. (1982). Techniques of trend analysis for monthly water quality data. *Water Resources Research*, 18(1):107–121.

Hu, X., Pollack, J. B., McCutcheon, M. R., Montagna, P. A., and Ouyang, Z. (2015). Long-term alkalinity decrease and acidification of estuaries in northwestern Gulf of Mexico. *Environmental science & technology*, 49(6):3401–3409.

Hutchings, J. K. and Rigor, I. G. (2012). Role of ice dynamics in anomalous ice conditions in the Beaufort Sea during 2006 and 2007. *Journal of Geophysical Research: Oceans*, 117(C8).

Hönisch, B., Ridgwell, A., Schmidt, D. N., Thomas, E., Gibbs, S. J., Sluijs, A., Zeebe, R., Kump, L., Martindale, R. C., Greene, S. E., Kiessling, W., Ries, J., Zachos, J. C., Royer, D. L., Barker, S., Marchitto, T. M., Moyer, R., Pelejero, C., Ziveri, P., Foster, G. L., and Williams, B. (2012). The geological record of ocean acidification. *Science*, 335(6072):1058–1063.

Iida, Y., Takatani, Y., Kojima, A., and Ishii, M. (2021). Global trends of ocean CO2 sink and ocean acidification: an observation-based reconstruction of surface ocean inorganic carbon variables. *Journal of Oceanography*, 77:323–358.

Jersild, A., Landschützer, P., Gruber, N., and Bakker, D. (2017). An observation-based global monthly gridded sea surface pCO2 and air-sea CO2 flux product from 1982 onward and its monthly climatology (NCEI Accession 0160558). Dataset Version 7.7, NOAA National Centers for Environmental Information.

Jiang, L.-Q., Carter, B. R., Feely, R. A., Lauvset, S. K., and Olsen, A. (2019). Surface ocean pH and buffer capacity: past, present and future. *Scientific reports*, 9(1):18624.

Kaushal, S. S., Likens, G. E., Jaworski, N. A., Pace, M. L., Sides, A. M., Seekell, D., Belt, K. T., Secor, D. H., and Wingate, R. L. (2010). Rising stream and river temperatures in the United States. *Frontiers in Ecology and the Environment*, 8(9):461–466.

Kaushal, S. S., Likens, G. E., Utz, R. M., Pace, M. L., Grese, M., and Yepsen, M. (2013). Increased river alkalinization in the eastern US. *Environmental science & technology*, 47(18):10302–10311.

Kwok, R. (2018). Arctic sea ice thickness, volume, and multiyear ice coverage: losses and coupled variability (1958–2018). *Environmental Research Letters*, 13(10):105005.

Landschützer, P., Gruber, N., Bakker, D. C., Stemmler, I., and Six, K. D. (2018). Strengthening seasonal marine CO2 variations due to increasing atmospheric CO2. *Nature Climate Change*, 8(2):146–150.

Landschützer, P., Gruber, N., Bakker, D. C. E., Schuster, U., Nakaoka, S., Payne, M. R., Sasse, T. P., and Zeng, J. (2013). A neural network-based estimate of the seasonal to inter-annual variability of the Atlantic Ocean carbon sink. *Biogeosciences*, 10(11):7793–7815.

Landschützer, P., Gruber, N., and Bakker, D. C. E. (2016). Decadal variations and trends of the global ocean carbon sink. *Global Biogeochemical Cycles*, 30(10):1396–1417.

Landschützer, P., Gruber, N., Bakker, D. C. E., and Schuster, U. (2014). Recent variability of the global ocean carbon sink. *Global Biogeochemical Cycles*, 28(9):927–949.

Lauvset, S. K., Gruber, N., Landschützer, P., Olsen, A., and Tjiputra, J. (2015). Trends and drivers in global surface ocean pH over the past 3 decades. *Biogeosciences*, 12(5):1285–1298.

Lauvset, S. K., Lange, N., Tanhua, T., Bittig, H. C., Olsen, A., Kozyr, A., Alin, S., Álvarez, M., Azetsu-Scott, K., Barbero, L., Becker, S., Brown, P. J., Carter, B. R., da Cunha, L. C., Feely, R. A., Hoppema, M., Humphreys, M. P., Ishii, M., Jeansson, E., Jiang, L.-Q., Jones, S. D., Lo Monaco, C., Murata, A., Müller, J. D., Pérez, F. F., Pfeil, B., Schirnick, C., Steinfeldt, R., Suzuki, T., Tilbrook, B., Ulfsbo, A., Velo, A., Woosley, R. J., and Key, R. M. (2022). GLODAPv2.2022: the latest version of the global interior ocean biogeochemical data product. *Earth System Science Data*, 14(12):5543–5572.

Le Chatelier, H. L. (1884). A general statement of the laws of chemical equilibrium. *Comptes rendus*, 99:786–789.

Lee, H., Calvin, K., Dasgupta, D., Krinner, G., Mukherji, A., Thorne, P., Trisos, C., Romero, J., Aldunce, P., Barrett, K., et al. (2023). Climate change 2023: Synthesis report. contribution of working groups i, ii and iii to the sixth assessment report of the intergovernmental panel on climate change. pages 35–115.

Lee, K., Tong, L. T., Millero, F. J., Sabine, C. L., Dickson, A. G., Goyet, C., Park, G.-H., Wanninkhof, R., Feely, R. A., and Key, R. M. (2006). Global relationships of total alkalinity with salinity and temperature in surface waters of the world's oceans. *Geophysical Research Letters*, 33(19).

Lehmann, C. M., Bowersox, V. C., and Larson, S. M. (2005). Spatial and temporal trends of precipitation chemistry in the United States, 1985–2002. *Environmental Pollution*, 135(3):347–361. The National Atmospheric Depostition PRogram (25th Anniversary) and Ammonia Workshop.

LeSage, J. P. (1999). The theory and practice of spatial econometrics. *University of Toledo. Toledo, Ohio*, 28(11):1–39.

Lewis, E. R. and Wallace, D. W. R. (1998). Program developed for CO2 system calculations.

Ma, D., Gregor, L., and Gruber, N. (2023). Four decades of trends and drivers of global surface ocean acidification. *Global Biogeochemical Cycles*, 37(7):e2023GB007765. e2023GB007765 2023GB007765.

Mathis, J. T., Cross, J. N., Evans, W., and Doney, S. C. (2015). Ocean acidification in the surface waters of the Pacific-Arctic boundary regions. *Oceanography.*

Mathis, J. T., Cross, J. N., Monacci, N., Feely, R. A., and Stabeno, P. (2014). Evidence of prolonged aragonite undersaturations in the bottom waters of the southern Bering Sea shelf from autonomous sensors. *Deep Sea Research Part II: Topical Studies in Oceanography*, 109:125–133.

Mathis, J. T., Pickart, R. S., Byrne, R. H., McNeil, C. L., Moore, G., Juranek, L. W., Liu, X., Ma, J., Easley, R. A., Elliot, M. M., et al. (2012). Storm-induced upwelling of high pCO2 waters onto the continental shelf of the western Arctic Ocean and implications for carbonate mineral saturation states. *Geophysical Research Letters*, 39(7).

Millero, F. J., Graham, T. B., Huang, F., Bustos-Serrano, H., and Pierrot, D. (2006). Dissociation constants of carbonic acid in seawater as a function of salinity and temperature. *Marine Chemistry*, 100(1):80–94.

Mol, J., Thomas, H., Myers, P. G., Hu, X., and Mucci, A. (2018). Inorganic carbon fluxes on the Mackenzie shelf of the Beaufort Sea. *Biogeosciences*, 15(4):1011–1027.

Mortenson, E., Steiner, N., Monahan, A. H., Hayashida, H., Sou, T., and Shao, A. (2020). Modeled impacts of sea ice exchange processes on Arctic Ocean carbon uptake and acidification (1980–2015). *Journal of Geophysical Research: Oceans*, 125(7):e2019JC015782. e2019JC015782 10.1029/2019JC015782.

Nguyen, H. M., Ouillon, S., and Vu, V. D. (2022). Sea level variation and trend analysis by comparing Mann Kendall test and innovative trend analysis in front of the Red River Delta, Vietnam (1961-2020). *Water*, 14(11).

Orr, J. C., Epitalon, J.-M., Dickson, A. G., and Gattuso, J.-P. (2018). Routine uncertainty propagation for the marine carbon dioxide system. *Marine Chemistry*, 207:84–107.

Orr, J. C., Fabry, V. J., Aumont, O., Bopp, L., Doney, S. C., Feely, R. A., Gnanadesikan, A., Gruber, N., Ishida, A., Joos, F., et al. (2005). Anthropogenic ocean acidification over the twenty-first century and its impact on calcifying organisms. *Nature*, 437(7059):681–686.

Ouyang, Z., Qi, D., Chen, L., Takahashi, T., Zhong, W., DeGrandpre, M. D., Chen, B., Gao, Z., Nishino, S., Murata, A., et al. (2020a). Sea-ice loss amplifies summertime decadal CO2 increase in the western Arctic Ocean. *Nature Climate Change*, 10(7):678–684.

Ouyang, Z., Qi, D., Chen, L., Takahashi, T., Zhong, W., DeGrandpre, M. D., Chen, B., Gao, Z., Nishino, S., Murata, A., et al. (2020b). Sea-ice loss amplifies summertime decadal CO2 increase in the western Arctic Ocean. *Nature Climate Change*, 10(7):678–684.

Ouyang, Z., Qi, D., Zhong, W., Chen, L., Gao, Z., Lin, H., Sun, H., Li, T., and Cai, W.-J. (2021). Summertime evolution of net community production and CO2 flux in the western Arctic Ocean. *Global Biogeochemical Cycles*, 35(3):e2020GB006651.

Oziel, L., Massicotte, P., Babin, M., and Devred, E. (2022). Decadal changes in Arctic Ocean chlorophyll a: Bridging ocean color observations from the 1980s to present time. *Remote Sensing of Environment*, 275:113020.

Pilcher, D., Cross, J., Hermann, A., Kearney, K., Cheng, W., and Mathis, J. (2022). Dynamically downscaled projections of ocean acidification for the

Bering Sea. *Deep Sea Research Part II: Topical Studies in Oceanography*, 198:105055.

Pilcher, D. J., Naiman, D. M., Cross, J. N., Hermann, A. J., Siedlecki, S. A., Gibson, G. A., and Mathis, J. T. (2019). Modeled effect of coastal biogeochemical processes, climate variability, and ocean acidification on aragonite saturation state in the Bering Sea. *Frontiers in Marine Science*, 5.

Pilcher, D. J., Siedlecki, S. A., Hermann, A. J., Coyle, K. O., Mathis, J. T., and Evans, W. (2018). Simulated impact of glacial runoff on CO2 uptake in the Gulf of Alaska. *Geophysical Research Letters*, 45(2):880–890.

Portner, H., Roberts, D., Masson-Delmotte, V., Zhai, P., Tignor, M., Poloczanska, E., Mintenbeck, K., Alegría, A., Nicolai, M., Okem, A., Petzold, J., Rama, B., and Weyer, N. M. (2019). IPCC special report on the ocean and cryosphere in a changing climate. page 755.

Provoost, P., Van Heuven, S., Soetaert, K., Laane, R., and Middelburg, J. (2010). Seasonal and long-term changes in pH in the Dutch coastal zone. *Biogeosciences*, 7(11):3869–3878.

Qi, D., Ouyang, Z., Chen, L., Wu, Y., Lei, R., Chen, B., Feely, R. A., Anderson, L. G., Zhong, W., Lin, H., Polukhin, A., Zhang, Y., Zhang, Y., Bi, H., Lin, X., Luo, Y., Zhuang, Y., He, J., Chen, J., and Cai, W.-J. (2022). Climate change drives rapid decadal acidification in the Arctic Ocean from 1994 to 2020. *Science*, 377(6614):1544–1550.

Reynolds, R. W., Rayner, N. A., Smith, T. M., Stokes, D. C., and Wang, W. (2002). An improved in situ and satellite SST analysis for climate. *Journal of Climate*, 15(13):1609 – 1625.

Robbins, L. L., Wynn, J. G., Lisle, J. T., Yates, K. K., Knorr, P. O., Byrne, R. H., Liu, X., Patsavas, M. C., Azetsu-Scott, K., and Takahashi, T. (2013). Baseline monitoring of the western Arctic Ocean estimates 20% of Canadian Basin surface waters are undersaturated with respect to aragonite. *PloS one*, 8(9):e73796.

Sabine, C. L., Feely, R. A., Gruber, N., Key, R. M., Lee, K., Bullister, J. L., Wanninkhof, R., Wong, C. S., Wallace, D. W. R., Tilbrook, B., Millero, F. J., Peng, T.-H., Kozyr, A., Ono, T., and Rios, A. F. (2004). The oceanic sink for anthropogenic CO2. *Science*, 305(5682):367–371.

Semiletov, I., Pipko, I., Gustafsson, Ö., Anderson, L. G., Sergienko, V., Pugach, S., Dudarev, O., Charkin, A., Gukov, A., Bröder, L., et al. (2016). Acidification of East Siberian Arctic shelf waters through addition of freshwater and terrestrial carbon. *Nature Geoscience*, 9(5):361–365.

Sen, P. K. (1968). Estimates of the regression coefficient based on Kendall's tau. *Journal of the American Statistical Association*, 63(324):1379–1389.

Shen, C., Testa, J. M., Li, M., and Cai, W.-J. (2020). Understanding anthropogenic impacts on pH and aragonite saturation state in Chesapeake Bay: Insights from a 30-year model study. *Journal of Geophysical Research: Biogeosciences*, 125(7):e2019JG005620. e2019JG005620 2019JG005620.

Smith, R. A., Hirsch, R. M., and Slack, J. R. (1982). *A study of trends in total phosphorus measurements at NASQAN stations*. US Government Printing Office.

Smith, V. H. (2003). Eutrophication of freshwater and coastal marine ecosystems a global problem. *Environmental Science and Pollution Research*, 10:126–139.

Spalding, M. D., Fox, H. E., Allen, G. R., Davidson, N., Ferdaña, Z. A., Finlayson, M., Halpern, B. S., Jorge, M. A., Lombana, A., Lourie, S. A., Martin, K. D., McManus, E., Molnar, J., Recchia, C. A., and Robertson, J. (2007). Marine Ecoregions of the World: A Bioregionalization of Coastal and Shelf Areas. *BioScience*, 57(7):573–583.

Taibi, H. and Haddad, M. (2019). Estimating trends of the Mediterranean Sea level changes from tide gauge and satellite altimetry data (1993-2015). *Journal of Oceanology and Limnology*, 37(4):1176–1185.

Takahashi, T., Olafsson, J., Goddard, J. G., Chipman, D. W., and Sutherland, S. C. (1993). Seasonal variation of CO2 and nutrients in the high-latitude surface oceans: A comparative study. *Global Biogeochemical Cycles*, 7(4):843–878.

Tank, S. E., McClelland, J. W., Spencer, R. G., Shiklomanov, A. I., Suslova, A., Moatar, F., Amon, R. M., Cooper, L. W., Elias, G., Gordeev, V. V., et al. (2023). Recent trends in the chemistry of major northern rivers signal widespread Arctic change. *Nature Geoscience*, 16(9):789–796.

Tassone, S., Besterman, A., Buelo, C., Walter, J., and Pace, M. (2021). Co-occurrence of aquatic heatwaves with atmospheric heatwaves, low dissolved oxygen, and low pH events in estuarine ecosystems. *Estuaries and Coasts*, 45.

Tassone, S. J., Besterman, A. F., Buelo, C. D., Ha, D. T., Walter, J. A., and Pace, M. L. (2023). Increasing heatwave frequency in streams and rivers of the United States. *Limnology and Oceanography Letters*, 8(2):295–304.

Timmermans, M.-L. and Toole, J. M. (2023). The Arctic Ocean's Beaufort Gyre. *Annual Review of Marine Science*, 15:223–248.

Tu, Z., Le, C., Bai, Y., Jiang, Z., Wu, Y., Ouyang, Z., Cai, W.-J., and Qi, D. (2021). Increase in CO2 uptake capacity in the Arctic Chukchi Sea during summer revealed by satellite-based estimation. *Geophysical Research Letters*, 48(15):e2021GL093844.

Uppström, L. R. (1974). The boron/chlorinity ratio of deep-sea water from the Pacific Ocean. *Deep Sea Research and Oceanographic Abstracts*, 21(2):161–162.

van Heuven, S., Pierrot, D., Rae, J., Lewis, E., and Wallace, D. (2011). MATLAB program developed for CO2 system calculations.

Waga, H. and Hirawake, T. (2020). Changing occurrences of fall blooms associated with variations in phytoplankton size structure in the Pacific Arctic. *Frontiers in Marine Science*, 7:209.

Walsh, J. E. and Chapman, W. L. (2001). 20th-century sea-ice variations from observational data. *Annals of Glaciology*, 33:444–448.

Wang, H., Lin, P., Pickart, R. S., and Cross, J. N. (2022). Summer surface CO2 dynamics on the Bering Sea and eastern Chukchi Sea shelves from 1989 to 2019. *Journal of Geophysical Research: Oceans*, 127(1):e2021JC017424.

Wiseman, W., Swenson, E. M., and Power, J. (1990). Salinity trends in Louisiana estuaries. *Estuaries*, 13:265–271.

Woosley, R. J. and Millero, F. J. (2020). Freshening of the western Arctic negates anthropogenic carbon uptake potential. *Limnology and oceanography*, 65(8):1834–1846.

Wynn, J. G., Robbins, L., and Anderson, L. (2016). Processes of multibathyal aragonite undersaturation in the Arctic Ocean. *Journal of Geophysical Research: Oceans*, 121(11):8248–8267.

Xue, L., Yang, X., Li, Y., Li, L., Jiang, L.-Q., Xin, M., Wang, Z., Sun, X., and Wei, Q. (2020). Processes controlling sea surface pH and aragonite saturation state in a large northern temperate bay: Contrasting temperature effects. *Journal of Geophysical Research: Biogeosciences*, 125(7):e2020JG005805.

Yamamoto-Kawai, M., McLaughlin, F. A., Carmack, E. C., Nishino, S., and Shimada, K. (2009). Aragonite undersaturation in the Arctic Ocean: effects of ocean acidification and sea ice melt. *Science*, 326(5956):1098–1100.

Zeebe, R. E., Ridgwell, A., and Zachos, J. C. (2016). Anthropogenic carbon release rate unprecedented during the past 66 million years. *Nature Geoscience*, 9(4):325–329.

Zhang, S., Bai, Y., He, X., Jiang, Z., Li, T., Gong, F., Yu, S., and Pan, D. (2023). Spatial and temporal variations in sea surface pCO2 and air-sea flux of CO2 in the Bering Sea revealed by satellite-based data during 2003-2019. *Frontiers in Marine Science*, 10:1099916.

Zhang, Y., Wei, H., Lu, Y., Luo, X., Hu, X., and Zhao, W. (2020a). Dependence of Beaufort Sea low ice condition in the summer of 1998 on ice export in the prior winter. *Journal of Climate*, 33(21):9247–9259.

Zhang, Y., Yamamoto-Kawai, M., and Williams, W. (2020b). Two decades of ocean acidification in the surface waters of the Beaufort Gyre, Arctic Ocean: effects of sea ice melt and retreat from 1997–2016. *Geophysical Research Letters*, 47(3):e60119. e60119 2019GL086421.

Zuo, H., Balmaseda, M. A., Tietsche, S., Mogensen, K., and Mayer, M. (2019). The ECMWF operational ensemble reanalysis-analysis system for ocean and sea ice: a description of the system and assessment. *Ocean science*, 15(3):779–808.

A. Cruise Data Summary Table

Table 6: Summary of cruise data from discrete bottle samples. An X denotes the measured parameters provided in the dataset. Notes: (1) GLODAP v2.2022 (2) NCEI (3) PANGAEA (4) DataONE (5) Arctic Data Center (6) No measurement error reported.

EXPOCODE	DIC	TA	pH	pCO2	Year	Notes	DOI
318M19730822	X	X	X	X	1973	1	doi.org/10.25921/27a9-8r69
18TH19740811	X	X	X	X	1974	1	doi.org/10.3334/cdiac/otg.ios_arct_carbn
18AW19860910	X				1986	1	doi.org/10.3334/cdiac/otg.ios_arct_carbn
18PZ19861014	X				1986	1	doi.org/10.3334/cdiac/otg.clivar_line_p_2009
189119870330	X				1987	1	doi.org/10.3334/cdiac/otg.ios_arct_carbn
18DD19870731	X				1987	1	doi.org/10.3334/cdiac/otg.ios_arct_carbn
18EN19870330	X				1987	1	doi.org/10.3334/cdiac/otg.clivar_line_p_2009
18EN19870717	X				1987	1	doi.org/10.3334/cdiac/otg.clivar_line_p_2009
18PZ19870923	X				1987	1	doi.org/10.3334/cdiac/otg.clivar_line_p_2009
18PZ19871124	X				1987	1	doi.org/10.3334/cdiac/otg.clivar_line_p_2009
18PZ19880502	X				1988	1	doi.org/10.3334/cdiac/otg.clivar_line_p_2009
18PZ19880628	X				1988	1	doi.org/10.3334/cdiac/otg.clivar_line_p_2009
18PZ19881129	X				1988	1	doi.org/10.3334/cdiac/otg.clivar_line_p_2009
18DD19890213	X				1989	1	doi.org/10.3334/cdiac/otg.clivar_line_p_2009
18PZ19890501	X				1989	1	doi.org/10.3334/cdiac/otg.clivar_line_p_2009
18PZ19891003	X				1989	1	doi.org/10.3334/cdiac/otg.clivar_line_p_2009
18HS19900906	X				1990	1	doi.org/10.3334/cdiac/otg.ios_arct_carbn
18PZ19900509	X				1990	1	doi.org/10.3334/cdiac/otg.clivar_line_p_2009
18PZ19900822	X				1990	1	doi.org/10.3334/cdiac/otg.clivar_line_p_2009
18EN19911017	X				1991	1	doi.org/10.3334/cdiac/otg.clivar_line_p_2009
31DS19910216	X				1991	1	doi.org/10.3334/cdiac/otg.31dicgc91_2
31DS19910307	X				1991	1	doi.org/10.3334/cdiac/otg.31dicgc91_2

Table 6 continued from previous page

EXPOCODE	DIC	TA	pH	pCO2	Year	Notes	DOI
77DN19910726	X	X	X	X	1991	1	doi.org/10.3334/cdiac/otg.carina_77dn19910726
18DD19920203	X	X	X	X	1992	1	doi.org/10.3334/cdiac/otg.clivar_line_p_2009
18DD19920908	X				1992	1	doi.org/10.3334/cdiac/otg.clivar_line_p_2009
18HS19920920	X				1992	1	doi.org/10.3334/cdiac/otg.ios_arct_carbn
322019920816	X	X	X	X	1992	1	doi.org/10.3334/cdiac/otg.ndp075
49HG19920807	X	X	X	X	1992	1	doi.org/10.3334/cdiac/otg.pacifica_49hg19920807
18DD19930226	X				1993	1	doi.org/10.3334/cdiac/otg.clivar_line_p_2009
18DD19930514	X	X	X	X	1993	1	doi.org/10.3334/cdiac/otg.clivar_line_p_2009
18HS19930824	X	X	X	X	1993	1	doi.org/10.3334/cdiac/otg.ios_arct_carbn
325019930515	X	X	X	X	1993	1	doi.org/10.3334/cdiac/otg.325021_1
325019930705	X	X	X	X	1993	1	doi.org/10.3334/cdiac/otg.325023_1
49HG19930413	X	X	X	X	1993	1	doi.org/10.3334/cdiac/otg.pacifica_49hg19930413
49HG19930807	X	X	X	X	1993	1	doi.org/10.3334/cdiac/otg.pacifica_49hg19930807
49OS19930611	X	X			1993	1	doi.org/10.3334/cdiac/otg.pacifica_49os19930611
18DD19940510	X	X	X	X	1994	1	doi.org/10.3334/cdiac/otg.clivar_line_p_2009
18DD19940906	X	X	X	X	1994	1	doi.org/10.3334/cdiac/otg.18dd9403_1_2
18SN19940724	X	X	X	X	1994	1	doi.org/10.3334/cdiac/otg.carina_18sn19940724
49HG19940413	X	X	X	X	1994	1	doi.org/10.3334/cdiac/otg.pacifica_49hg19940413
49HG19940808	X	X	X	X	1994	1	doi.org/10.3334/cdiac/otg.pacifica_49hg19940808
90AQ19940706	X	X	X	X	1994	1	doi.org/10.3334/cdiac/otg.carina_90aq19940706
18DD19950207	X				1995	1	doi.org/10.3334/cdiac/otg.clivar_line_p_2009
18DD19950508	X				1995	1	doi.org/10.3334/cdiac/otg.clivar_line_p_2009
18SN19950803	X	X	X	X	1995	1	doi.org/10.3334/cdiac/otg.ios_arct_carbn
49HG19950807	X	X	X	X	1995	1	doi.org/10.3334/cdiac/otg.pacifica_49hg19950807
06AQ19960712	X	X	X	X	1996	1	doi.org/10.3334/cdiac/otg.carina_06aq19960712
18DD19960219	X	X	X	X	1996	1	doi.org/10.3334/cdiac/otg.clivar_line_p_2009
18DD19960506	X	X	X	X	1996	1	doi.org/10.3334/cdiac/otg.clivar_line_p_2009
18DD19960812	X	X	X	X	1996	1	doi.org/10.3334/cdiac/otg.clivar_line_p_2009

Table 6 continued from previous page

EXPOCODE	DIC	TA	pH	pCO2	Year	Notes	DOI
18SN19960910	X	X	X	X	1996	1	doi.org/10.3334/cdiac/otg.ios_arct_carbn
49HG19960807	X	X	X	X	1996	1	doi.org/10.3334/cdiac/otg.pacifica_49hg19960807
18DD19970212	X	X	X	X	1997	1	doi.org/10.3334/cdiac/otg.clivar_line_p_2009
18DD19970604	X	X	X	X	1997	1	doi.org/10.3334/cdiac/otg.clivar_line_p_2009
18DD19970827	X	X	X	X	1997	1	doi.org/10.3334/cdiac/otg.clivar_line_p_2009
18SN19970831	X	X			1997	1	doi.org/10.3334/cdiac/otg.carina_18sn19970831
18SN19970924	X	X	X	X	1997	1	doi.org/10.3334/cdiac/otg.carina_18sn19970924
49NZ19971111	X	X	X	X	1997	1	doi.org/10.3334/cdiac/otg.pacifica_49nz19971111
18DD19980219	X				1998	1	doi.org/10.3334/cdiac/otg.clivar_line_p_2009
49HO19980718	X	X	X	X	1998	1	doi.org/10.3334/cdiac/otg.pacifica_49ho19980718
18DD19990602	X	X	X	X	1999	1	doi.org/10.3334/cdiac/otg.clivar_line_p_2009
18DD19990824	X	X	X	X	1999	1	doi.org/10.3334/cdiac/otg.clivar_line_p_2009
49HO19990719	X	X	X	X	1999	1	doi.org/10.3334/cdiac/otg.pacifica_49ho19990719
49K619990523	X	X	X	X	1999	1	doi.org/10.3334/cdiac/otg.woce_p01_1999
49NZ19990508	X	X	X	X	1999	1	doi.org/10.3334/cdiac/otg.pacifica_49nz19990508
49NZ19990823	X	X	X	X	1999	1	doi.org/10.3334/cdiac/otg.woce_p01_1999
49NZ19990911	X	X			1999	1	doi.org/10.3334/cdiac/otg.pacifica_49nz19990911
18DD20000208	X	X	X	X	2000	1	doi.org/10.3334/cdiac/otg.clivar_line_p_2009
18DD20000531	X	X	X	X	2000	1	doi.org/10.3334/cdiac/otg.clivar_line_p_2009
18DD20000905	X	X	X	X	2000	1	doi.org/10.3334/cdiac/otg.clivar_line_p_2009
18LU20000705	X	X	X	X	2000	1	doi.org/10.3334/cdiac/otg.ios_arct_carbn
18LU20000902	X	X	X	X	2000	1	doi.org/10.3334/cdiac/otg.ios_arct_carbn
49HG20000912	X	X	X	X	2000	1	doi.org/10.3334/cdiac/otg.pacifica_49hg20000912
49NZ20000105	X	X	X	X	2000	1	doi.org/10.3334/cdiac/otg.pacifica_49nz20000105
49NZ20000803	X	X	X	X	2000	1	doi.org/10.3334/cdiac/otg.pacifica_49nz20000803
18DD20010206	X	X	X	X	2001	1	doi.org/10.3334/cdiac/otg.clivar_line_p_2009
49HG20010813	X	X	X	X	2001	1	doi.org/10.3334/cdiac/otg.pacifica_49hg20010813
49NZ20010604	X	X	X	X	2001	1	doi.org/10.3334/cdiac/otg.pacifica_49nz20010604

Table 6 continued from previous page

EXPOCODE	DIC	TA	pH	pCO2	Year	Notes	DOI
49NZ20010723	X	X	X	X	2001	1	doi.org/10.3334/cdiac/otg.clivar_p17n_2001
49NZ20010828	X	X	X	X	2001	1	doi.org/10.3334/cdiac/otg.pacifica_49nz20010828
18RD20020922	X	X	X	X	2002	1	doi.org/10.3334/cdiac/otg.ios_arct_carbn
18SN20020816	X	X	X	X	2002	1	doi.org/10.3334/cdiac/otg.ios_arct_carbn
32H120020505	X	X	X	X	2002	1	doi.org/10.3334/cdiac/otg.carina_32h120020505
32H120020718	X	X	X	X	2002	1	doi.org/10.3334/cdiac/otg.carina_32h120020718
49NZ20020822	X	X	X	X	2002	1	doi.org/10.3334/cdiac/otg.pacifica_49nz20020822
49NZ20021011	X	X	X	X	2002	1	doi.org/10.3334/cdiac/otg.pacifica_49nz20021011
18DL20030913	X	X	X	X	2003	1	doi.org/10.3334/cdiac/otg.ios_arct_carbn
18DL20031015	X	X	X	X	2003	1	doi.org/10.3334/cdiac/otg.ios_arct_carbn
18DL20031126	X	X	X	X	2003	1	doi.org/10.3334/cdiac/otg.ios_arct_carbn
18SN20030806	X	X	X	X	2003	1	doi.org/10.3334/cdiac/otg.ios_arct_carbn
18VT20030902	X	X	X	X	2003	1	doi.org/10.7289/v5k64gcp
18VT20031201	X	X	X	X	2003	1	doi.org/10.7289/v5k64gcp
49NB20030705	X	X	X	X	2003	1	doi.org/10.3334/cdiac/otg.pacifica_49nb20030705
49NZ20030220	X	X	X	X	2003	1	doi.org/10.3334/cdiac/otg.pacifica_49nz20030220
49UP20030620	X				2003	1	doi.org/10.25921/3rar-a808
18DD20040218	X	X	X	X	2004	1	doi.org/10.3334/cdiac/otg.clivar_line_p_2009
18DD20040602	X	X	X	X	2004	1	doi.org/10.3334/cdiac/otg.clivar_line_p_2009
18DD20040821	X				2004	1	doi.org/10.3334/cdiac/otg.clivar_line_p_2009
18DL20040107	X	X	X	X	2004	1	doi.org/10.3334/cdiac/otg.ios_arct_carbn
18DL20040218	X	X	X	X	2004	1	doi.org/10.3334/cdiac/otg.ios_arct_carbn
18DL20040401	X	X	X	X	2004	1	doi.org/10.3334/cdiac/otg.ios_arct_carbn
18DL20040513	X	X	X	X	2004	1	doi.org/10.3334/cdiac/otg.ios_arct_carbn
18DL20040625	X	X	X	X	2004	1	doi.org/10.3334/cdiac/otg.ios_arct_carbn
18DL20040806	X	X	X	X	2004	1	doi.org/10.3334/cdiac/otg.ios_arct_carbn
32H120040515	X	X	X	X	2004	1	doi.org/10.3334/cdiac/otg.carina_32h120040515
32H120040718	X	X	X	X	2004	1	doi.org/10.3334/cdiac/otg.carina_32h120040718

Table 6 continued from previous page

EXPOCODE	DIC	TA	pH	pCO2	Year	Notes	DOI
49NZ20040327	X	X	X	X	2004	1	doi.org/10.3334/cdiac/otg.pacifica_49nz20040327
49NZ20040807	X	X	X	X	2004	1	doi.org/10.3334/cdiac/otg.pacifica_49nz20040807
49NZ20040901		X			2004	1	doi.org/10.3334/cdiac/otg.pacifica_49nz20040901
49NZ20041013	X	X	X	X	2004	1	doi.org/10.3334/cdiac/otg.pacifica_49nz20041013
49UP20040608	X				2004	1	doi.org/10.3334/cdiac/otg.pacifica_49ry20040608
18DD20050211	X	X	X	X	2005	1	doi.org/10.3334/cdiac/otg.clivar_line_p_2009
18SN20050729	X	X	X	X	2005	1	doi.org/10.3334/cdiac/otg.ios_arct_carbn
49NZ20050228	X	X	X	X	2005	1	doi.org/10.3334/cdiac/otg.pacifica_49nz20050228
49NZ20050913	X	X	X	X	2005	1	doi.org/10.3334/cdiac/otg.pacifica_49nz20050913
49UP20050615	X				2005	1	doi.org/10.3334/cdiac/otg.pacifica_49ry20050615
77DN20050730	X	X	X		2005	1	doi.org/10.3334/cdiac/otg.clivar_77dn20050819
77DN20050819	X	X	X	X	2005	1	doi.org/10.3334/cdiac/otg.clivar_77dn20050819
18DD20060130	X	X	X	X	2006	1	doi.org/10.3334/cdiac/otg.clivar_line_p_2009
18DD20060919	X	X	X	X	2006	1	doi.org/10.3334/cdiac/otg.clivar_line_p_2009
18SN20060805	X	X	X	X	2006	1	doi.org/10.3334/cdiac/otg.ios_arct_carbn
325020060213	X	X	X	X	2006	1	doi.org/10.25921/bvaz-zm17
49NZ20060526	X	X	X	X	2006	1	doi.org/10.3334/cdiac/otg.pacifica_49nz20060526
49NZ20060821	X	X	X	X	2006	1	doi.org/10.3334/cdiac/otg.pacifica_49nz20060821
49UP20060607	X				2006	1	doi.org/10.3334/cdiac/otg.pacifica_49ry20060607
06AQ20070728	X	X	X	X	2007	1	doi.org/10.3334/cdiac/otg.clivar_arkxxii_2
18DD20070208	X	X	X	X	2007	1	doi.org/10.3334/cdiac/otg.clivar_line_p_2009
18DD20070530	X	X	X	X	2007	1	doi.org/10.3334/cdiac/otg.clivar_line_p_2009
18DD20070814	X	X	X	X	2007	1	doi.org/10.3334/cdiac/otg.clivar_line_p_2009
18SN20070704	X	X	X	X	2007	1	doi.org/10.3334/cdiac/otg.ios_arct_carbn
18SN20070726	X	X	X	X	2007	1	doi.org/10.3334/cdiac/otg.ios_arct_carbn
32WC20070511	X	X	X	X	2007	1	doi.org/10.3334/cdiac/otg.clivar_nacp_west_coast_cruise_2007
49NZ20070724	X	X	X	X	2007	1	doi.org/10.3334/cdiac/otg.clivar_p01_2007
49NZ20070904	X	X	X	X	2007	1	doi.org/10.3334/cdiac/otg.pacifica_49nz20070904

Table 6 continued from previous page

EXPOCODE	DIC	TA	pH	pCO2	Year	Notes	DOI
49NZ20071008	X	X	X	X	2007	1	doi.org/10.3334/cdiac/otg.clivar_p14_2007
49UP20070606	X				2007	1	doi.org/10.3334/cdiac/otg.pacifica_49ry20070606
NPEO20070422		X			2007	5, 6	doi.org/10.18739/A25T3FZ8X
18DD20080131	X	X	X	X	2008	1	doi.org/10.3334/cdiac/otg.clivar_line_p_2009
18DD20080813	X	X	X	X	2008	1	doi.org/10.3334/cdiac/otg.clivar_line_p_2009
18LU20080702	X	X	X	X	2008	1	doi.org/10.3334/cdiac/otg.ios_arct_carbn
18LU20080923	X	X	X	X	2008	1	doi.org/10.3334/cdiac/otg.ios_arct_carbn
18SN20080717	X	X	X	X	2008	1	doi.org/10.3334/cdiac/otg.ios_arct_carbn
325020080826	X	X	X	X	2008	1	doi.org/10.3334/cdiac/otg.clivar_tn224_2008
33A020080502	X	X			2008	2	doi.org/10.25921/44kh-zb66
33A020080913	X	X			2008	2	doi.org/10.25921/44kh-zb66
33HQ20080329	X	X	X	X	2008	1	doi.org/10.3334/cdiac/otg.best08spr_33hq20080329 doi.org/10.25921/531n-c230
33HQ20080703	X	X	X	X	2008	1	doi.org/10.25921/px3e-rb18 doi.org/10.25921/531n-c230
49MR0804		X			2008		jamstec.go.jp/iace/e/report/
49NZ20081011	X	X	X	X	2008	1	doi.org/10.3334/cdiac/otg.pacifica_49nz20081011
76XL20080730	X	X			2008	2	doi.org/10.25921/d4te-fs53
90JS20080815	X	X	X	X	2008	1	doi.org/10.25921/0sv9-dj92
ARKXXIII/3		X			2008	2	ncei.noaa.gov/archive/accession/0065370
NPEO20080321		X			2008	5, 6	doi.org/10.18739/A25T3FZ8X
NPEO20080406		X			2008	5, 6	doi.org/10.18739/A25T3FZ8X
18DL20090730		X	X		2009		doi.org/10.17882/75345
18LU20090710	X	X	X	X	2009	1	doi.org/10.3334/cdiac/otg.ios_arct_carbn
18SN20090917	X	X	X	X	2009	1	doi.org/10.3334/cdiac/otg.ios_arct_carbn
316N20090614	X	X	X	X	2009	1	doi.org/10.25921/sqkj-f093 doi.org/10.25921/531n-c230

Table 6 continued from previous page

EXPOCODE	DIC	TA	pH	pCO2	Year	Notes	DOI
31FN20090924	X	X	X	X	2009	1	doi.org/10.25921/14tb-zk16 doi.org/10.25921/531n-c230
33A020090503	X	X			2009	2	doi.org/10.25921/n43y-9r47
33A020090914	X	X			2009	2	doi.org/10.25921/n43y-9r47
33HQ20090403	X	X	X	X	2009	1	doi.org/10.25921/f6g1-3d67 doi.org/10.25921/531n-c230
49MR0903	X	X			2009		jamstec.go.jp/iace/e/report/
49UF20090610	X				2009	1	doi.org/10.25921/7z5a-zj52
18DD20100203	X	X	X	X	2010	1	doi.org/10.3334/cdiac/otg.clivar_line_p_2009
18DD20100606	X	X	X	X	2010	1	doi.org/10.3334/cdiac/otg.clivar_line_p_2009
18DD20100720	X	X	X	X	2010	1	doi.org/10.7289/v5k64gcp
18SN20100915	X	X	X	X	2010	1	doi.org/10.25921/w3rp-tx17
18VT20100403	X	X	X	X	2010	1	doi.org/10.7289/v5k64gcp
18VT20100805	X	X	X	X	2010	1	doi.org/10.7289/v5k64gcp
18VT20101029	X	X	X	X	2010	1	doi.org/10.7289/v5k64gcp
325020100509	X	X	X	X	2010	1	doi.org/10.25921/kjhg-2n93
32QO20100503	X	X			2010	2	doi.org/10.25921/avxr-m571
33A020100914	X	X			2010	2	doi.org/10.25921/avxr-m571
33HQ20100907	X	X			2010	1	doi.org/10.3334/cdiac/otg.clivar_33hq20100907
49MR1005	X	X			2010		jamstec.go.jp/iace/e/report/
49UF20100811	X	X	X	X	2010	1	doi.org/10.25921/nfk6-b019
76XL20100709	X	X			2010	2	doi.org/10.7289/v5862dr7
76XL20100710	X	X			2010	5	doi.org/10.18739/A2928P
06AQ20110805	X	X	X	X	2011	1	doi.org/10.25921/d0zx-ew89
18DD20110621	X	X	X	X	2011	1	doi.org/10.7289/v5k64gcp
18SN20110721	X	X	X	X	2011	1	doi.org/10.25921/y1cw-db38
18VT20110404	X	X	X	X	2011	1	doi.org/10.7289/v5k64gcp
18VT20110805	X	X	X	X	2011	1	doi.org/10.7289/v5k64gcp

Table 6 continued from previous page

EXPOCODE	DIC	TA	pH	pCO2	Year	Notes	DOI
18VT20110909	X	X	X	X	2011	1	doi.org/10.7289/v5k64gcp
18VT20111124	X	X	X	X	2011	1	doi.org/10.7289/v5k64gcp
32WC20110812	X	X	X	X	2011	1	doi.org/10.7289/v5jq0xz1
33A009072011	X	X			2011	2	doi.org/10.25921/07yn-b044
33A020110506	X	X			2011	2	doi.org/10.25921/07yn-b044
33HQ20111003		X	X		2011	2	doi.org/10.3334/cdiac/otg.clivar_33hq20111003
49RY20110515	X	X	X	X	2011	1	doi.org/10.3334/cdiac/otg.clivar_p13_2011
NPEO20110416		X			2011	5, 6	doi.org/10.18739/A25T3FZ8X
18SN20120802	X	X	X	X	2012	1	doi.org/10.25921/c5kx-sm59
18VT20120401	X	X	X	X	2012	1	doi.org/10.7289/v5k64gcp
18VT20120405	X	X	X	X	2012	1	doi.org/10.7289/v5k64gcp
18VT20120613	X	X	X	X	2012	1	doi.org/10.7289/v5k64gcp
18VT20120714	X	X	X	X	2012	1	doi.org/10.7289/v5k64gcp
18VT20120919	X	X	X	X	2012	1	doi.org/10.7289/v5k64gcp
332220120904	X	X	X	X	2012	1	doi.org/10.25921/e7m6-gh32 doi.org/10.25921/531n-c230
33A020120503	X	X			2012	2	doi.org/10.25921/mttc-gc63
33A020120913	X	X			2012	2	doi.org/10.25921/mttc-gc63
33HQ20121005	X	X			2012	1	doi.org/10.3334/cdiac/otg.clivar_33hq20121005
49MR12E03	X	X			2012		https://www.jamstec.go.jp/iace/e/report/
49UP20120602	X	X	X	X	2012	1	doi.org/10.25921/vwtv-xw29
CHINARE2012			X		2012		doi.org/10.17632/vytzhmm254.2
18SN20130724	X	X	X	X	2013	1	doi.org/10.25921/7r17-4q18
317W20130803	X	X	X	X	2013	1	doi.org/10.7289/v5c53hxp
33A020130427	X	X			2013	2	doi.org/10.25921/n5dy-h455
33A020130914	X	X			2013	2	doi.org/10.25921/n5dy-h455
33HQ20131005	X	X			2013	2	doi.org/10.3334/cdiac/otg.clivar_33hq20131005
49NZ20130828	X	X			2013		jamstec.go.jp/iace/e/report/

Table 6 continued from previous page

EXPOCODE	DIC	TA	pH	pCO2	Year	Notes	DOI
49UF20130531	X	X	X	X	2013	1	doi.org/10.25921/asrw-nh27
18DD20140212	X	X	X	X	2014	1	doi.org/10.3334/cdiac/otg.clivar_line_p_2009
18DL20140817	X	X			2014	3	doi.org/10.1594/PANGAEA.886238
18SN20140921	X	X	X	X	2014	1	doi.org/10.25921/jkqw-ya62
18VT20141027	X	X	X	X	2014	1	doi.org/10.25921/vr8n-x476
32H120140516	X	X			2014	5	doi.org/10.18739/A27W6763M
33A020140503	X	X			2014	2	doi.org/10.25921/ke3w-xp11
33A020140913	X	X			2014	2	doi.org/10.25921/ke3w-xp11
49NZ20140717	X	X	X	X	2014	1	doi.org/10.25921/x4pw-g263
49NZ20140831	X	X			2014		jamstec.go.jp/iace/e/report/
49UF20140512	X	X	X	X	2014	1	doi.org/10.25921/pjv7-3s61
77DN20140705	X	X			2014	3	doi.org/10.1594/PANGAEA.843909
CHINAIRE2014			X		2014		doi.org/10.17632/vytzhmm254.2
NPEO20140415		X			2014	5, 6	doi.org/10.18739/A25T3FZ8X
06AQ20150817	X	X	X	X	2015	1	doi.org/10.7289/v5319t5z
18DL20150710	X	X	X	X	2015	1	doi.org/10.25921/651b-8d31
18DL20150714	X	X			2015	3	doi.org/10.1594/PANGAEA.929298
18DL20150905	X	X	X	X	2015	1	doi.org/10.25921/4xsw-e696
18SN20150920	X	X	X	X	2015	1	doi.org/10.25921/c35k-0h70
18VT20150401	X	X	X	X	2015	1	doi.org/10.25921/0cnc-x944
33A020150505	X	X			2015	2	doi.org/10.25921/r7kp-0j46
33A020150914	X	X			2015	2	doi.org/10.25921/r7kp-0j46
33HQ20150809	X	X	X	X	2015	1	doi.org/10.3334/cdiac/otg.clivar_arc01_33hq20150809
33RO20150525	X	X	X	X	2015	1	doi.org/10.3334/cdiac/otg.go_ship_p16n_2015
33RO20150713	X	X			2015	2	doi.org/10.25921/dey6-9h45
49MR1503	X	X			2015		jamstec.go.jp/iace/e/report/
49UP20150604	X	X	X	X	2015	1	doi.org/10.25921/g9qx-v677
18DD20160208	X	X	X	X	2016	1	doi.org/10.3334/cdiac/otg.clivar_line_p_2009

Table 6 continued from previous page

EXPOCODE	DIC	TA	pH	pCO2	Year	Notes	DOI
18DD20160605	X	X	X	X	2016	1	doi.org/10.3334/cdiac/otg.clivar_line_p_2009
18DD20160817	X	X	X	X	2016	1	doi.org/10.3334/cdiac/otg.clivar_line_p_2009
18SN20160922	X	X	X	X	2016	1	doi.org/10.25921/jy88-9n09
24HU20160805	X	X			2016		doi.org/10.25921/rycv-m555
33A020160430	X	X			2016	2	doi.org/10.25921/ed32-3h29
33A020160915	X	X			2016	2	doi.org/10.25921/ed32-3h29
33RO20160505	X	X	X	X	2016	1	doi.org/10.7289/v5v40shg
49UP20160608	X	X	X	X	2016	1	doi.org/10.25921/jffc-4p98
CHINARE2016			X		2016		doi.org/10.17632/vytzhmm254.2
18DD20170205	X	X	X	X	2017	1	doi.org/10.3334/cdiac/otg.clivar_line_p_2009
18DD20170604	X	X	X	X	2017	1	doi.org/10.3334/cdiac/otg.clivar_line_p_2009
24HU20170806	X	X			2017		doi.org/10.25921/rycv-m555
332220170918	X	X	X	X	2017	1	doi.org/10.25921/3qa5-v720
33A020170501	X	X			2017	2	doi.org/10.25921/rvm1-vj65
33A020170916	X	X			2017	2	doi.org/10.25921/rvm1-vj65
33HQ20170826	X	X	X	X	2017	1	doi.org/10.25921/pks4-4p43
49MR1705C	X	X			2017		jamstec.go.jp/iace/e/report/
49UP20170623	X	X	X	X	2017	1	doi.org/10.25921/bd00-5226
RVAKADEMIK201709	X				2017	6	doi.org/10.1134/S0016702920080054
18DN20180803	X	X			2018	2	doi.org/10.25921/6pye-2x72
18LU20180218	X				2018	1	doi.org/10.3334/cdiac/otg.clivar_line_p_2009
24HU20180804	X	X			2018		doi.org/10.25921/rycv-m555
33HQ20180807	X	X	X	X	2018	1	doi.org/10.25921/xc4b-xh20
49UP20180614	X	X	X	X	2018	1	doi.org/10.25921/vzkj-kr87
76XL20180723			X		2018	2	doi.org/10.25921/xv5b-r238
CHINARE2018			X		2018		doi.org/10.17632/vytzhmm254.2
MR1805C	X				2018		jamstec.go.jp/iace/e/report/
SKQ201810S	X			X	2018	4	doi.org/10.24431/rw1k45g

Table 6 continued from previous page

EXPOCODE	DIC	TA	pH	pCO2	Year	Notes	DOI
TGX201809	X	X			2018	4	doi.org/10.24431/rw1k45g
WSD201807	X			X	2018	4	doi.org/10.24431/rw1k45g
18DD20190205	X	X	X	X	2019	1	doi.org/10.3334/cdiac/otg.clivar_line_p_2009
18DD20190602	X	X	X	X	2019	1	doi.org/10.3334/cdiac/otg.clivar_line_p_2009
18DN20190802	X	X			2019	2	doi.org/10.25921/yayq-gc09
33HQ20190806	X	X	X	X	2019	1	doi.org/10.25921/b5s5-py61
49NZ20190927	X	X			2019		jamstec.go.jp/iace/e/report/
49UP20190516	X	X	X	X	2019	1	doi.org/10.25921/skr2-r320
CHINARE2019			X		2019		doi.org/10.17632/vytzhmm254.2
SKQ201915S	X	X			2019	4	doi.org/10.24431/rw1k45g
TGX201904	X	X			2019	4	doi.org/10.24431/rw1k45g
TGX201909	X	X	X		2019	4	doi.org/10.24431/rw1k45g
33BI20201025	X	X			2020	2	doi.org/10.25921/pnsd-sv10
49NZ20200919	X	X			2020		jamstec.go.jp/iace/e/report/
49UP20200730	X	X	X	X	2020	1	doi.org/10.25921/ga52-xk29
RVARAON20200717		X			2020		doi.org/10.5061/dryad.fbg79cnvp
SKQ202010S	X	X			2020	4	doi.org/10.24431/rw1k45g
SKQ202012S	X	X			2020	4	doi.org/10.24431/rw1k45g
33BI20211108	X	X			2021	2	doi.org/10.25921/29r3-4z87
49UF20210515	X	X	X	X	2021	1	doi.org/10.25921/f20y-3w61
77DN20210725	X	X	X		2021	2	doi.org/10.25921/eaf4-9658
SKQ202106S	X	X			2021	4	doi.org/10.24431/rw1k45g
SKQ202110S	X	X			2021	4	doi.org/10.24431/rw1k45g
TGX202109	X	X	X		2021	4	doi.org/10.24431/rw1k45g

B. SSS and SST Effect on Calculation Uncertainty

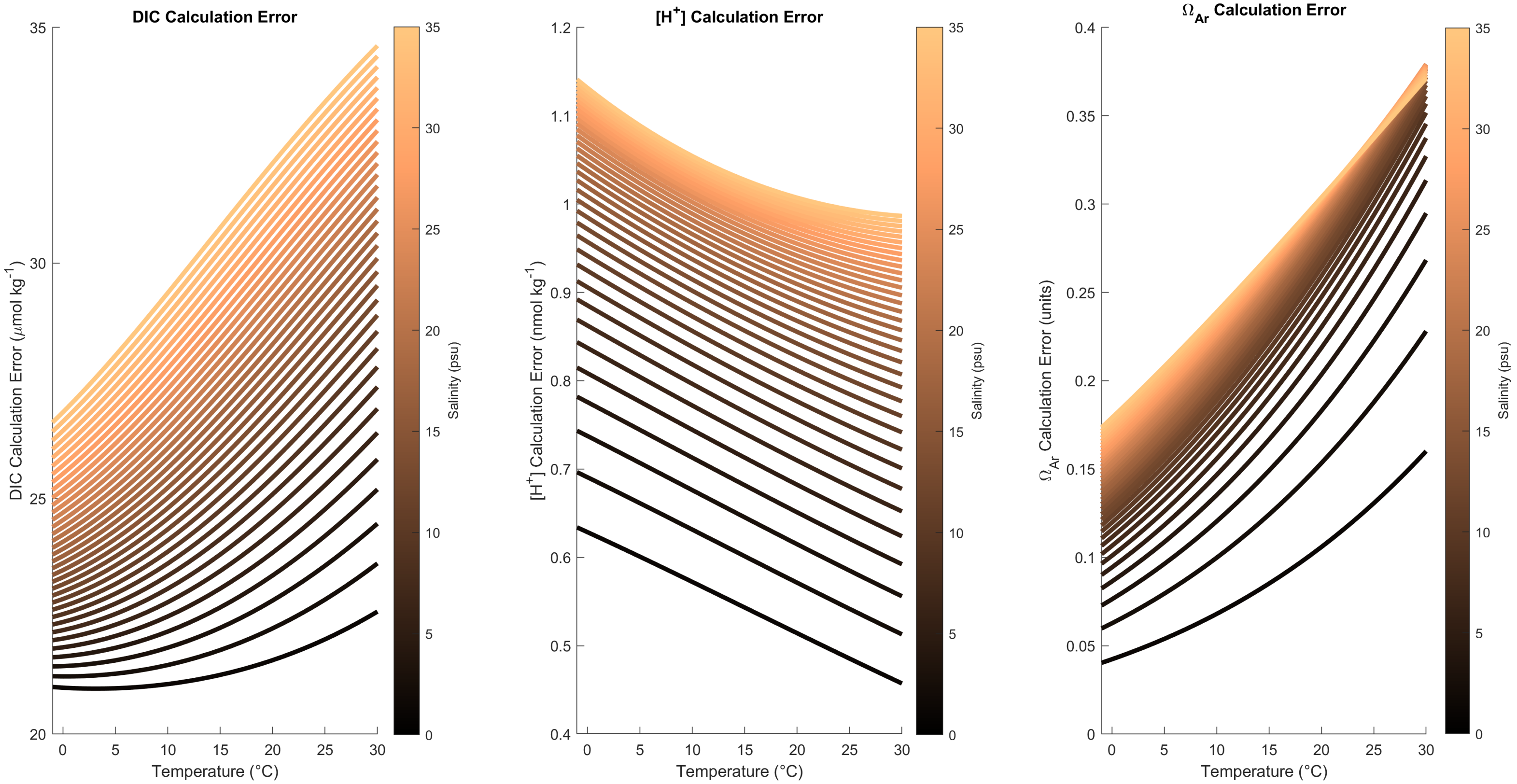

Figure 13: Plots showing calculation error (calculated using errors.m) for DIC, [H$^+$], and Ω_{Ar} based on the following input parameters: TA $=$ 2150 μmol kg^{-1}, pCO$_2$ $=$ 350 μatm, TA$_{Err}$ $=$ 20 μmol kg^{-1}, pCO$_{2Err}$ $=$ 50 μatm. Colored lines denote discrete salinity values from 0-35 psu. Note that, while the exact values plotted will vary based on input parameters, this represents overall relationships in calculation error as a function of temperature and salinity.

C. TA Prediction Results by Subregion

Table 7: Detailed TA prediction results for all models and equations, organized by subregion.

		LIAR	Equation 1			Equation 2			Equation 3			Equation 4		
			OLS	Robust	GWR	OLS	Robust	GWR	OLS	Robust	GWR	OLS	Robust	GWR
	RMSE	76.9	26.3	26.5	25.6	26.3	26.6	25	26.3	26.6	24.4	26.2	28.1	25.3
	MAE	68.5	18.2	18	17.1	18.2	18	16.8	18.2	18	16.4	17.6	17.4	16.5
	MBE	67.04	-0.03	-3.16	1.2	-0.03	-3.21	0.47	-0.06	-3.24	0.44	-0.13	-4.1	0.91
Arctic	R^2	0.35	0.924	0.923	0.928	0.924	0.923	0.931	0.924	0.922	0.935	0.925	0.913	0.93
Ocean	AICc	8379	6281	6298	6258	6285	6303	6215	6283	6304	6166	6278	6414	6236
	a	-	450.5 ± 5.7	413.3 ± 2.6	447.4 ± 111.4	449.9 ± 5.1	415.3 ± 2.6	441.7 ± 106.5	466.5 ± 7.8	418.4 ± 4.4	254.9 ± 700.8	315 ± 106.8	-417.8 ± 43	-361.9 ± 1225.7
N=964	*b*	-	55.3 ± 0.2	56.5 ± 0.1	55.5 ± 3.9	55.3 ± 0.2	56.5 ± 0.1	55.6 ± 3.9	54.7 ± 0.3	56.3 ± 0.2	61.9 ± 23.2	66 ± 7.8	117.3 ± 3.1	111.1 ± 86.1
	c	-	-	-	-	0.1 ± 0.3	-0.4 ± 0.3	-0.7 ± 13.6	32.1 ± 4.9	4 ± 3.9	-94.9 ± 497.8	-3.6 ± 0.3	-3.9 ± 0.2	-26.7 ± 176.2
	d	-	-	-	-	-	-	-	-1.2 ± 0.2	-0.2 ± 0.2	3.1 ± 16.5	-0.2 ± 0.1	-1.1 ± 0.1	-1 ± 1.5
	e	-	-	-	-	-	-	-	-	-	-	2.4 ± 0.2	2.8 ± 0.1	-5.8 ± 59.5
	RMSE	182.7	68.5	99.9	51	66.2	99.7	54.4	65.4	76.2	57.2	58.2	60	58.1
	MAE	120.7	41.6	49.1	26.9	41.4	49.4	28.7	38.5	40.1	29.3	36	35.9	33.4
	MBE	115.09	0.46	12.68	3.93	-1.31	12.43	3.28	-2.32	5.25	4.79	-1.64	-2.86	-1.58
East Siberian Sea	R^2	0.698	0.96	0.916	0.977	0.962	0.915	0.973	0.963	0.95	0.97	0.97	0.968	0.969
	AICc	787	596	649	594	593	651	606	594	615	616	580	584	620
	a	-	199.6 ± 29.4	496 ± 100.3	418.9 ± 225.2	185.1 ± 29.4	440.7 ± 106.1	522.9 ± 349.6	226.5 ± 33.3	310.3 ± 98	471.6 ± 278.5	-58.6 ± 37.1	88.2 ± 64	138.9 ± 781.4
N=75	*b*	-	63.6 ± 1	52.7 ± 3.5	55.3 ± 8.7	64 ± 1	54.7 ± 3.7	51.4 ± 13.5	62.3 ± 1.2	59 ± 3.4	53.4 ± 10.7	96.9 ± 2.9	84.3 ± 4.9	82.9 ± 52.3
	c	-	-	-	-	13.7 ± 1.5	3 ± 2.7	-13.6 ± 15.4	133.2 ± 21.5	175 ± 45.3	-1.5 ± 80.8	-5.3 ± 2.1	-6.1 ± 1.4	-15.3 ± 16.4
	d	-	-	-	-	-	-	-	-4.5 ± 0.8	-6 ± 1.5	-0.5 ± 3	-0.9 ± 0.1	-0.6 ± 0.1	-0.6 ± 0.9
	e	-	-	-	-	-	-	-	-	-	-	3.9 ± 0.6	5.1 ± 1.6	2.1 ± 5
	RMSE	31.3	11.8	13.8	13.3	12.9	12.9	18.4	12.2	12.2	14.7	325.8	330.4	55.1
	MAE	24.4	9	10.1	11.8	9.8	9.9	13.2	8.8	9	12.5	120.4	122.1	30.4
	MBE	14.47	0.51	1.73	6.06	1.11	1.04	8.21	3.08	2.95	3.53	105.78	107.22	24.63
Upper	R^2	0.742	0.968	0.956	0.959	0.956	0.956	0.91	0.954	0.954	0.934	0	0	0.119
Arc.	AICc	73	50	53	53	57	57	63	63	63	66	134	134	102
	a	-	68.8 ± 41.2	41.3 ± 72.3	214.2 ± 66.2	78.5 ± 94.1	72.4 ± 82.6	312.5 ± 131.4	-3699.8 ± 1347	-3699 ± 1334.8	-354.1 ± 491.7	-30174 ± 15660	-30281 ± 15922	-2872 ± 7121
N=9	*b*	-	67.4 ± 1.4	68.3 ± 2.5	62.8 ± 2.1	67 ± 3.2	67.2 ± 2.8	59.2 ± 4.4	196 ± 46	196 ± 45.6	81.7 ± 17	2017.3 ± 1014	2024.3 ± 1031	264.9 ± 468.6
	c	-	-	-	-	-0.6 ± 3.1	-0.7 ± 2.7	-10.6 ± 6.2	-2316.9 ± 808.4	-2318.6 ± 801.9	-473.9 ± 352	89.1 ± 266.7	90.3 ± 270.4	8.2 ± 43.8
	d	-	-	-	-	-	-	-	79.1 ± 27.6	79.1 ± 27.4	15.7 ± 12	-31.3 ± 16.3	-31.4 ± 16.5	-3.3 ± 7.7
	e	-	-	-	-	-	-	-	-	-	-	-8.1 ± 98.1	-7.7 ± 99.5	4.5 ± 17.9
	RMSE	53.9	34.3	34.1	33.4	34.2	34.1	32.6	33.2	32.8	31.4	36.9	34.9	32.3
	MAE	37.4	23	22.6	21.8	23.1	22.6	21	21.8	21.5	19.4	21.4	20.9	19.9
	MBE	25.82	0.04	-2.69	1.71	0.03	-2.69	1.7	0.03	-1.74	1.38	0.32	-2.54	1.01
Chukchi	R^2	0.762	0.904	0.905	0.909	0.904	0.905	0.913	0.91	0.912	0.919	0.888	0.9	0.914
Sea	AICc	13594	12020	12000	11957	12017	12002	11878	11917	11878	11754	12281	12088	11855
	a	-	511.6 ± 17.5	505.5 ± 3.3	554.5 ± 116.8	516.9 ± 18.1	505.8 ± 3.9	550.2 ± 114.5	431.8 ± 24.4	427.5 ± 3.5	404.4 ± 88.7	190.1 ± 370.7	-758.2 ± 89.6	165.5 ± 644.6
N=1704	*b*	-	53 ± 0.6	53.1 ± 0.1	51.7 ± 3.7	52.7 ± 0.6	53.1 ± 0.1	51.7 ± 3.9	55.6 ± 0.8	55.6 ± 0.1	56.5 ± 2.7	76.6 ± 25.3	139.6 ± 6.1	79.9 ± 43
	c	-	-	-	-	0.9 ± 0.1	0 ± 0.1	0.1 ± 2.2	63.5 ± 5.8	64.9 ± 1.6	68.1 ± 34.1	-5 ± 0.2	-6.5 ± 0.2	-4.8 ± 2.5
	d	-	-	-	-	-	-	-	-2.1 ± 0.2	-2.1 ± 0.1	-2.3 ± 1	-0.4 ± 0.4	-1.5 ± 0.1	-0.5 ± 0.7
	e	-	-	-	-	-	-	-	-	-	-	1 ± 0	1 ± 0	1.1 ± 0.5

Table 7 continued from previous page

		LIAR	Equation 1			Equation 2			Equation 3			Equation 4		
RMSE	90.2	91.6	92.4	78.2	88.6	89	78.2	82.7	82.7	76.4	86.8	103.1	76.9	
	MAE	62.7	61.7	61.3	40	61.6	60.8	39.8	57.1	56.3	37.6	56.4	53.8	39.5
	MBE	20.14	0.43	-6.59	-3.71	0.41	-3.75	-3.99	0.45	-4.1	-3.57	0.53	2.05	-2.82
Beaufort	R^2	0.602	0.589	0.582	0.761	0.615	0.611	0.76	0.664	0.665	0.771	0.63	0.478	0.767
Sea	AICc	10596	10574	10594	4799	10500	10511	4802	10341	10340	4777	10454	10857	4787
	a	-	1034.8 ± 21.9	904.4 ± 27.6	566.5 ± 92.1	998.4 ± 20.3	955.6 ± 18.6	560.1 ± 84.8	788.5 ± 23.7	732.2 ± 31.7	470.8 ± 65.7	1261.7 ± 99.9	2789.6 ± 45	247.3 ± 224.7
N=1176	*b*	-	35.8 ± 0.8	40.4 ± 1	51.7 ± 3	36.7 ± 0.8	38.3 ± 0.7	51.9 ± 2.8	44.5 ± 0.9	46.5 ± 1.1	55.1 ± 2.1	12.5 ± 7.7	-105.1 ± 3.4	78.5 ± 15.4
	c	-	-	-	-	9.3 ± 0.2	5.6 ± 0.4	0.9 ± 2	92.2 ± 5.5	90.5 ± 6.4	85.2 ± 13.1	-3.3 ± 0.8	-6.3 ± 0.4	-6.5 ± 1.4
	d	-	-	-	-	-	-	-	-3.2 ± 0.2	-3.1 ± 0.2	-3 ± 0.5	0.5 ± 0.1	2.8 ± 0.1	-0.5 ± 0.3
	e	-	-	-	-	-	-	-	-	-	-	2.4 ± 0.1	2 ± 0.1	1.8 ± 0.4
	RMSE	66.4	59.7	59.7	46	58.2	58.2	45.6	55.6	56.6	45.4	56.6	57	50.9
	MAE	48.4	47.1	47.1	34	44.9	44.7	33.2	39.8	38.7	33	40.9	40.4	32.5
	MBE	15.69	-0.09	1.02	1.9	-0.13	0.37	2.19	-0.16	-2.38	1.35	0.08	2.47	2.12
Lower	R^2	0.722	0.777	0.776	0.867	0.787	0.787	0.868	0.805	0.798	0.87	0.798	0.795	0.836
Arc.	AICc	3127	3030	3030	2853	3014	3014	2849	2982	2994	2847	2996	3002	2933
	a	-	586.1 ± 15.2	591.2 ± 17.7	689.9 ± 231.5	577.6 ± 15	563.7 ± 17.1	682.5 ± 231.4	707.1 ± 16.5	746.3 ± 17.8	628.1 ± 340.8	1916.4 ± 304.8	3334.5 ± 167.2	2218.4 ± 1514.9
N=372	*b*	-	52.2 ± 0.5	52 ± 0.6	48.5 ± 7.4	52.8 ± 0.5	53.4 ± 0.6	48.9 ± 7.5	48.1 ± 0.6	46.7 ± 0.7	50.9 ± 11.4	-46 ± 22.1	-150.2 ± 12.4	-66.4 ± 104.8
	c	-	-	-	-	-4.9 ± 0.4	-5.6 ± 0.4	-1.5 ± 5.5	-89.7 ± 6.1	-135.2 ± 5.4	5.5 ± 93.6	-14.3 ± 0.6	-15.9 ± 0.8	-11.4 ± 15
	d	-	-	-	-	-	-	-	3 ± 0.2	4.6 ± 0.2	-0.3 ± 3.3	1.8 ± 0.4	3.7 ± 0.2	2.1 ± 1.8
	e	-	-	-	-	-	-	-	-	-	-	2.2 ± 0.1	2.2 ± 0.2	2.2 ± 2.6
	RMSE	44.7	29.2	33.7	24.1	29.2	33.7	23.7	28.9	36.4	22.8	26.9	29.6	22.9
	MAE	27	21.4	21	16.8	21.5	21	16.4	21.3	21.2	15.9	18.9	18.7	15.8
	MBE	-21.92	0.01	-5.12	-1.15	0	-5.15	-1.1	-0.06	-5.66	-0.76	0.09	-0.71	-0.93
Bering Sea	R^2	0.516	0.356	0.141	0.559	0.353	0.138	0.571	0.367	0.005	0.602	0.449	0.334	0.6
Shelf	AICc	6473	5738	5982	5411	5743	5986	5388	5724	6118	5325	5607	5769	5330
	a	-	1391 ± 25.3	800.2 ± 27.9	1094.3 ± 369.7	1389.2 ± 24.6	807.6 ± 27.5	1107.1 ± 395.3	1053.9 ± 48.3	1088.3 ± 50.6	1170.6 ± 381.5	6142.4 ± 346.6	11022 ± 1155.2	7716.7 ± 4927.2
N=851	*b*	-	24.7 ± 0.8	43.3 ± 0.9	34 ± 11.6	24.8 ± 0.8	43.1 ± 0.9	33.6 ± 12.3	35.4 ± 1.5	34.3 ± 1.6	31.7 ± 12.2	-287.1 ± 22.5	-604.7 ± 72.7	-389.7 ± 313.5
	c	-	-	-	-	0.1 ± 0.1	-0.3 ± 0.1	-0.2 ± 1.1	54.4 ± 7.9	-58.2 ± 5.6	-11.5 ± 80.3	-0.8 ± 0.2	0.9 ± 0.2	-0.6 ± 1.9
	d	-	-	-	-	-	-	-	-1.7 ± 0.2	1.8 ± 0.2	0.3 ± 2.6	5.1 ± 0.4	10.3 ± 1.1	6.8 ± 5
	e	-	-	-	-	-	-	-	-	-	-	0.1 ± 0	-0.2 ± 0	0 ± 0.2
	RMSE	13.9	11.2	12.2	12.7	11.3	12.8	12.4	11	14.5	11.7	9.4	9.3	8.4
	MAE	8.1	7.9	7.5	7	7.9	7.7	6.8	8	7.7	6.4	6.8	6.6	5.4
	MBE	-2.92	-0.04	0.56	1.36	-0.07	0.72	1.32	-0.05	0.99	1.04	-0.2	-0.06	0.41
Bering Sea	R^2	0.377	0.119	0.044	0.153	0.102	0.159	0.102	0.142	0.497	0.023	0.376	0.384	0.487
Basin	AICc	1090	971	1005	1052	976	1027	1044	968	1079	1020	905	903	889
	a	-	1706.9 ± 72.3	1170.2 ± 29.9	1398.7 ± 658.3	1736.2 ± 84.5	1011.7 ± 50.2	1493 ± 764.4	2383.6 ± 173.1	172.1 ± 140.2	2764.2 ± 3164	-16067.5 ± 707	-14306 ± 775.3	-22773 ± 13548
N=206	*b*	-	16 ± 2.2	32.3 ± 0.9	25.4 ± 20.1	15.2 ± 2.6	37 ± 1.5	22.7 ± 23.1	-4.5 ± 5.2	62.5 ± 4.2	-16.2 ± 96.6	1084.1 ± 42	980.5 ± 45.8	1472.5 ± 826.6
	c	-	-	-	-	-0.2 ± 0.1	0.6 ± 0.1	-0.6 ± 1.3	-83.3 ± 16.2	82.3 ± 8.9	-143.3 ± 259.4	-1.6 ± 0.7	-2.9 ± 0.3	4.1 ± 29.2
	d	-	-	-	-	-	-	-	2.5 ± 0.5	-2.5 ± 0.3	4.4 ± 7.9	-16 ± 0.6	-14.5 ± 0.7	-21.7 ± 12.6
	e	-	-	-	-	-	-	-	-	-	-	0.1 ± 0.1	0.2 ± 0	-0.1 ± 1.2
	RMSE	10	14.4	14.9	9.8	14.4	15.4	9.6	14.1	15.8	13	14.4	11.7	9.6
	MAE	6.6	8.8	8.1	6.8	8.7	8.4	6.7	8.8	8.6	7.3	8.5	7.6	6.6
	MBE	0.28	0.16	-1.12	-0.06	0.01	-1.2	-0.32	0.12	-1.2	-1.38	-0.6	1.75	-0.14
Aleutian	R^2	0.642	0.265	0.215	0.664	0.254	0.145	0.675	0.274	0.096	0.395	0.236	0.498	0.663
Chain	AICc	486	537	544	479	540	553	476	538	560	542	545	503	482
	a	-	833.9 ± 209.4	-78.2 ± 102.5	877.5 ± 656.4	986.7 ± 250.4	-151.3 ± 164.8	749.6 ± 1203.4	2555.1 ± 519.4	-363.9 ± 245.9	182.8 ± 4194.7	40210 ± 14228	43916 ± 6385	5742 ± 21550
N=104	*b*	-	42.3 ± 6.4	70.1 ± 3.1	41 ± 20.1	38 ± 7.5	72.3 ± 5	45 ± 36.3	-9.9 ± 15.8	78.7 ± 7.5	62.1 ± 127.6	-2388.5 ± 874.5	-2604.2 ± 387.9	-267.7 ± 1303.4
	c	-	-	-	-	-1.3 ± 0.3	0.3 ± 0.2	-0.7 ± 2.6	-214 ± 64.9	27.2 ± 31.8	34.9 ± 353.6	0.3 ± 1.2	1.5 ± 1	-2.8 ± 15.2
	d	-	-	-	-	-	-	-	6.5 ± 2	-0.8 ± 1	-1.1 ± 10.8	37.5 ± 13.4	40.6 ± 5.9	4.9 ± 19.7
	e	-	-	-	-	-	-	-	-	-	-	0 ± 0.1	-0.1 ± 0.1	0.2 ± 0.9

Table 7 continued from previous page

		LIAR	Equation 1			Equation 2			Equation 3			Equation 4		
Gulf of Alaska N=1687	RMSE	29.4	38.6	41.7	27.8	38.3	41.7	27.2	29.4	29.3	27.4	32.5	33.6	31.2
	MAE	17.7	20.8	19.9	16.4	21.3	19.9	16.2	18.5	18.2	16.9	19.5	19	18.7
	MBE	-4.63	0.06	-3.46	1.19	0.07	-3.47	0.84	0.02	-1.49	-0.36	0.08	0.27	5.15
	R^2	0.968	0.944	0.935	0.971	0.945	0.935	0.972	0.968	0.968	0.972	0.961	0.958	0.963
	AICc	11408	12278	12538	11218	12256	12539	11150	11363	11354	11167	11703	11815	11615
	a	-	720.2 ± 12.9	575.8 ± 6.8	625.2 ± 235.3	695.5 ± 12.6	574.1 ± 6.4	567.7 ± 280.2	65.8 ± 22.6	32.6 ± 8.6	299.2 ± 683.5	993.9 ± 14.2	1021.1 ± 55.4	-146.8 ± 8942.9
	b	-	45.2 ± 0.4	49.8 ± 0.2	48.4 ± 7.3	45.5 ± 0.4	49.9 ± 0.2	49.9 ± 8.5	66.1 ± 0.7	66.9 ± 0.3	58.7 ± 21.1	20.2 ± 0.9	19.7 ± 3.7	95.9 ± 554.6
	c	-	-	-	-	1.4 ± 0.1	0.1 ± 0.1	1 ± 1.3	48.2 ± 1.6	48.2 ± 0.4	25.2 ± 57.8	-3.5 ± 0.5	0 ± 0.2	-3.4 ± 9.9
	d	-	-	-	-	-	-	-	-1.5 ± 0.1	-1.5 ± 0	-0.8 ± 1.8	0.5 ± 0	0.5 ± 0.1	-0.7 ± 8.6
	e	-	-	-	-	-	-	-	-	-	-	0.2 ± 0	0 ± 0	0.2 ± 0.4

D. Detailed Driver Decomposition

Table 8: Results of driver decomposition for Ω_{Ar} and $[H^+]$. Each value represents the area-weighted average for decomposed drivers and uncertainties for the corresponding zone. The sum of all 12 values (*i.e.*, ΔDriver, ΔSensitivity, and Mass Effect of DIC, TA, SSS, and SST) equals the total trend of Ω_{Ar} and $[H^+]$ per Equations 15 and 14. The total trends in Table 4 may differ slightly from the summed decomposed drivers as a result of averaging across grid cells. Decomposed drivers are in Ω_{Ar} units decade^{-1} for Ω_{Ar} and nmol H^+ kg^{-1} decade^{-1} for $[H^+]$.

		Ω_{Ar}			$[H^+]$		
		ΔDriver	ΔSensitivity	Mass Effect	ΔDriver	ΔSensitivity	Mass Effect
Northern PAR	DIC	-0.030±0.018	-0.002±0.005	0.003±0.005	0.209±0.130	-0.038±0.042	0.033±0.042
	TA	-0.110±0.015	-0.053±0.005	0.053±0.005	0.767±0.102	-0.344±0.038	0.343±0.038
	SSS	0.001±0.000	0.001±0.000	-0.001±0.000	-0.055±0.001	0.025±0.002	-0.024±0.002
	SST	0.000±0.000	0.000±0.000	-0.000±0.000	0.012±0.000	-0.003±0.000	0.003±0.000
Bering Sea Shelf	DIC	0.002±0.020	-0.001±0.002	0.001±0.002	-0.022±0.110	-0.006±0.010	0.006±0.010
	TA	0.025±0.012	-0.003±0.002	0.003±0.002	-0.115±0.060	-0.007±0.008	0.008±0.008
	SSS	-0.001±0.000	0.000±0.000	-0.000±0.000	0.011±0.000	0.001±0.001	-0.001±0.001
	SST	0.001±0.000	-0.000±0.000	0.000±0.000	0.069±0.001	0.000±0.002	-0.001±0.002
Southern PAR	DIC	-0.040±0.010	-0.002±0.001	0.002±0.001	0.213±0.052	-0.019±0.007	0.019±0.007
	TA	-0.005±0.005	-0.002±0.001	0.002±0.001	0.023±0.025	-0.007±0.004	0.007±0.004
	SSS	0.000±0.000	0.000±0.000	-0.000±0.000	-0.003±0.000	0.001±0.000	-0.001±0.000
	SST	0.001±0.000	0.000±0.000	-0.000±0.000	0.054±0.000	-0.005±0.001	0.005±0.001